OSCILLATIONS IN A FORWARD-FACING CAVITY MEASURED USING LASER-DIFFERENTIAL INTERFEROMETRY IN A HYPERSONIC QUIET TUNNEL

This version is slightly revised from the official version reported to Purdue. Items 2, 4, and 20 in the alignment procedure appendix were slightly modified. Per 12 Dec. 2007 email from Rodrigo. This slightly revised version was the one submitted to DTIC.

A Thesis

Submitted to the Faculty

of

Purdue University

by

Rodrigo Segura

In Partial Fulfillment of the

Requirements for the Degree

of

Master of Science in Aeronautics and Astronautics

December 2007

Purdue University

West Lafayette, Indiana

Este trabajo va dedicado a mi papá, mi mamá, mi hermano, y mi Dios.
A ustedes les debo todo lo que soy.

ACKNOWLEDGMENTS

I want to thank my advisor, Professor Steven P. Schneider for building and managing the hypersonic wind tunnels at Purdue University and giving me the opportunity to work on this project. Had it not been for his vote of confidence, the LDI would sit in a drawer for years to come. Furthermore, his expertise and frankness helped me get through the difficulties encountered in this experimental research. I would also like to thank my committee members, Professors Steven H. Collicott and Anastasios S. Lyrintzis, their guidance and suggestions are appreciated.

The machinists and technicians at the Purdue Aerospace Sciences Laboratory were extremely helpful during the course of the project. I thank them for their excellent craftsmanship and valuable technical assistance. I would like to express my special gratitude to Madeline Chadwell, Robin Snodgrass, and John Phillips all of whom went out of their way to assist me with unexpected experimental breakdowns on multiple occasions. Jerry Hahn and Jim Younts were also included in that crew.

The office and information systems staff at the Aeronautical and Astronautical Engineering department at Purdue University also played an important role. Linda Flack's timely reminders made the logistics of my academic life easy. I would like to give special thanks to Joan Jackson; she made me laugh and was patient and helpful even when I demanded her help on rather short notice. Joe Kline's technical assistance is appreciated.

A great deal of contribution came from my fellow researchers. Tom Juliano, Katya Casper, Mikey Hannon, Jackie Jaron, Erick Swanson, Bob Manning, Matt Borg, and Brad Wheaton, provided invaluable help and support without which completing the project would have been orders of magnitude more difficult.

None of this would have been possible without the precious friendship of those who kept me company. My most special thanks to Luis Guillermo Arboleda, Oscar

Alfredo Ardila, Jaime Andres Rueda, Camila Pachón, Muriel Gallego, Fabian Consuegra, Elena Merino, Vanesa Toquero, Maria Muñoz, and Carolina Gonzales. Your friendship and constant physical and spiritual company were crucial in my survival these years. I would like to thank Maria Paula Forero for existing and willingly caring for me like she does. I owe her my happiness during my last months here.

And most importantly, I want to say thank you to my dad, my mom, my brother, and my God. Thank you for standing by me at all times. You are the meaning of this life. I love you.

TABLE OF CONTENTS

LIST OF TABLES

LIST OF FIGURES

SYMBOLS

A	cross-sectional area
a	speed of sound
D	forward-facing cavity diameter
d	distance between lens systems
E	photoreceiver output voltage
$E1$	first photodiode induced voltage
$E2$	second photodiode induced voltage
f	‘Organ-Pipe’ frequency in Hz
I	laser-beam irradiance
L	forward-facing cavity depth
p	pressure
T	temperature
t	time
M	Mach number
V	driver tube volume
R	specific gas constant for air
U	flow velocity
S	Sutherland constant for air
Re	Reynolds number
Kn	Knudsen number
γ	ratio of specific heats
δ	bow-shock standoff distance
η	recovery factor
λ	laser wavelength
μ	viscosity

$\delta\Phi$	optical path length difference in nm
$\delta\phi$	phase shift in radians
ρ	density
ω	‘Organ-Pipe’ frequency in radians

Superscripts

$*$	sonic point
$\sim$	root-mean-square
$-$	mean
$\star$	adjusted value

Subscripts

0	total (stagnation) value
1	pre-shock value
2	post-shock value
$crit$	critical value
i	initial value
max	maximum value
r	recovery
ref	Sutherland reference
R	reference beam
S	signal beam
α	first lens system
β	second lens system

Acronyms

ASL	Aerospace Sciences Laboratory
BAM6QT	Boeing/AFOSR Mach-6 Quiet Tunnel
BFL	Back Focal Length

CCA	Constant Current Anemometer
EFL	Effective Focal Length
FFC	Forward Facing Cavity
LDI	Laser Differential Interferometer
OPD	Optical Path length Difference
PQFLT	Purdue Quiet Flow Ludwieg Tube
RMS	Root Mean Square

ABSTRACT

Segura, Rodrigo. M.S.A.A., Purdue University, December, 2007. Oscillations in a Forward-Facing Cavity Measured Using Laser-Differential Interferometry in a Hypersonic Quiet Tunnel. Major Professor: Steven P. Schneider.

Laminar-turbulent transition is a pivotal factor for the design of hypersonic vehicles but the mechanisms that induce transition are not well understood. A laser differential interferometer (LDI) is a non-intrusive optical device that measures the optical path length difference between two laser beams. The LDI is a reliable calibrated instrument to assist the study of boundary layer instability-wave growth in hypersonic flow and has high sensitivity and frequency response. A LDI with a commercial balanced photodetector capable of detecting optical path length differences of $\lambda/21,000$ from DC to 80 MHz was assembled and tested in the Purdue Quiet-Flow Ludwieg tube (PQFLT). Fluctuations in the subsonic region of a forward-facing cavity were measured with the LDI and compared to those detected with a Kulite pressure transducer at the base of the cavity. Predictions of self-resonating deep cavities were confirmed. The LDI was then adapted and transferred to the Boeing/AFOSR Mach-6 Quiet Tunnel (BAM6QT).

1. Introduction

1.1 Purpose

Laminar-turbulent boundary layer transition is a pivotal factor for the design of vehicles traveling at hypersonic speeds but the mechanisms that induce transition are not so well understood [1–5]. The primary purpose of this research is to develop a reliable calibrated instrument to assist the study of boundary layer instability-wave growth at the Purdue Mach-6 wind tunnel. A laser differential interferometer (LDI) was assembled and tested in the Purdue Quiet Flow Ludwieg Tube (PQFLT) before being adapted and transferred to the Boeing AFOSR Mach-6 Quiet Tunnel (BAM6QT) facility. Since the LDI is highly sensitive to mechanical vibrations and electrical noise, and the optical table near the PQFLT was no longer floated, a large amplitude known disturbance was required to test the instrument. A forward-facing cavity was chosen to compare oscillations detected by the LDI behind the bow shock to those detected by a Kulite pressure transducer mounted at the base of the cavity. Pressure transducers and cold-wires were also used to characterize the freestream flow and validate the preliminary LDI test results.

1.2 Motivation and Background

Optical interferometry has been used in a myriad of forms to perform flow diagnostics. The motivation for the use of this technique arises from the simple relation between gas density ρ and the optical path length of a light beam passing through a gas flow. The laser differential interferometer is a nonintrusive optical flow diagnostic device particularly applicable to low-density flow [6–13]. It measures the optical path length difference between two laser beams known as reference and signal beams.

When the beams pass through a flow whose density fluctuates in time, causing its index of refraction to change, the optical path length of the beams varies and the difference in their individual variations is recorded by the LDI. Among the advantages of the LDI over other nonintrusive techniques are its high sensitivity, good spatial resolution, and large bandwidth [14–18]. All of these make it a fine instrument to analyze the flow in the PQFLT. Smeets and George developed the first version of the LDI in 1973, with which they were able to resolve optical path length differences as small as $\lambda/30,000$ over bandwidths between 100 Hz and 10 MHz [7]. Salyer developed a feedback stabilized version of the LDI at Purdue University able to resolve minimum path length differences of $\lambda/13,000$ at a bandwidth of 6 MHz [17,18]. Azzazy and O'Hare also developed optical and nonintrusive methods to make similar measurements [19,20].

In Salyer's experiment, a laser perturbation was generated upstream of a blunt body at Mach 4 and the LDI was used to analyze its propagation across the bow shock. Salyer characterized the perturbation profile across the shock and compared it with the LDI results. The laser system used to generate the laser perturbation in the work done by Salyer [15–18], Schmisseur [21], and Ladoon [22,23] could not be readily resurrected for this project, so it could not be used to test the performance of the LDI.

A forward-facing cavity can be regarded as a resonance tube. Engblom et al. numerically simulated the unsteady flow inside the cavity and obtained agreement with the experimental data for the pressure oscillations at the base of the cavity [24]. Using their experimental and computational results, Hoffman et al. state that the frequency of the oscillations is inversely proportional to the cavity depth and the amplitude is directly proportional to it [25]. Ladoon et al. measured pressure fluctuations inside a forward-facing cavity and pointed out primary mode frequencies and harmonics for several cavity depth ratios, L/D (length to diameter), ranging from 0.0 to 1.984. They state that '*the cavity was found to be very sensitive to freestream noise. Even very weak freestream disturbances that are normally too small to be* *detected are amplified to measurable levels by the cavity*' [23]. Kim and Park also reported that perturbations in the freestream excited the oscillations inside the cavity at the acoustic resonant frequency for various L/D values [26]. Lastly, Engblom et al. confirm that fluctuations inside the cavity resonate at the primary mode ('Organ-Pipe') frequency which is inversely proportional to cavity depth. They also mention that the amplification of the fluctuations by the cavity is thought to be directly proportional to the cavity depth [27, 28]. Such large amplitude oscillations should be measurable by the LDI under noisy conditions in the PQFLT. This provides a suitable method for obtaining quantitative data comparable to the LDI results to validate its performance. Moreover, Engblom et al. also reported that numerical results indicate that deeper cavities are unstable and resonate strongly without freestream noise, generating self-sustained resonant oscillations [27]. However, Ladoon et al. state that these deep-cavity simulations have not been experimentally confirmed in a quiet-flow facility [23]. The reader can find further numerical results on forward-facing cavity flow in Refs. [24] and [29].

Second-mode instability waves have been studied in the past and measurements were made under quiet and noisy conditions in the BAM6QT [30, 31]. The ultimate motivation for developing this instrument is to complement measurements made on the surface of cone models by S. J. Rufer using hot wires, and by M. Estorf using flush mounted pressure transducers [30–32].

1.3 Approach

Salyer's LDI system was reassembled and improved by upgrading to a commercial balanced photodetector able to detect a minimum path length difference of $\lambda/21,000$ at frequencies ranging from DC to 80 MHz (3 dB signal drop). Furthermore, the system was adapted to the BAM6QT with a vibration control system.

2. Flow Facility

The two wind tunnels used in this research were built to better understand laminar-turbulent transition in high-speed boundary layers. This is a complex phenomenon that affects a myriad of conditions critical to the design of vehicles that fly at hypersonic speeds [1,2]. During the last five decades, despite extensive research to predict in-flight transition, there have been few reliable conclusions. This is partly because flight conditions lack the high level of acoustic disturbances radiated from the turbulent boundary layers that exist on the tunnel walls in conventional wind tunnels and have a strong effect on transition [33, 34]. The pitot pressure fluctuation level normalized by its average $\tilde{p}/\bar{p}$, here known as the freestream noise, is approximately $1-2\%$ in conventional (noisy) wind tunnels. On the other hand, a freestream noise level of 0.02% was recorded in flight at Mach 2 [33]. This two-orders-of-magnitude difference became a strong motivation for the development of quiet facilities for transition research [35]. The wind tunnels used in this research are among the few facilities capable of generating quiet flow at supersonic and hypersonic speeds. By 'quiet' it is understood that the freestream noise levels in the tunnel are less than 0.1% [33].

The quiet-flow core in the test section is demarcated upstream by the uniform flow characteristics, and downstream by the Mach lines generated at the onset of turbulence in the nozzle wall boundary layer. Figure 2.1 shows a sketch of the nozzle geometry and the radiated noise.

2.1 Pressure & Temperature Sensors

Kulite Semiconductor pressure transducers were used to measure the stagnation pressure drops in the contraction section of both tunnels, and behind the normal

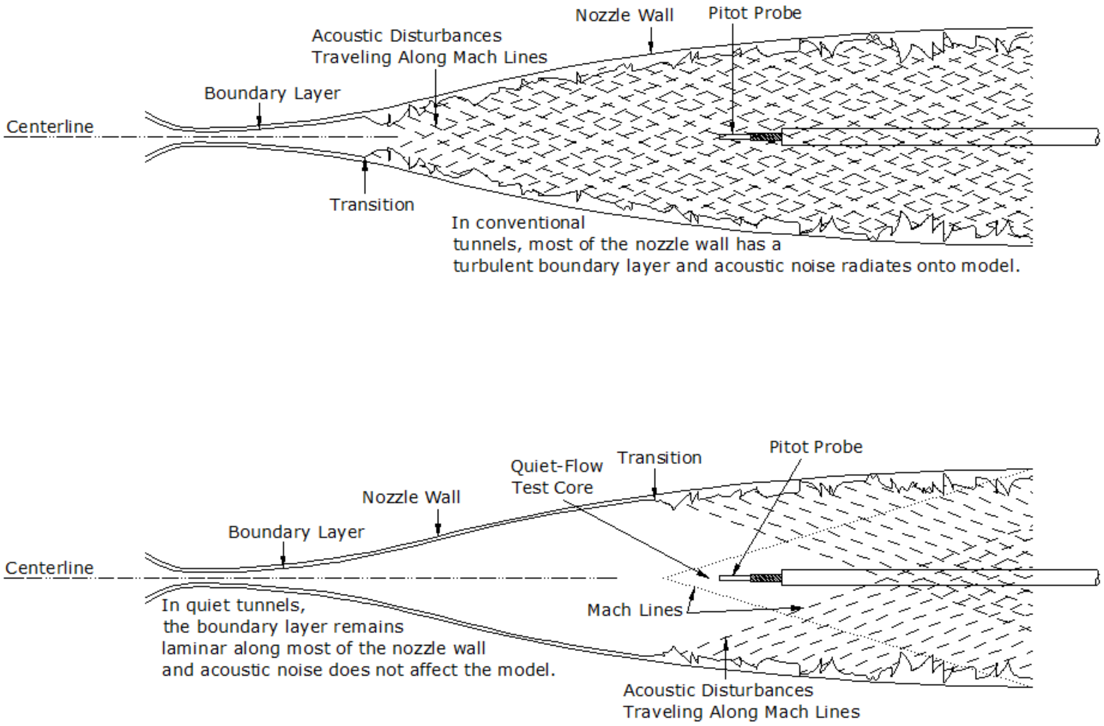

Figure 2.1: Diagram of noise radiated from boundary layer transition on the nozzle wall

shock of several pitot probes and a hemispherical nose. They were also used at the base of two forward-facing cavity models described in Section 3.1.1. A 1/16-in. hole in the wall of the driver tube near the entrance of the PQFLT contraction section leads to a 0.5-in.-dia. pipe, about 3 in. long. After the pipe, a 0.5-in.-dia. tee fitting was installed with a Wika analog gauge-pressure gauge on one side, and a Kulite pressure transducer, with a range from 0 to 50 psia, on the other (model XTL-123B-190-50A). Similarly, a flush-mounted Kulite transducer (model XTEL-190-200) is located on the wall of the driver tube, near the entrance to the contraction of the BAM6QT, with a range from 0 to 200 psia. All the pitot probes, the hemispherical nose, and the forward-facing cavity are equipped with Kulite transducers (model XCQ-062-15A) with a range from 0 to 15 psia. Note that the Kulites installed in the pitot probes or test models used in the BAM6QT have a mechanical stop placed behind the strain-gauge diaphragm, to prevent damage that would otherwise be sustained at pre-run pressures exceeding twice the operating pressure of the instrument. Since the maximum driver pressure used in the PQFLT is 26 psia there is no need for the stopped Kulites in the Mach-4 facility.

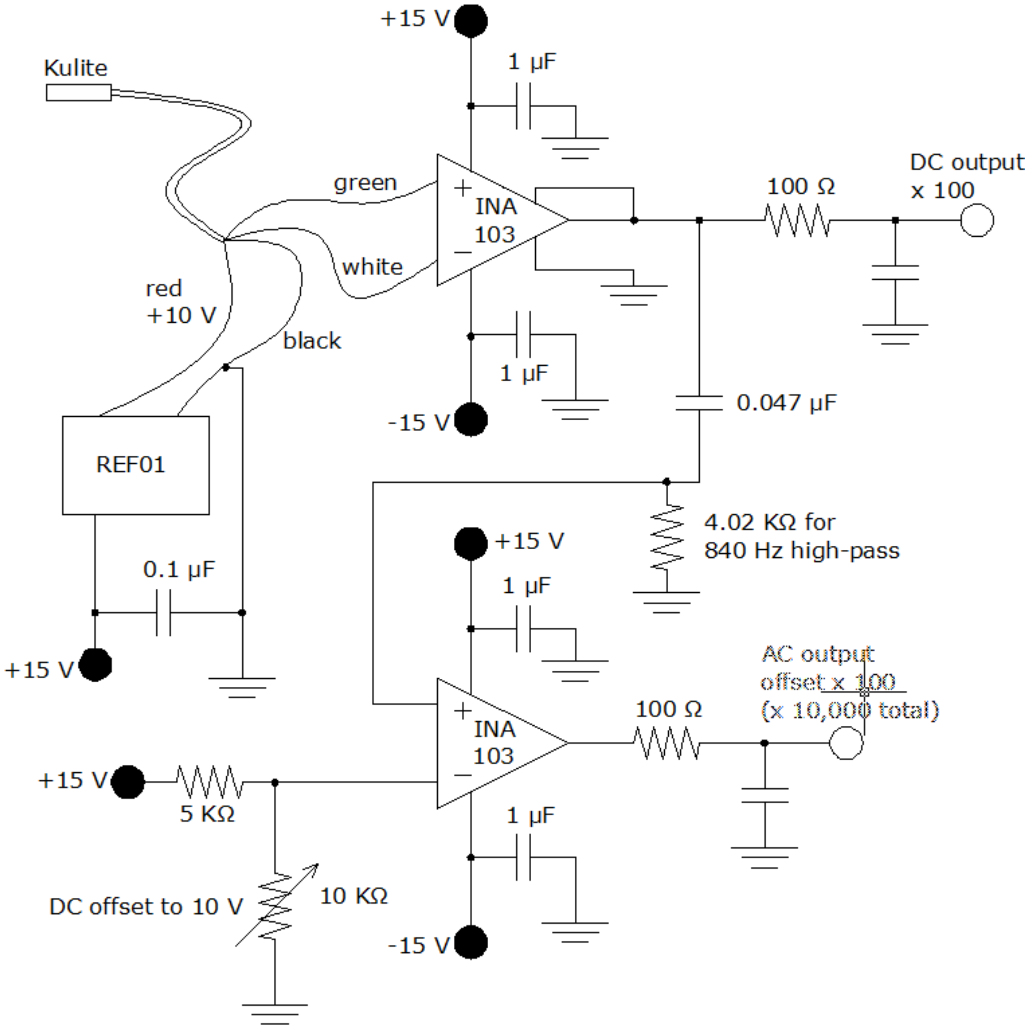

Figure 2.2: Kulite amplifier circuit

To obtain a signal from the Kulite pressure transducers, custom electronics were designed by Schneider and have been used by the Ludwieg Tube research group at Purdue University for a number of years [36]. A schematic of the Kulite amplifier circuit is shown in Figure 2.2. A REF01 +10 V precision-voltage-reference integrated circuit supplies power to the Kulite. The transducer output is amplified by a factor of 100 using a low noise INA103 instrumentation amplifier. The output is then high-pass filtered at 840 Hz and fed to a second INA103 which supplies a further gain of 100 to the AC part of the signal. The DC signal is used to calculate the mean stagnation pressure for both the contraction and the test section. The AC signal obtained from the Kulite in the pitot probe is used to calculate the freestream noise levels in the nozzle.

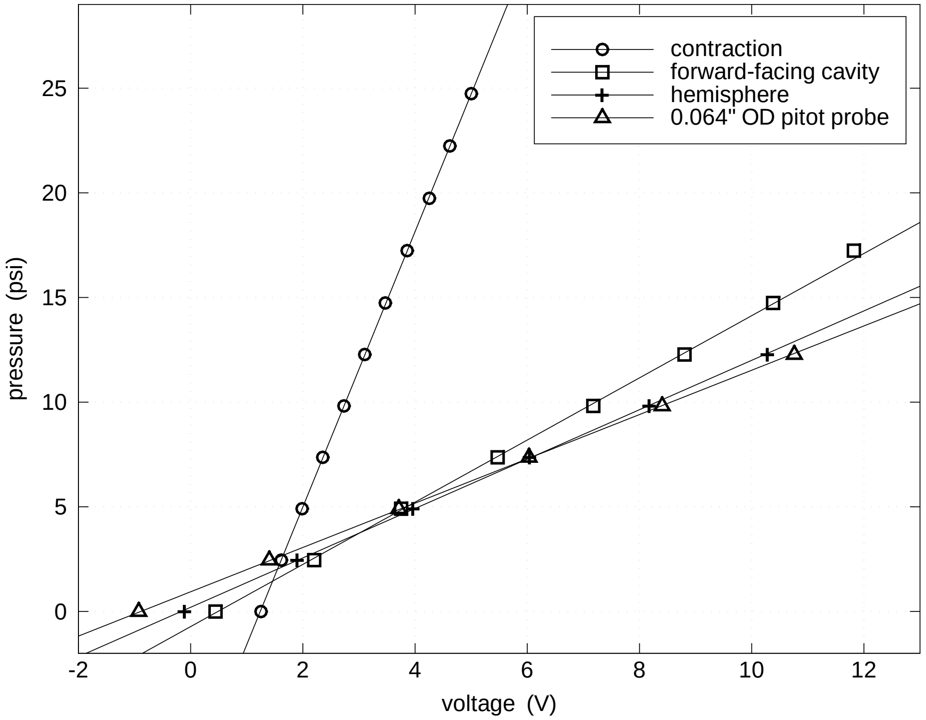

Figure 2.3: Kulite transducer calibration curves

To calibrate the transducers in the PQFLT, the air in the Ludwieg tube was evacuated down to a gauge pressure of about −14 psi and slowly pumped up to about 12 psia. The output from the transducer amplifier was monitored along with the reading from a Wika analog gauge-pressure gauge (model 212.25HR, accuracy:

Table 2.1: Kulite transducer calibration values

Transducer	$\frac{psia}{Volt}$	Offset (psia)
Contraction	6.5777	−8.1631
Pitot	1.0585	0.9393
Hemisphere	1.1801	0.1976
Forward-facing cavity	1.4856	−0.724

±0.5% of span, range: 30” Hg-0-15 psi) from which the ambient pressure was subtracted to obtain the absolute pressure. Calibration curves for all the transducers are shown in Figure 2.3, with their respective fit values in Table 2.1. Note that the subtraction of ambient pressure from the gauge pressure reading, during the calibration, is a large source of error that strongly affects the Mach number calculation.

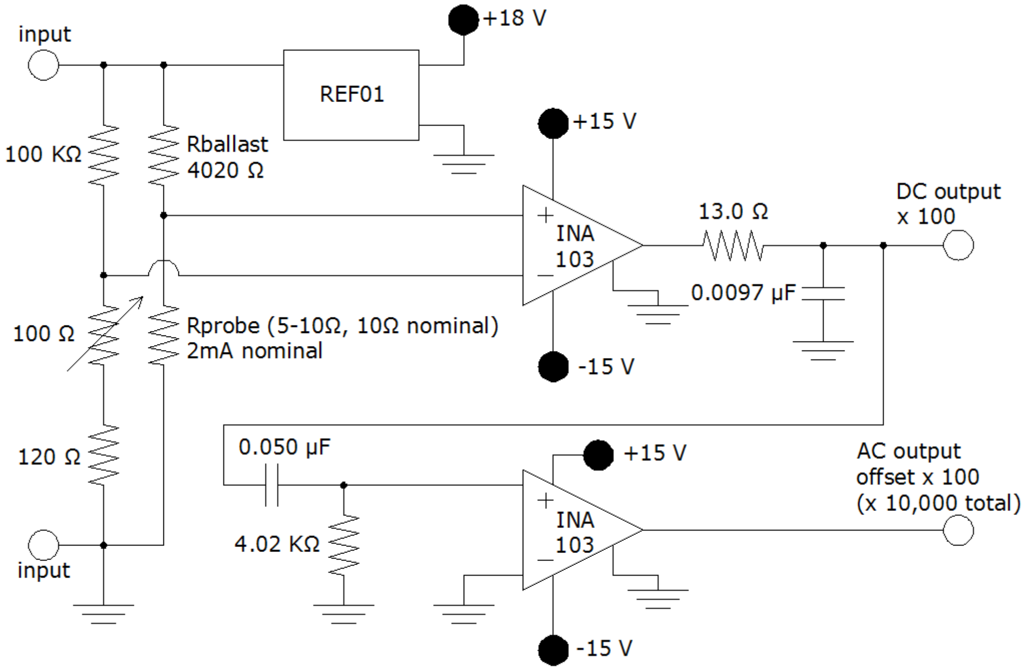

Figure 2.4: Constant current anemometer circuit

The recovery temperature in the test section was measured by running a 2.5 mA current through a $1.5 \cdot 10^{-4}$ in.-dia. tungsten wire to sense the resistance variations in the wire. A custom-made constant current anemometer (CCA) designed by Schneider was used to condition the signal from the wire [37]. A schematic of the CCA circuit is shown in Figure 2.4. A REF01 precision voltage reference integrated circuit supplies 10 V to a 4020 Ω ballast resistor in series with the wire. The DC output from the cold wire is amplified by a factor of 100 using a INA103 instrumentation amplifier before being digitized by the scope.

Table 2.2: Kulite transducer calibration values

Instrument	Fit value	Offset
Cold-wire	90.162 K/Ω	−1113.5 K
CCA	4.0516 Ω/V	10.213 Ω

To calibrate the cold wire, the temperature inside a Lindberg/Blue M mechanical oven (model MO1440P3A-1) was raised to about 350 K and slowly decreased to about 300 K. The resistance across the wire was monitored along with the temperature inside the oven measured with a K-type thermocouple (model: Omega KTSS-18G-18) and a Fluke 51 II reader. Then, a potentiometer was used to input multiple resistance values into the CCA (obtained during the oven calibration) while recording its output. The calibration curves for the wire and the CCA are shown in Figure 2.5, with their respective fit values in Table 2.2. All calibrations were made before performing the experiment.

2.2 Tektronix TDS 5034B Digital Phosphor Oscilloscope

All the experimental data was recorded using an 8-bit Tektronix TDS 5034B Digital Phosphor Oscilloscope in Hi-Res mode. Hi-Res mode means that the scope samples data at 1 GHz, averages it on the fly, and saves it at a frequency specified by

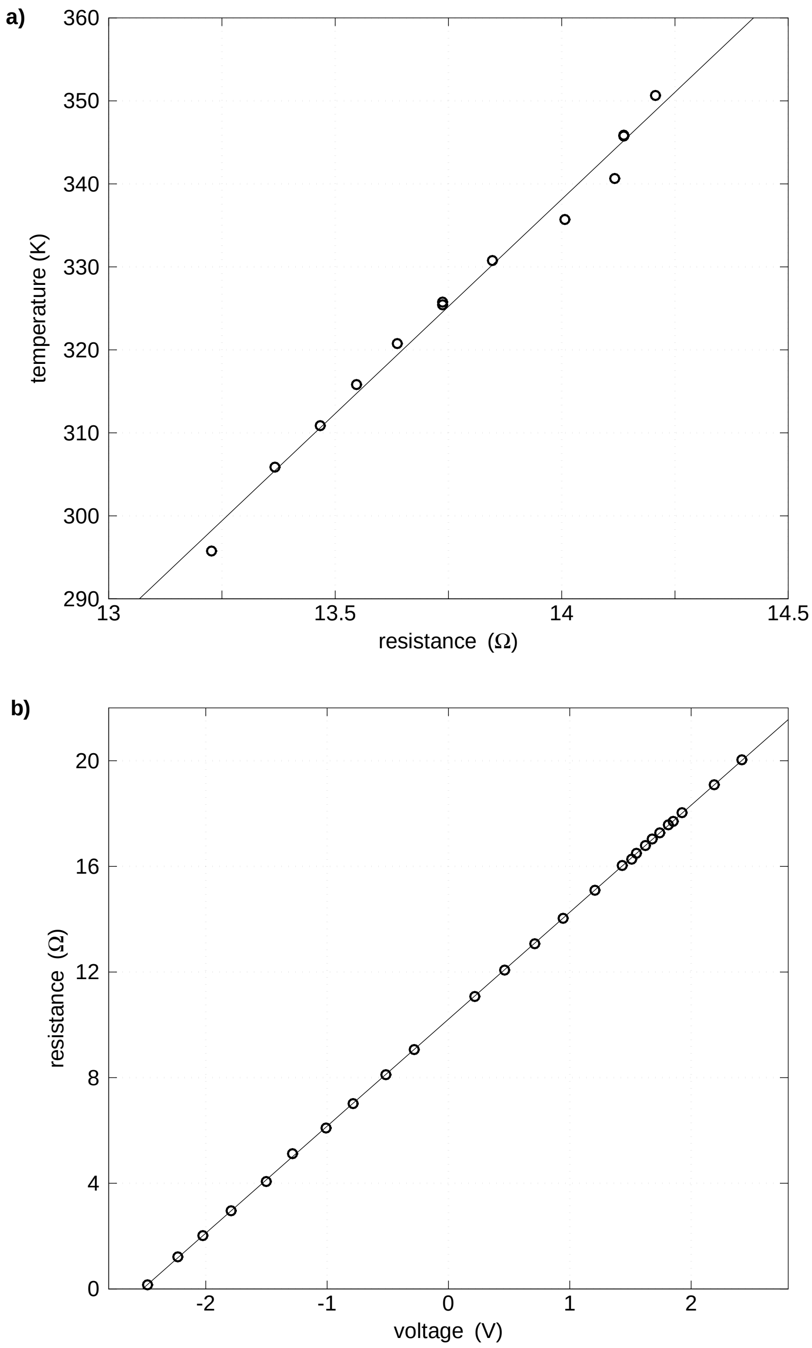

Figure 2.5: a) cold-wire calibration curve; b) CCA calibration curve

the user. When set to Hi-Res mode, the oscilloscope supplies 11-12 bits of resolution and digital filtering.

2.3 Purdue Quiet Flow Ludwieg Tube

The PQFLT is a 30.5-cm diameter, 20.7-m long pipe with a converging-diverging nozzle on one end followed by a test section and a diffuser that leads to a 500 ft^3 vacuum tank. A schematic of the PQFLT is shown in Figure 2.6. A smooth contraction tapers the driver tube into the 8.826 cm^2 nozzle throat leading to the 9.7×10.9 cm rectangular test section, through a nozzle designed to achieve Mach-4 flow in the test section.

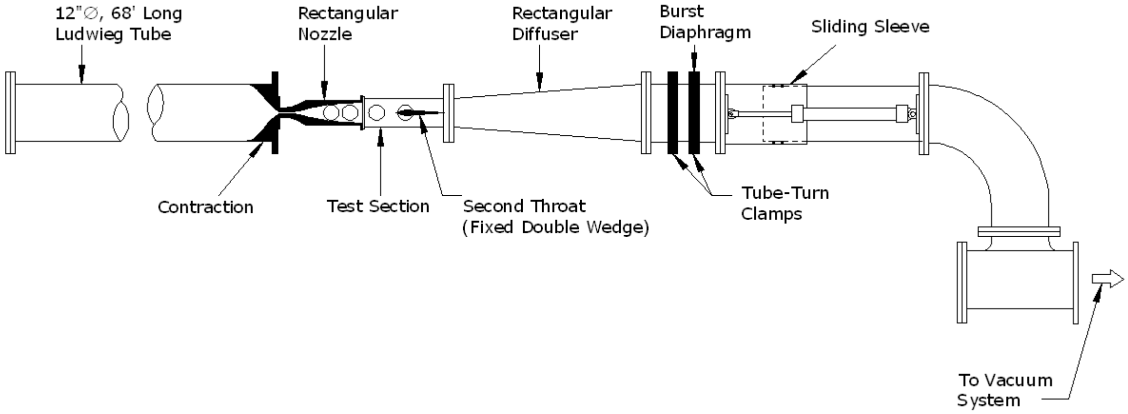

Figure 2.6: Purdue Mach 4 quiet-flow Ludwieg tube

To generate the quasi-steady Mach-4 flow in the tunnel, a mylar diaphragm is placed between the diffuser and the sliding sleeve. The vacuum tank is evacuated and the pressure in the driver tube is raised to the desired initial stagnation pressure. A Nickel-Chromium $30AWG$ wire is attached to the surface of the diaphragm with masking tape and a pulse of electrical current runs through the wire to heat it up; the diaphragm cleanly ruptures generating an expansion wave that moves upstream resulting in Mach 4 quiet flow in the test section. Note that quiet flow is achieved and maintained in this tunnel in large part due to the 2 microinch polish on the nozzle walls and the fact that the air inside the driver tube is filtered. Hence, the boundary layer on the nozzle walls remains laminar to a greater extent and particles that can act as a transition bypass mechanism are removed from the flow.

2.3.1 Flow Conditions

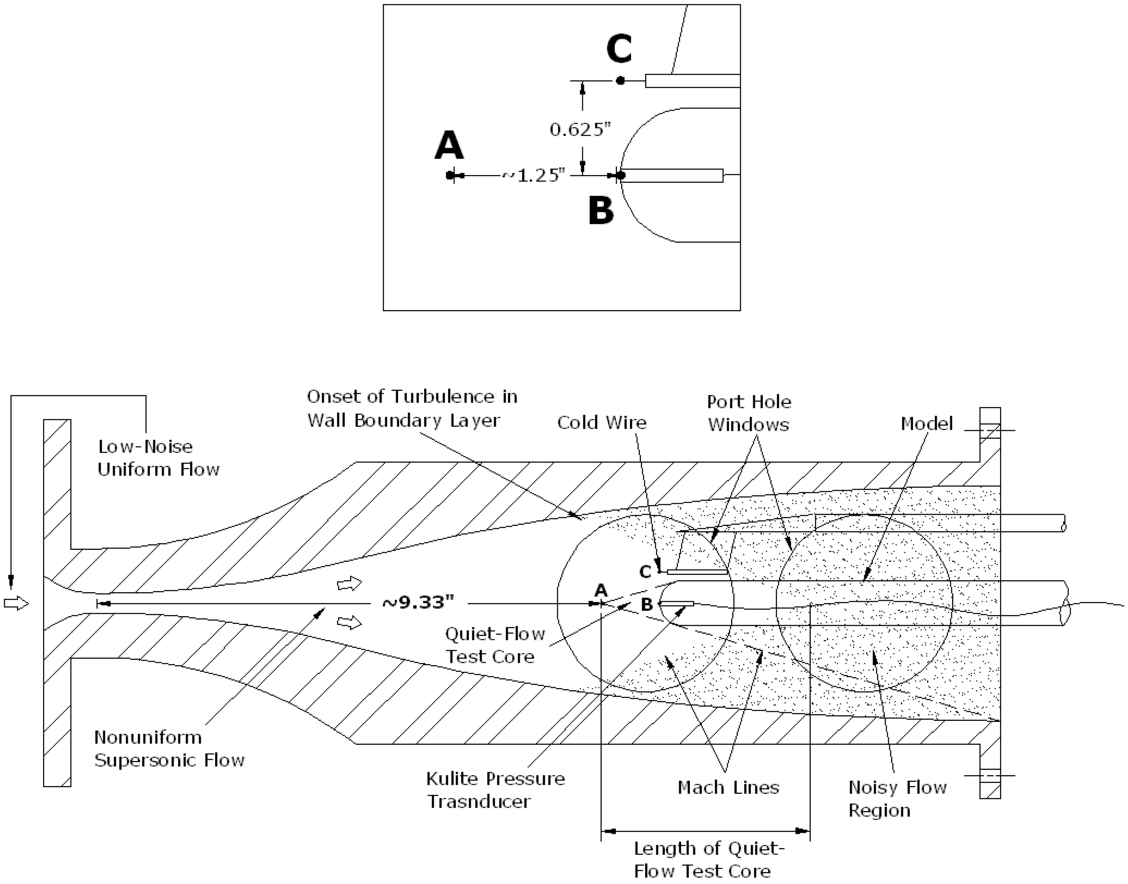

Figure 2.7: Hemispherical nose model and cold wire in the PQFLT test section

When flow is initiated in the tunnel an expansion wave begins to reflect cyclicly between the contraction and the upstream end of the driver tube, decreasing the stagnation pressure that drives the supersonic nozzle flow. The uniform flow region begins approximately 9.33 in. downstream of the throat along the centerline as shown in Figure 2.7. Calibrated pressure and temperature sensors described in detail in Section 2.1 are placed at various locations in the tunnel to calculate the flow conditions during a run. The Mach number in the contraction is less than 0.01, hence the signal from the Kulite located near its entrance provides the total pressure during the course of a run with an inlet line delay of a few milliseconds relative to the Kulite mounted in the test section. Other Kulite pressure transducers were mounted in a pitot probe, a hemispherical nose, and a forward-facing cavity. The latter three, when in use, were located approximately 1.25 in. downstream from the beginning of the quiet-flow test core (at point B as shown in Figure 2.7) and measured the drop in stagnation pressure behind the normal shock throughout the tunnel run. A cold wire located at the same axial location as the test models, 0.625 in. above the centerline (see Figure 2.7), measures the initial stagnation temperature, and the drop in recovery temperature throughout the run. The rest of the flow variables are computed from these quantities. Note that the pitot probe and the cold wire are both mounted on the same traverse mechanism, hence they cannot be used simultaneously. For this reason, the pitot probe is primarily used to measure freestream noise and the Kulite mounted on the tip of the hemispherical nose is used in conjunction with the cold-wire to calculate the rest of the mean flow variables.

The oscilloscope was set to record ten seconds of data at a 100 KHz sampling rate in Hi-Res mode. Figure 2.8 shows a typical set of calibrated pressure data from runs at three different initial driver pressures with the pitot probe in the test section. A simple choked-throat theoretical approximation to the drop in total pressure during a run developed by Schneider et al. [37] is also displayed in Figure 2.8. The total pressure drop is computed assuming an isentropic expansion in the nozzle as,

$$\frac{p_0}{p_{0,i}} = \left(1 + \frac{\gamma - 1}{2}\frac{A^*}{V}\sqrt{RT_{0,i}}tc_1\right)^{\frac{2\gamma}{1-\gamma}}, \tag{2.1}$$

where

$$c_1 = \sqrt{\gamma\left(\frac{2}{\gamma + 1}\right)^{\frac{\gamma+1}{\gamma-1}}}, \tag{2.2}$$

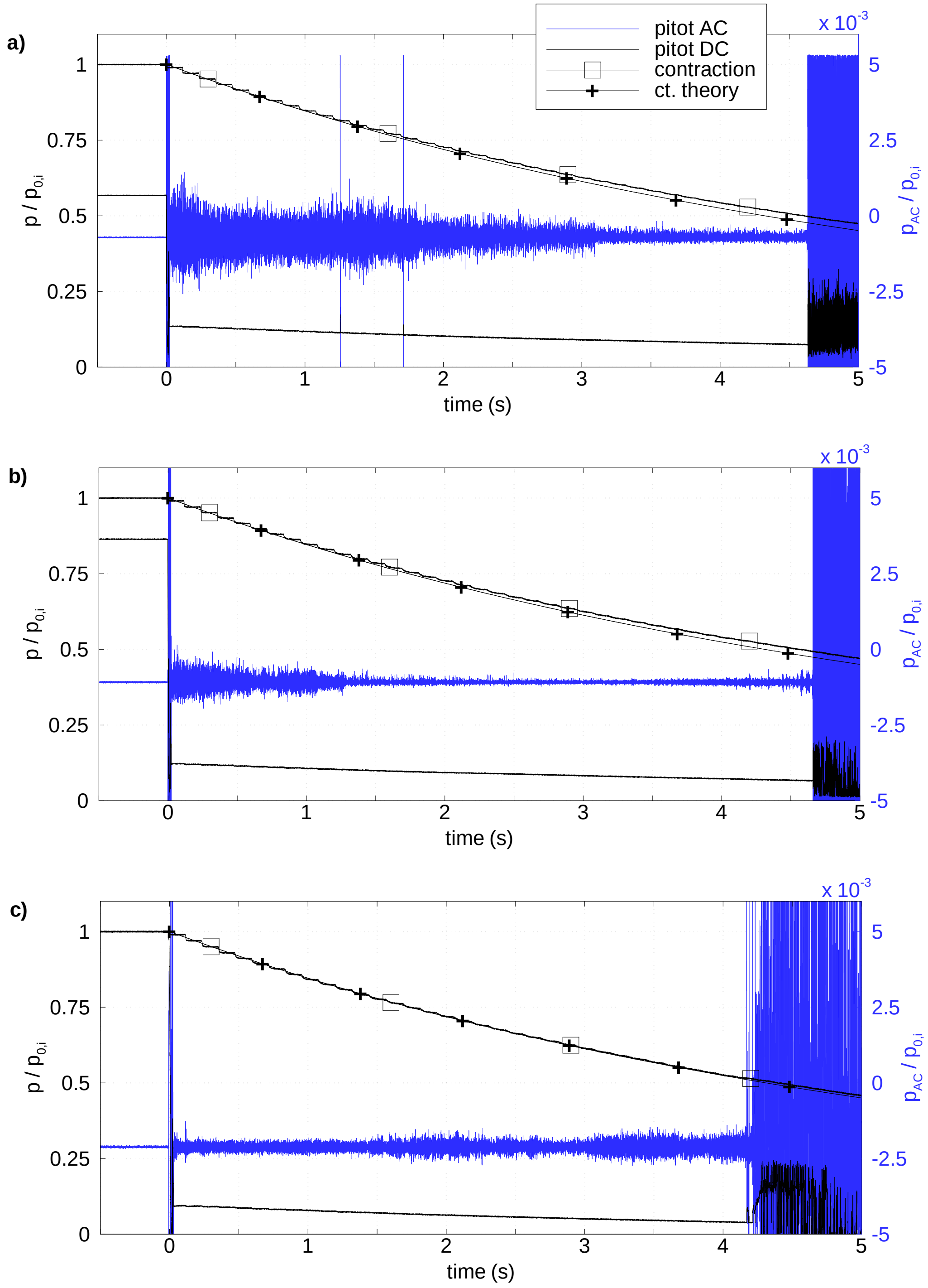

Figure 2.8: Typical pitot and contraction pressure traces: a) $p_{0,i} = 24$ psi, b) $p_{0,i} = 16$ psi, c) $p_{0,i} = 8$ psi

and V is the driver tube volume, A^* is the throat area, $p_{0,i}$ is the initial driver pressure, $T_{0,i}$ is the initial driver temperature, and t is the time since flow initiation.

The freestream tunnel noise is computed by normalizing the root-mean-square (rms) of the high-frequency (AC) component of the pitot signal $\tilde{p}$, by the average of its full bandwidth (DC) signal $\bar{p}$. The pitot data was collected at a rate of $1 \cdot 10^5$ samples per second and divided into 0.1 s intervals for the calculation of $\tilde{p}$ and $\bar{p}$. Thus, $1 \cdot 10^4$ pressure values were used to calculate each data point. Note that the data was not filtered in any way to eliminate aliasing, which is not expected.

The levels of freestream noise during 9 individual runs were measured with the 0.067 in.-dia. pitot and are plotted in Figure 2.9. The legend refers to the initial driver pressure for each run and the data displayed were only computed between 0.2 s and 4.2 s after supersonic flow is established in the test section. This window was chosen because the shortest run made was slightly longer than 4.2 s.

The author believes that the steep rise in freestream noise at initial total pressures under 8 psi is due to a small step in the nozzle throat. This tunnel is currently used for teaching as well as for research. Some years ago, a group of students separated the nozzle and contraction sections, introducing a small step (about 0.002 in.) very close to the throat of the nozzle (see Figure 2.11). Schneider and Haven also measured the freestream noise in this tunnel and obtained consistently low values for initial driver pressures around $10-14$ psi [36,37]. Munro made further measurements of the freestream noise at initial driver pressures as low as 7 psi [38, 39]. According to his measurements, freestream noise decreases consistently as driver pressure decreases. Thus, the high fluctuations at low pressure seemed to be an anomaly caused by the small step in the throat. For this reason, the run made with $p_{0,i} = 24$ psi was used to calculate the mean flow variables in the test section (before the nozzle was repolished).

Freestream noise during 11 individual runs was measured with the hemispherical nose as plotted in Figure 2.10. Again, the legend refers to the initial driver pressure for each run and the data were only computed between 0.2 s and 4.2 s after supersonic

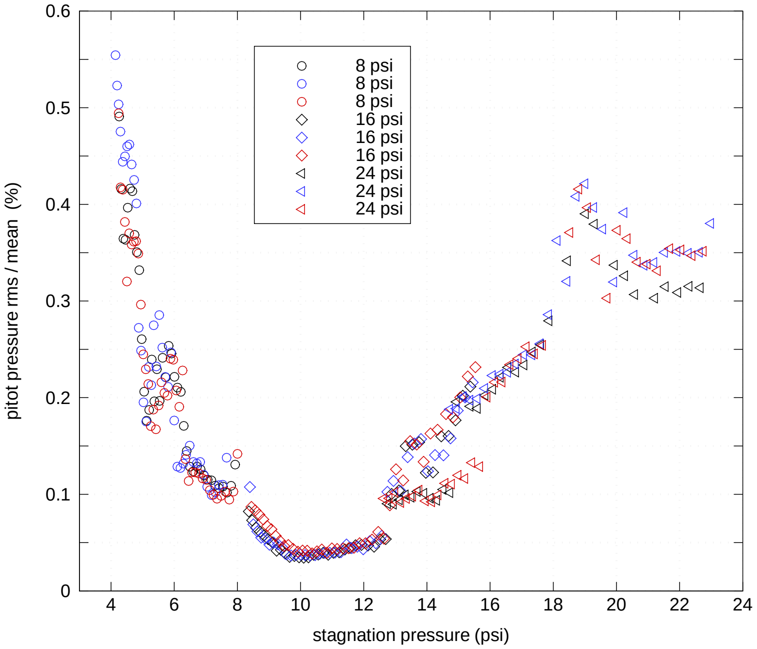

Figure 2.9: Freestream noise level in the PQFLT measured with 0.067 in.-dia. pitot probe before repolishing nozzle

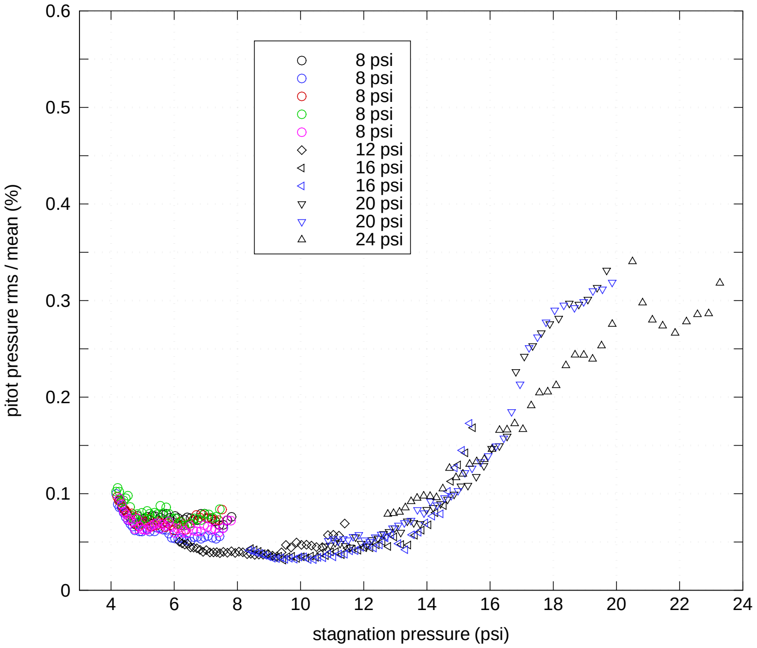

Figure 2.10: Freestream noise level in the PQFLT measured with 1 in.-dia. hemispherical nose before repolishing nozzle

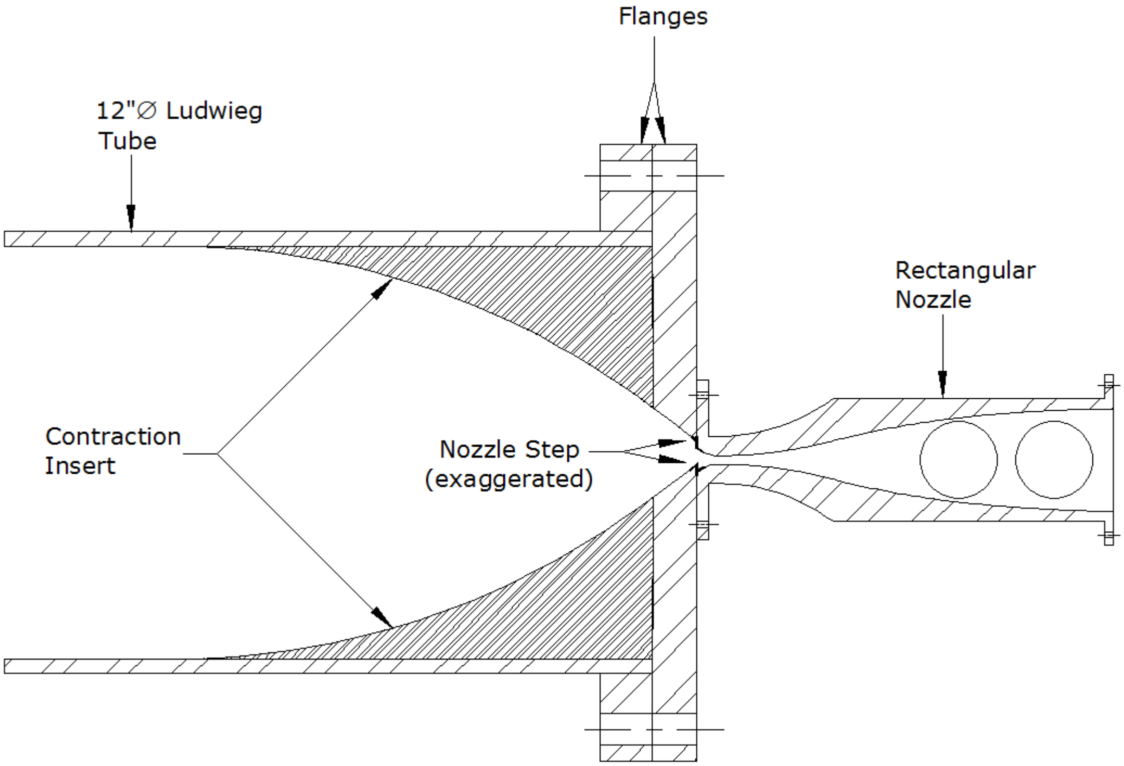

Figure 2.11: Exaggerated sketch of step in the PQFLT nozzle

flow begins. Figure 2.12 shows a typical set of calibrated pressure and recovery temperature data from a run with the hemispherical nose and the cold-wire inside the test section. It is clear from Figures 2.9 & 2.10 that the size of the probe in the test section has an effect on the data collected. It seems likely that the freestream noise levels measured by the Kulite in the tip of the hemispherical nose are lower than those measured with the 0.067 in.-dia. pitot probe because the pressure fluctuations in the subsonic region behind the normal shock are averaged over a larger area.

Note that the temperature data displays an increase in noise before the flow becomes subsonic in the test section. It is possible that the cause for this noise is related to the fact that the cold wire is not located at the centerline as is the Kulite. However, Schneider and Haven, as well as Munro, also made calibrated temperature measurements using cold wires and obtained noisy fluctuations that appeared before the Kulite indicated the end of the run [37,39]. The source of this noise is unknown.

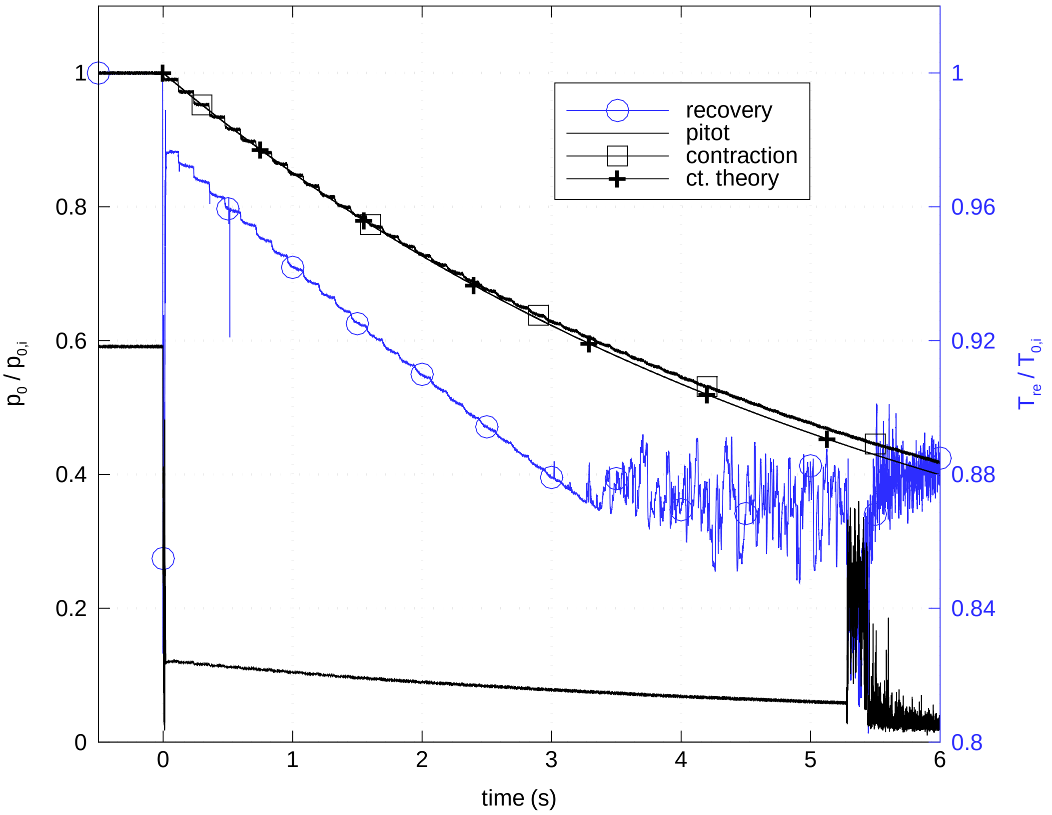

Figure 2.12: Typical stagnation pressures before and after normal shock, along with recovery temperature

To calculate the rest of the flow variables, data from the Kulite mounted on the tip of the hemispherical nose and the cold-wire was used. The recovery temperature T_r is the temperature that a cold-wire assumes when placed in a compressible flow. At low speeds, the recovery temperature is equal to the stagnation temperature of the flow, T_0. But when the cold-wire is exposed to a high-speed compressible flow, it does not exactly achieve the stagnation temperature and equilibrates at a recovery temperature given by [40, 41],

$$T_r = \eta T_0, \tag{2.3}$$

where η is known as the recovery factor.

The Mach number M was calculated using the Rayleigh Pitot formula,

$$\frac{p_{01}}{p_{02}} = \left(\frac{(\gamma+1)^2 M^2}{4\gamma M^2 - 2(\gamma-1)}\right)^{\frac{\gamma}{\gamma-1}} \cdot \left(\frac{1-\gamma+2\gamma M^2}{\gamma+1}\right), \tag{2.4}$$

where $\gamma = 1.4$ is the ratio of specific heats and p_{01} and p_{02} are the stagnation pressures before and after the normal shock. These are measured by the contraction Kulite and the Kulite mounted on the tip of the hemispherical nose model, respectively. A bisector method was used to solve for M. Note that the error in the calibration of the pitot Kulite strongly affected the mean Mach number at low initial driver pressures; hence, it is not reported.

To compute Kn for the cold wire, the total temperature during tunnel runs was approximated assuming an isentropic expansion in the nozzle as

$$T_0 = T_{0,i}\left(\frac{p_0}{p_{0,i}}\right)^{\frac{\gamma-1}{\gamma}}, \tag{2.5}$$

and the total density was computed from the ideal gas law as,

$$\rho_0 = \frac{p_0}{RT_0}, \tag{2.6}$$

where $T_{0,i}$ is the initial (pre-run) temperature recorded by the cold-wire, p_0 is the total pressure measured by the contraction Kulite, and $R = 287$ J/Kg·K is the specific gas constant for air at standard temperature and pressure. The static flow properties were also calculated assuming an isentropic expansion in the nozzle as,

$$p = p_0\left(1+\frac{\gamma-1}{2}M^2\right)^{\frac{-\gamma}{\gamma-1}}, \tag{2.7}$$

$$T = T_0\left(1 + \frac{\gamma - 1}{2}M^2\right)^{-1}, \tag{2.8}$$

$$\rho = \rho_0\left(1 + \frac{\gamma - 1}{2}M^2\right)^{\frac{-1}{\gamma-1}}, \tag{2.9}$$

and the speed of sound a and flow velocity in the test section U are given by,

$$a = \sqrt{\gamma R T} \tag{2.10}$$

$$U = Ma \tag{2.11}$$

The change in viscosity due to the drop in static temperature was computed from the Sutherland law as,

$$\mu = \mu_{ref}\left(\frac{T}{T_{ref}}\right)^{\frac{3}{2}}\frac{T_{ref} + S}{T + S} \tag{2.12}$$

where $T_{ref} = 273.15$ K is the reference temperature, $\mu_{ref} = \mu(T_{ref}) = 1.716 \cdot 10^{-5}$ Kg/m·s is the viscosity at the reference temperature, and $S = 110.4$ K is the Sutherland constant for air. Finally, the unit Reynolds number Re and the Knudsen number Kn were computed as,

$$Re = \frac{\rho U}{\mu} \tag{2.13}$$

$$Kn = \frac{M}{Re}\sqrt{\pi\frac{\gamma}{2}} \tag{2.14}$$

Note that the Reynolds number in Equation 2.14 is based on the 0.00015 in.-dia. of the cold-wire and the stagnation conditions in front of the wire.

Figure 2.13 shows the Mach number and Kn variation during the course of a run with initial stagnation pressure $p_{0,i} = 24$ psi and stagnation temperature $T_{0,i} = 297$ K. Using the Knudsen number variation during the course of the run from Figure 2.13, an linear approximation for the change in η from 0.98 to 1.01

was extrapolated from Figure 2.4 in Ref. [41] at $M \approx 4.1$. The total temperature drop T_0 shown in Figure 2.14 was computed by multiplying the cold-wire recovery temperature by η. Note that since the theoretical approximation was very similar to the experimental total temperature, only one of every 2000 total temperature data points were plotted in Figure 2.14.

All flow variables for a typical run starting at $p_{0,i} = 24$ psi, $T_{0,i} = 297$ K, before repolishing the nozzle, are plotted in Figures 2.15 through 2.18.

The supersonic flow in the tunnel typically lasts between 4 and 5 seconds. The total pressure drops by approximately 48% of the initial total pressure depending on the length of the run. The passage of the expansion waves results in a series of approximately 0.125 s steps. The total pressure, measured at the entrance of the contraction, drops between 1.8% and 1.0% across each step. The total temperature also decreases in the same step pattern by approximately 15% during the first $3-3.5$ s of the run. However, for the remaining 1.5 s, it stabilizes rather chaotically at a temperature around $T_{0,i} \cdot 0.85$. The drop in pitot pressure due to the passage of the expansion waves ranges from 1.1% to 2.0% of the initial pitot pressure per step for a total drop of approximately 48% during a run.

To determine whether the high freestream noise levels at low initial total pressures were related to the small step in the nozzle throat, the contraction and nozzle sections were repolished. The 0.067 in.-dia. pitot probe was mounted in the test section and calibrated by monitoring its output along with the output of a Paroscientific Model 740-30A Digiquartz Portable Standard pressure transducer as the tunnel was pressurized from 0.1 psi to 15 psi. The calibration curve obtained using this gauge had an offset of 0.45 psia compared to the curve obtained using the Wika analog gauge. Figure 2.19 shows a typical set of calibrated pressure data from runs at three different initial driver pressures. The levels of freestream noise during 12 individual runs were measured along with the mean Mach number and are plotted in Figures 2.20 and Figure 2.21. The legend refers to the initial driver pressure for each run and the data displayed are only computed between 0.4 s and 2.4 s after

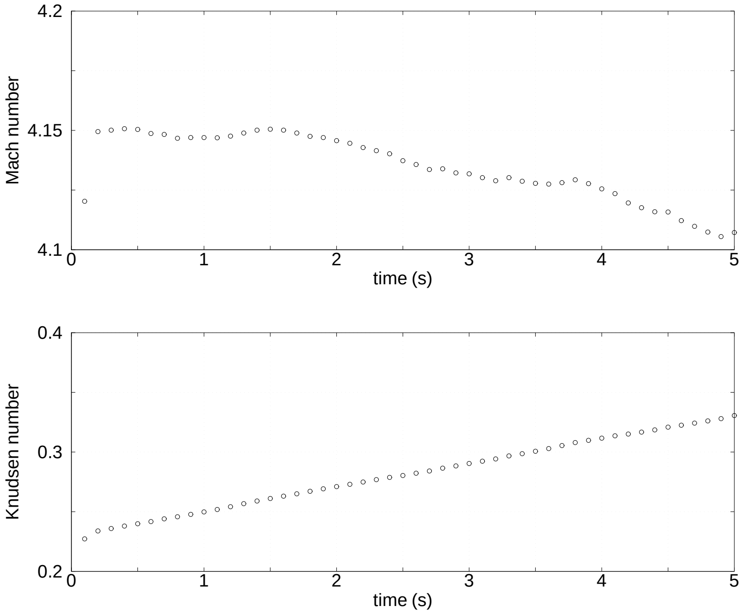

Figure 2.13: Mach number and Knudsen number throughout a run with initial stagnation pressure $p_0 = 24$ psi and stagnation temperature $T_{0,i} = 297$ K

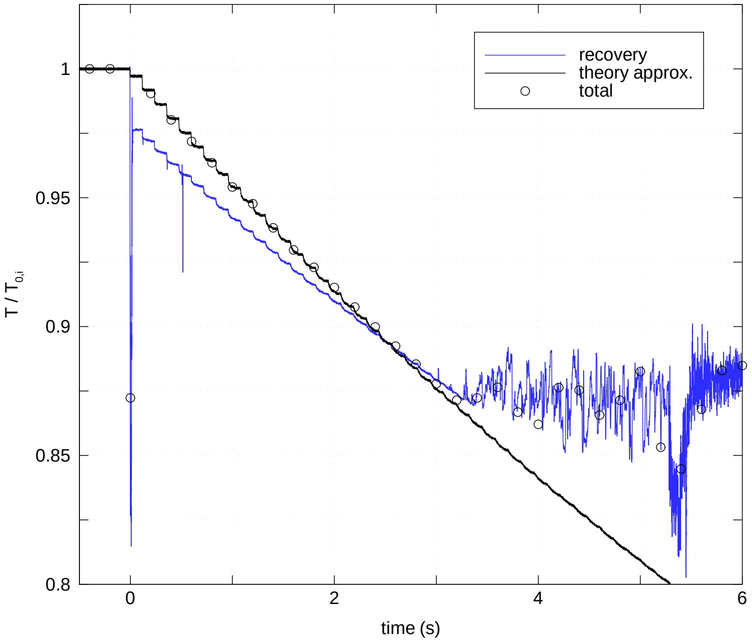

Figure 2.14: Final adjusted total temperature

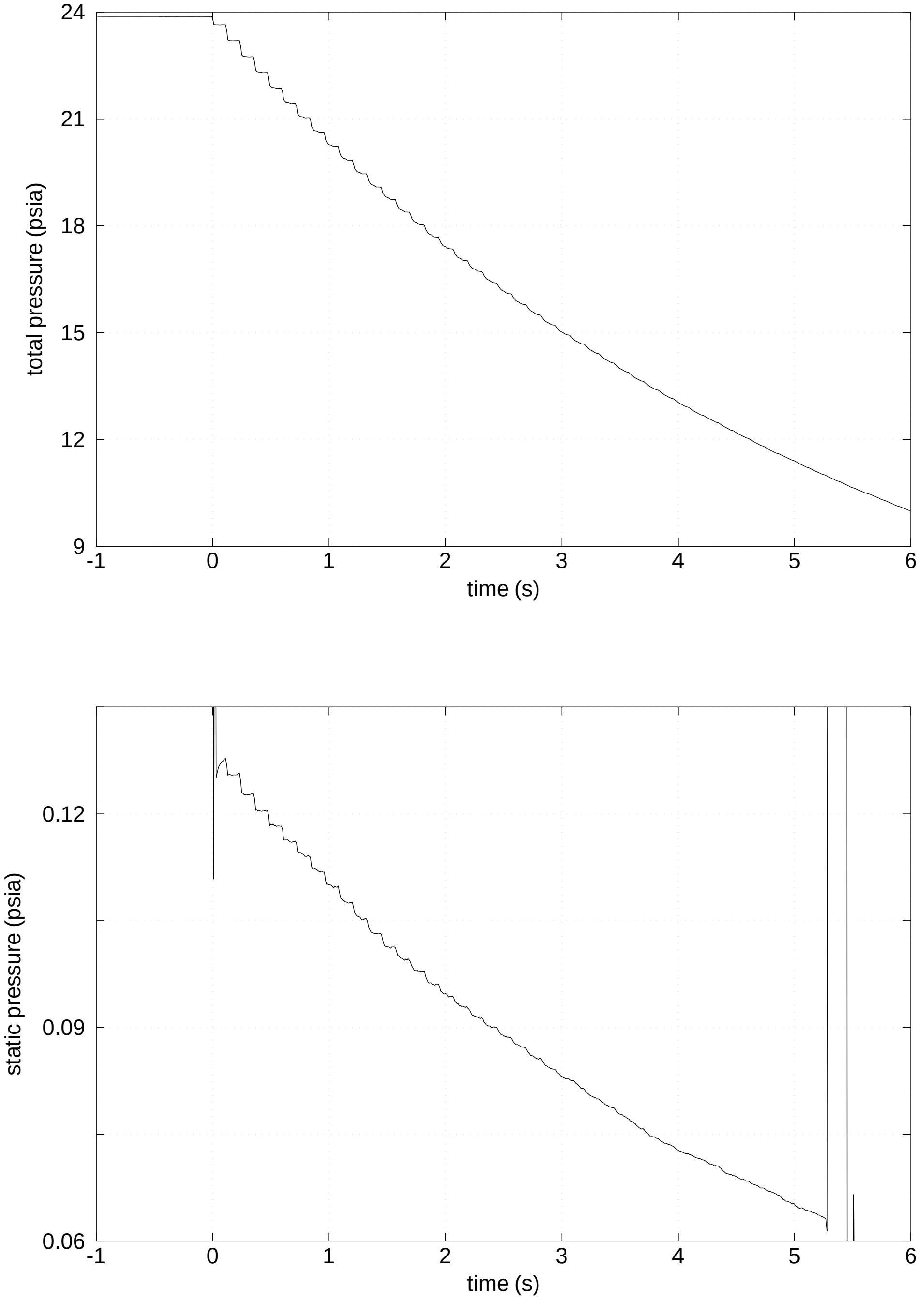

Figure 2.15: Pressure drop throughout tunnel run before repolishing the nozzle. $p_{0,i} = 24$ psi, $T_{0,i} = 297$ K.

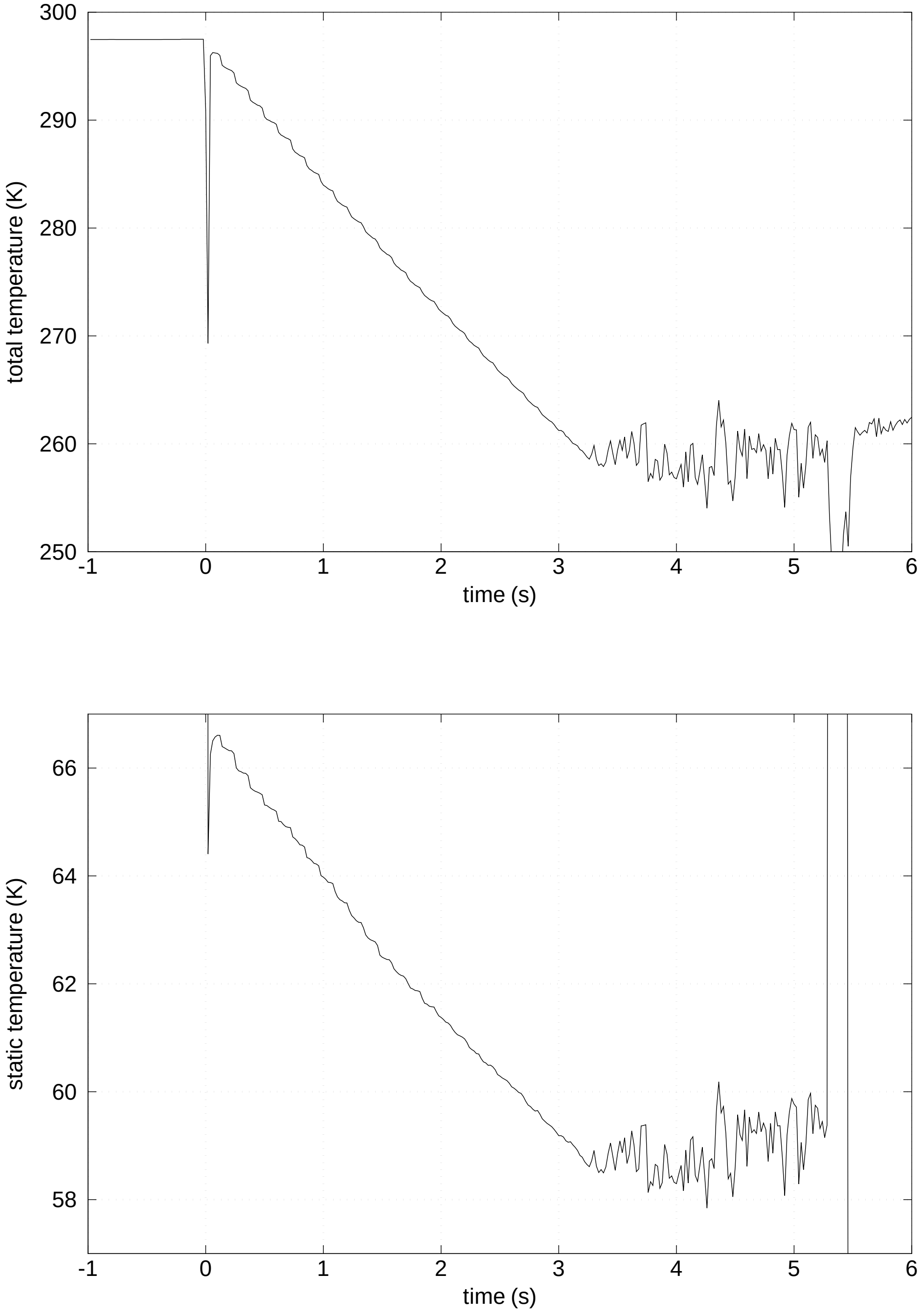

Figure 2.16: Temperature drop throughout tunnel run before repolishing the nozzle. $p_{0,i} = 24$ psi, $T_{0,i} = 297$ K

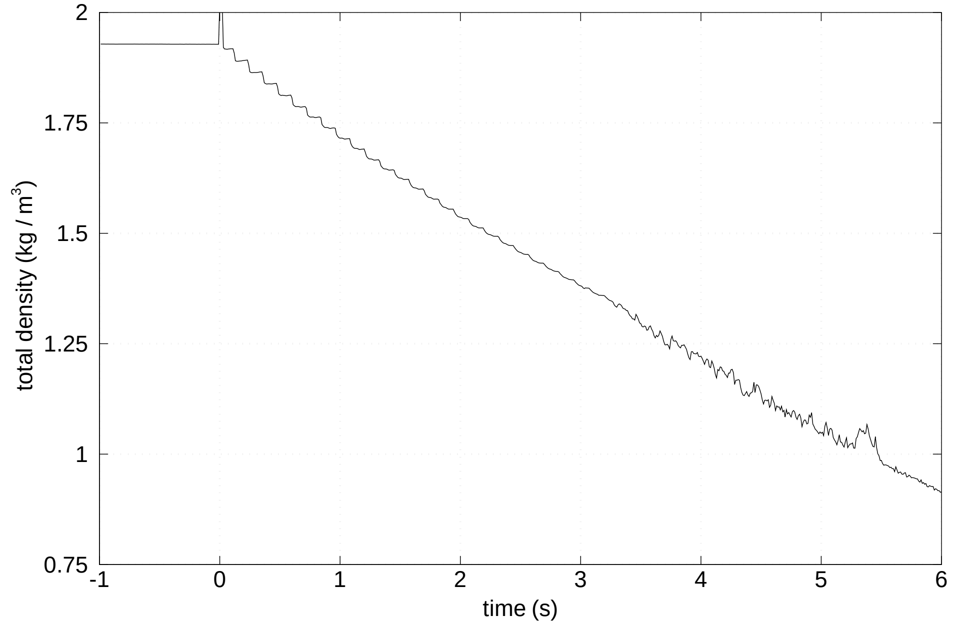

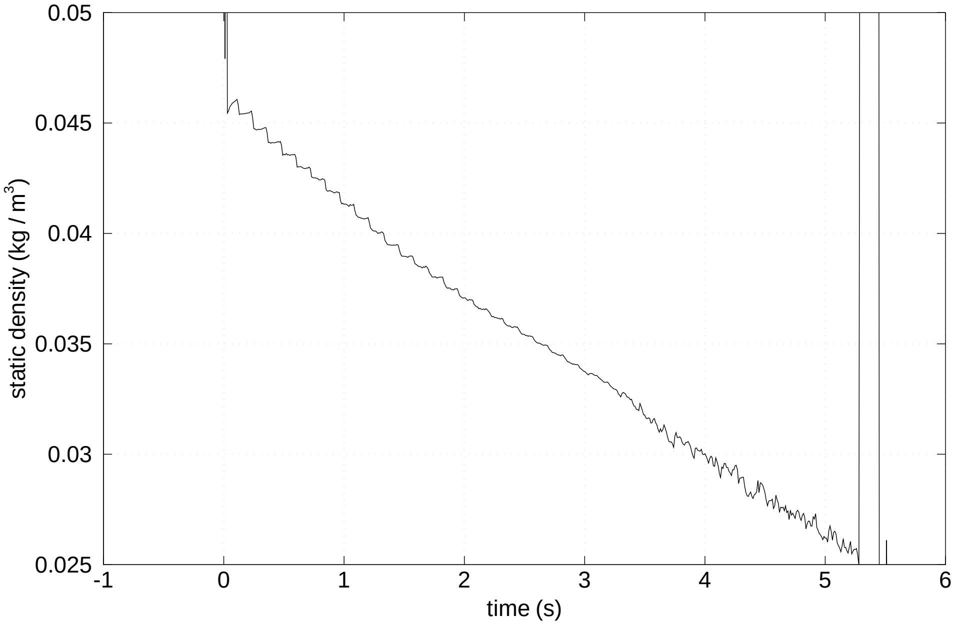

Figure 2.17: Density drop throughout tunnel run before repolishing the nozzle. $p_{0,i} = 24$ psi, $T_{0,i} = 297$ K

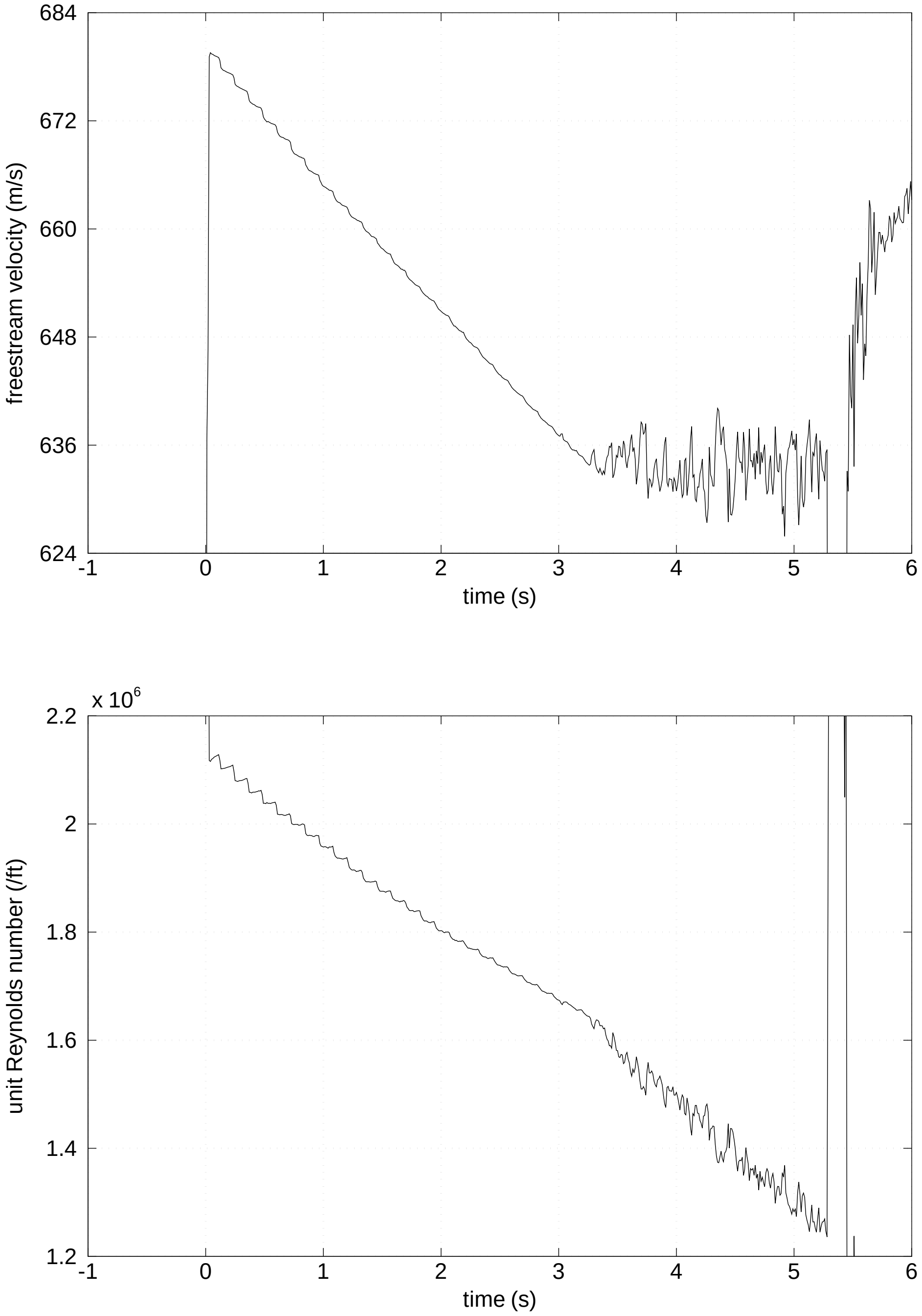

Figure 2.18: Velocity and unit Reynolds number throughout tunnel run before repolishing the nozzle. $p_{0,i} = 24$ psi, $T_{0,i} = 297$ K

supersonic flow is established in the test section. Again, this window was chosen because the shortest run made was slightly longer than 2.8 s. Note that, on average, tunnel runs became approximately 20% shorter after repolishing the nozzle except for the shortest run which was almost 35% than the shortest run before the repolish. The cause for the decrease in run length is unknown. Clearly, the step in the nozzle had a strong effect in the freestream noise. After repolishing the nozzle, freestream noise values very similar to those obtained in the past by Munro, Schneider, and Haven were measured [36–39]. Without the step in the nozzle throat, the freestream noise decreases as initial driver pressure decreases even at low initial pressures. The Mach number decreases about 2.5% during the tunnel run. The source of this variation is not known and may not be physical. It is possible that calibration and data processing errors are the reason why the mean Mach number changes.

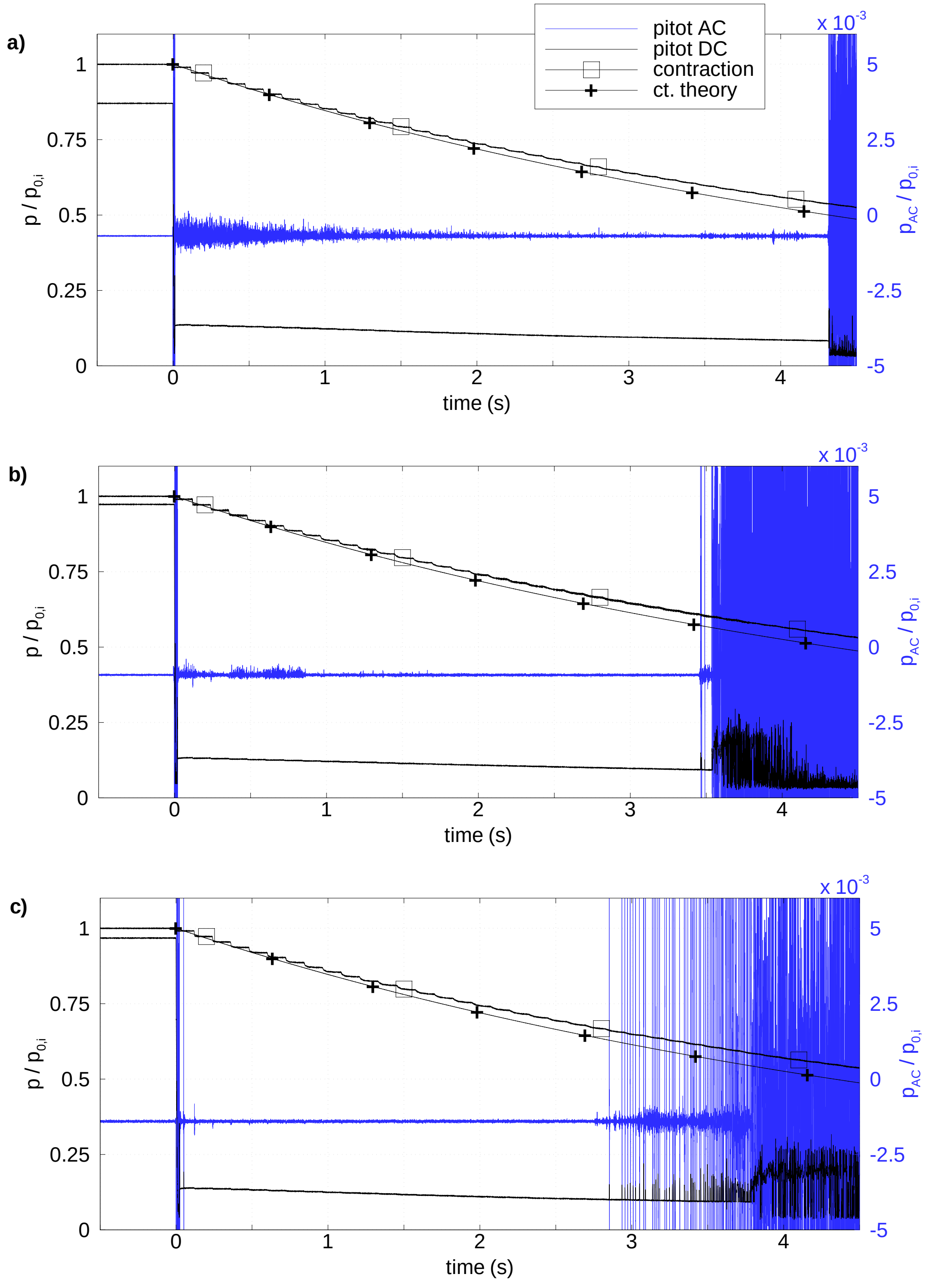

Figure 2.19: Typical pitot and contraction pressure traces after repolishing the nozzle: a) $p_{0,i} = 16$ psi, b) $p_{0,i} = 12$ psi, c) $p_{0,i} = 8$ psi

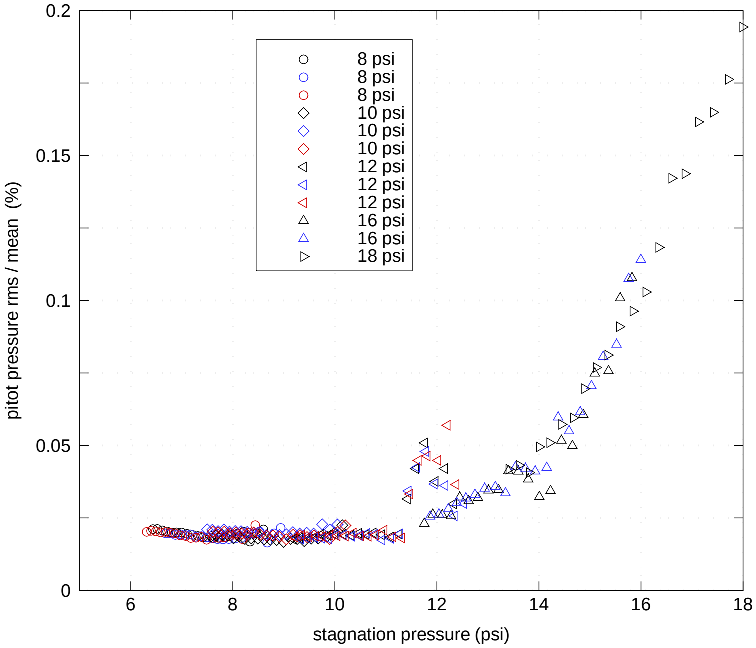

Figure 2.20: Freestream noise level in the PQFLT measured with 0.067 in.-dia. pitot probe after repolishing the nozzle

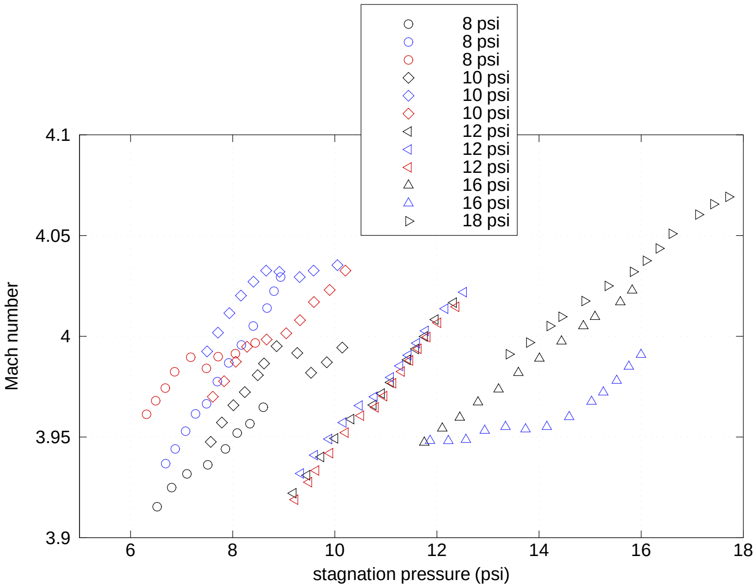

Figure 2.21: Mach number inside the PQFLT test section after repolishing the nozzle

3. Instrumentation

3.1 Test Models

3.1.1 Forward-Facing Cavity

A forward-facing cavity was used to test the performance of the LDI, as shown in Figure 3.1. The forward-facing cavity is simply a hemisphere with a circular hole drilled in its center. The cavity depth could be adjusted between 0 and 3 D. A larger model (shown in Figure 3.2) was designed for experiments in the BAM6QT, permitting a maximum cavity depth of 5 D.

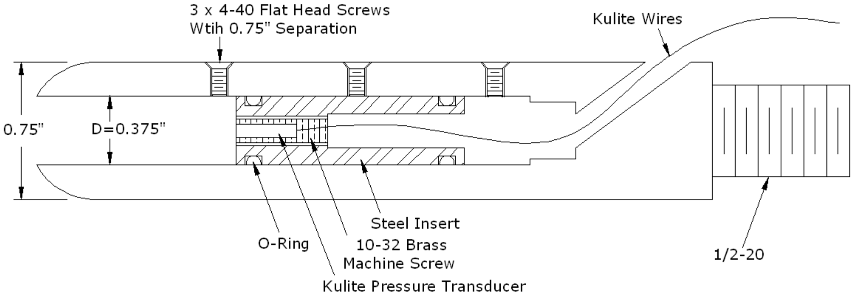

Figure 3.1: Forward-facing cavity model tested in the PQFLT

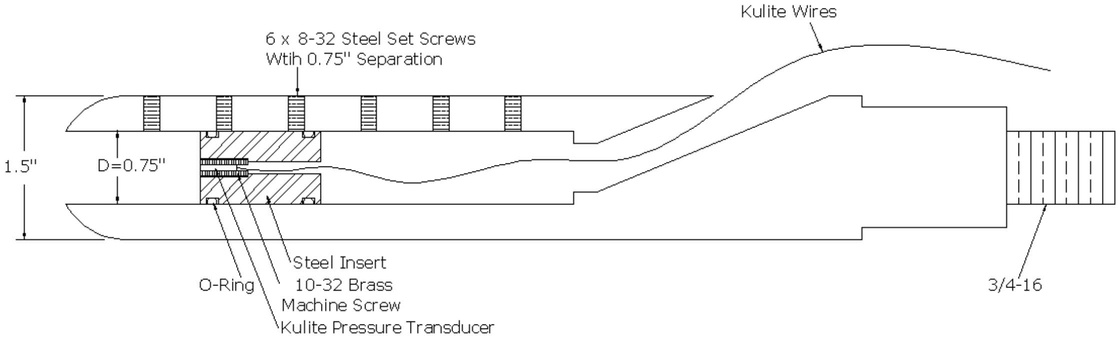

Figure 3.2: Forward-facing cavity model to be tested in the BAM6QT

3.2 Vibration Isolation System

The optical table in the BAM6QT was installed on a four-isolator vibration control system (Newport Model: Stabilizer I-2000) previously used by Salyer and others in the PQFLT. When the BAM6QT was built, Shin Matsumura transferred the isolators from the PQFLT to the BAM6QT, but plumbing to pressurize them was not completed until now. The reader can refer to Newport's documentation for detailed installation procedures [42]. This particular system, however, does not have the isolators directly attached to the optical table. This table sits on top of two rails that allow it to slide axially, so the optical system can evaluate different areas of the test section (see Figure 3.3). In order to accommodate the system to the sliding rail mechanism, the support plates that attach to the table in the original design were removed, and the isolator legs were directly bolted to the rails as shown in Figure. 3.4. Hence, the leveling procedure suggested in the Newport instruction manual varies slightly. To adjust the leveling of these isolators, the four bolts attaching each isolator to the rail must be removed. One of the custom leveling wrenches shown in Figure 3.5 is used to hold the hex nut stationary and the prongs of the second wrench are inserted into the holes of the plate holding the rail (see Figure 3.6). The plate is then rotated using the top wrench to adjust the height. The air that pressurizes the isolators comes from the main compressor line to the BAM6QT driver tube via an air pressure regulator (McMaster-Carr part. 4959K301). The regulator was set to about 16 psig to stabilize the system.

3.3 Laser differential interferometer

The LDI is a non-intrusive optical flow diagnostic that detects minute changes in the density of the medium. Unlike the usual full-field interferometry, the LDI only looks at a single integration line. However, it is superior to the other techniques in the sense that the frequency response of the receiving electronics is the only limitation to the system's bandwidth, and it has a high axial spatial resolution that can be

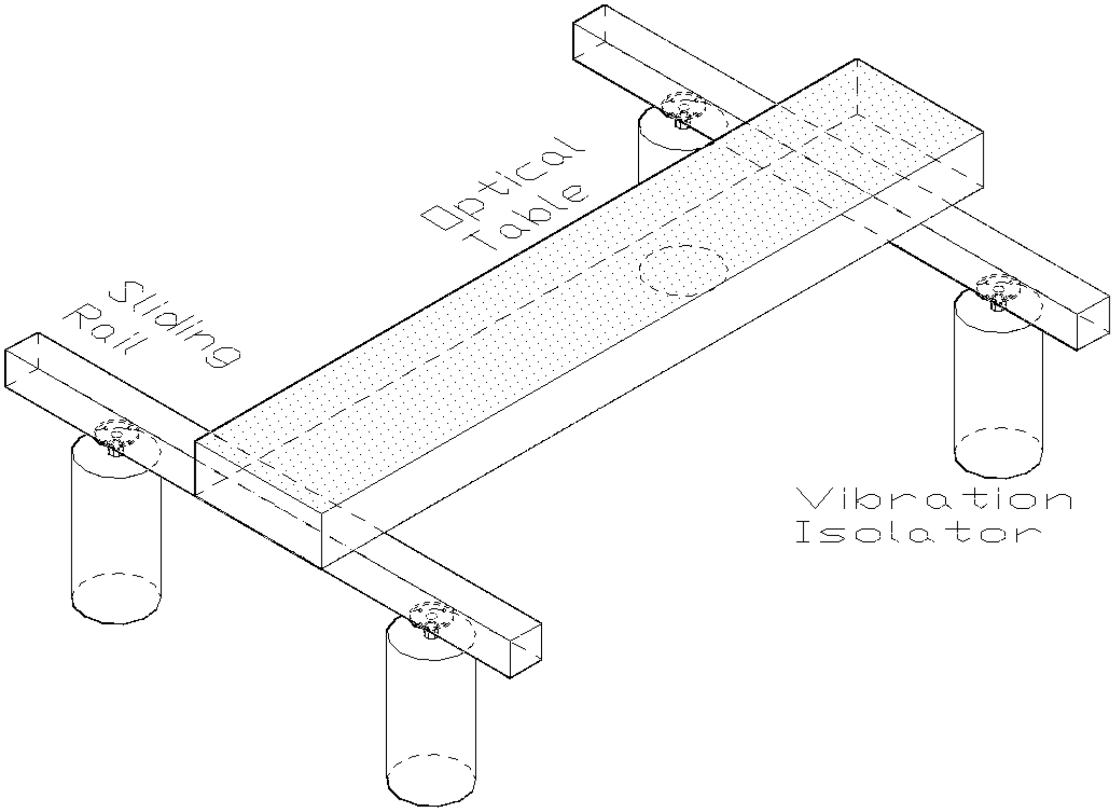

Figure 3.3: Schematic of vibration isolation control system in the BAM6QT

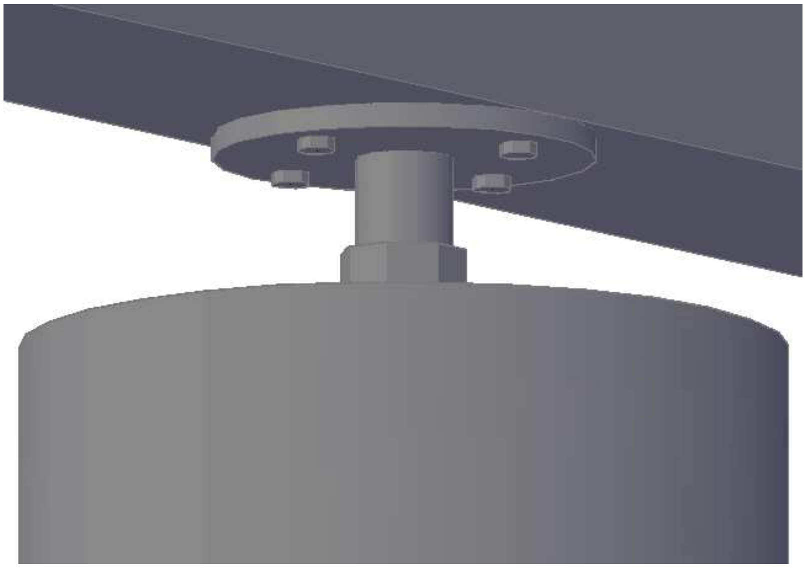

Figure 3.4: Individual isolator attachment to sliding rail

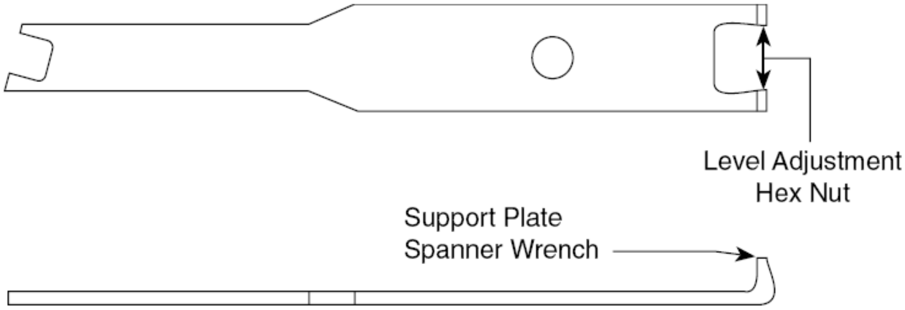

Figure 3.5: Isolator leveling wrench (Ref. [42])

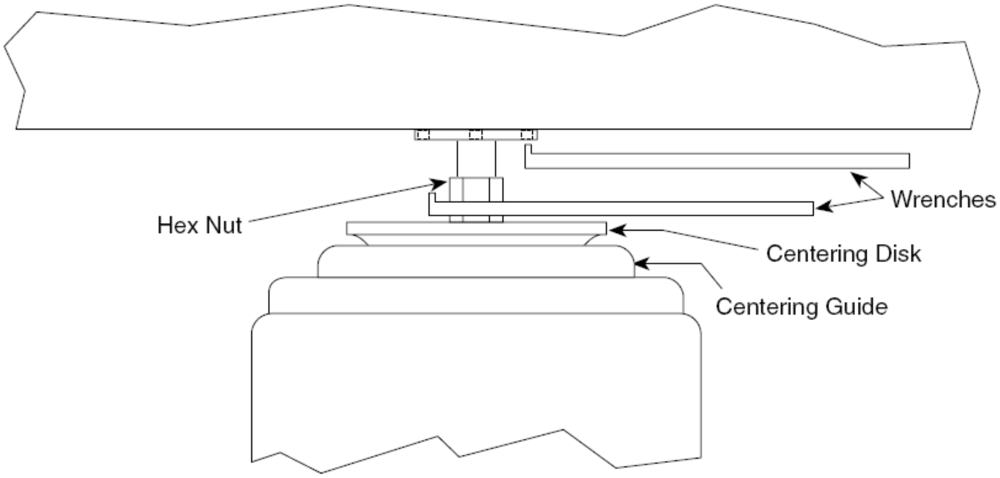

Figure 3.6: Isolator level adjustment (Ref. [42])

easily adjusted with the optical components that focus the laser beams. On the other hand, the transverse spatial resolution of the LDI is limited and considered to be the main drawback of the instrument. This is because the LDI output is affected by the whole integration line of the laser beams (see Figure 3.7). Hence, density fluctuations in the boundary layer of the tunnel windows are picked up by the LDI as well.

The basic LDI system works by sending two parallel laser beams through the flow which are later reunited to a single beam. This beam is then split into two beams

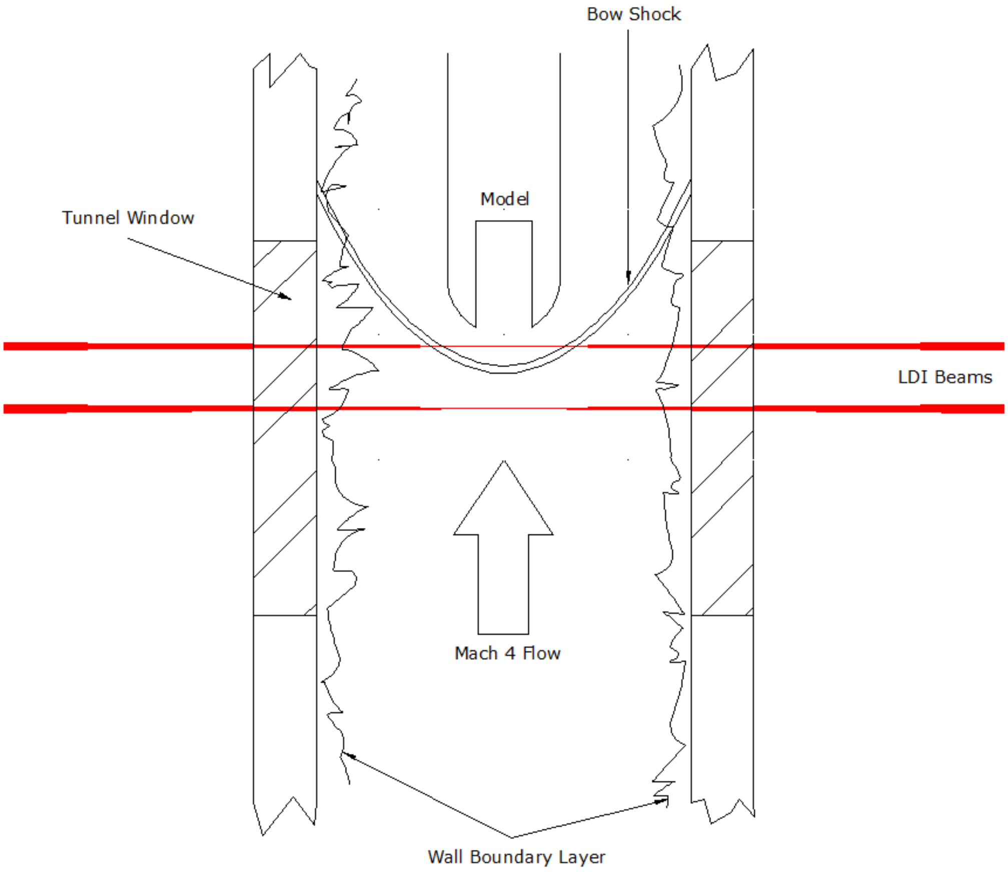

Figure 3.7: Schematic of LDI integration path

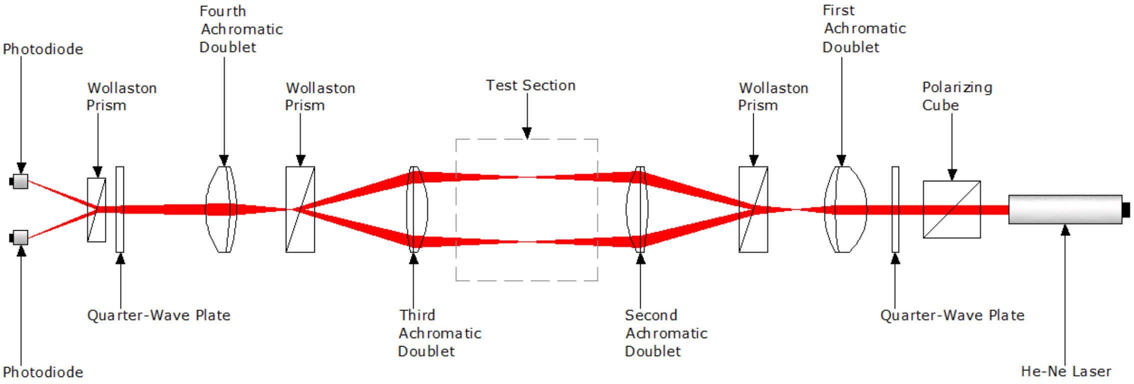

Figure 3.8: Schematic of basic LDI

with complementary interference patterns. The two resulting beams are focused onto a pair of photodiodes whose currents are subtracted and their difference is recorded.

A schematic of the basic LDI setup is shown in Figure 3.8. Note that some of the figures displayed in this report were based on those reported by Salyer. Nevertheless, they were all made specifically for this project by the author. A Melles Griot 25-STP-912-249 stabilized He-Ne laser generates the linearly polarized source beam.

A polarizing cube is placed immediately after the laser system. Although it is not required for the performance of the basic LDI system, the polarizing cube is used in combination with the next component, a quarter wave plate. The purpose of this component is to isolate the laser from back reflections resulting from other optical elements or windows that could make the laser unstable if allowed to pass back into the laser system. With these two components in place, the polarization of all back reflections is rotated by the quarter wave plate. The polarizing cube then deflects them by 90 deg, driving them away from the laser cavity.

The quarter wave plate, if oriented correctly, is used primarily to convert the polarization of the beam to circular polarization. Though also not essential for the proper function of the system, this is a convenient component to have because a circularly polarized beam allows for the easy adjustment of beam separation orientation in the test section. With the quarter-wave plate included in the system, the orientation of the separation of the beams can be precisely adjusted by rotating the first wollaston prism. This is a more precise method than rotating the laser system (which lacks a mechanical optical mount with precise rotation capabilities) to a linear polarization aligned at 45 deg from the wollaston prism's optical axis. With the LDI assembled as shown in Figure 3.8, and the quarter wave plate oriented correctly, the first wollaston prism will always generate two beams of equal intensity whose separation orientation can be adjusted by rotating the prism in its rotational optical mount.

The first achromatic doublet works in conjunction with the second achromatic doublet to focus the parallel beams inside the test section. The reader can refer to Appendix A for drawings with actual component distances and optical values calculated and chosen using the well known lens maker's equation. For two multiple lens systems separated by a distance d, the distance from the surface on the lens system furthest away from the light source, to the focal point of the optical system known as its back focal length (BFL) is given by (Ref. [43] chapter 5-2)

$$BFL = \frac{f_\beta(d-f)}{d-(f_\alpha+f_\beta)}, \tag{3.1}$$

where f_α, f_β are the effective focal lengths of the first and second lens systems, and $d > f_\alpha$, $d > f_\beta$. The importance of focusing the beams at a specific location inside the test section will be further explained with the placing of the last achromatic doublet.

The interferometer section of the system begins when the beam passes through the first wollaston prism. The prism splits the source beam into two beams of equal intensity and orthogonal linear polarizations separated by an angle.

The second achromatic doublet is placed after the first wollaston prism at a distance from the prism exactly equal to its focal length. This lens is used to collimate the diverging beams coming from the wollaston prism. The separation angle between the beams emerging from the wollaston prism is chosen depending on the desired parallel beam spacing inside the test section.

After the two parallel beams are focused at the desired location and leave the test section, they pass through the third achromatic doublet which redirects them so they reunite at its focal point.

The second wollaston prism, placed following the third achromatic doublet and at a distance exactly equal to its focal length, makes the two beams coincident. Note that the beams have orthogonal linear polarizations, hence despite their coincidence they do not interfere. At this point, the interferometer portion of the system ends.

The coincident beams proceed to pass through the fourth achromatic doublet. This lens, in conjunction with the three-lens system preceding it, focuses the final beams through the remaining optical components onto the surface of the photodiodes. To calculate the precise location of this component refer to Equation 3.1. Note that the LDI works by detecting phase changes between the beams traveling through the flow in question. These phase changes are caused by index of refraction fluctuations, caused in turn by density fluctuations in the flow through the laser beams' integration paths. Recall however, that index of refraction gradients also cause light rays to bend allowing for schlieren effects. To optimize the performance of the LDI, schlieren effects are minimized by focusing an image of the flow in question onto each photodiode. This is why the first and last lenses are referred to as the imaging lenses of the system and why the beams are focused at specific locations in the test section and on the surface of the photodiodes. This optical system focused the beams to a spot size of about 0.1 mm inside the test section.

After the fourth achromatic doublet (second imaging lens), both coincident beams pass through the second quarter-wave plate. Once again, the quarter-wave plate changes the polarization of the beams from linear to circular making them spatially coherent and able to interfere with each other. The degree of spatial coherence of the beams depends on the orientation of the quarter-wave plate. Hence, it must be carefully adjusted to achieve maximum fringe contrast.

Once the two beams are both coincident and spatially coherent, they pass through the third and last wollaston prism which generates two beams with complementary interference patterns that are focused on the surface of the photodiodes.

The He-Ne laser beam's wavelength $\lambda = 633.2$ nm falls in the single photon absorption spectral range ($300 - 1050$ nm) of the silicon photodiodes in the photo detector used in this experiment. This means that a single photon with a wavelength in this range will excite an electron on the valence band enough to overlap the gap to the conduction band of the diode. Hence, the rate at which this diode produces electrons is linearly proportional to the irradiance of the laser beam. Now, for two interfering, spatially coherent beams with equal irradiance contributions $I_S = I_R = I_0$ (true when the first quarter-wave plate is oriented correctly) and a relative phase shift $\delta\varphi$ (in radians), the total irradiance is given by (Ref. [43] chapter 9-1)

$$I = 4I_0cos^2\left(\frac{\delta\varphi}{2}\right) \tag{3.2}$$

Thus, the non-dimensional normalized induced voltages from the first and second photodiodes are respectively given by

$$\frac{E1}{E1_{max}} = cos^2\left(\pi\frac{\delta\Phi}{\lambda}\right), \tag{3.3}$$

$$\frac{E2}{E2_{max}} = cos^2\left(\pi\frac{\delta\Phi}{\lambda} + \frac{\pi}{2}\right) = sin^2\left(\pi\frac{\delta\Phi}{\lambda}\right), \tag{3.4}$$

where $E1_{max}$ & $E2_{max}$ are the maximum voltages induced by the first and second photodiodes respectively, $\delta\Phi$ is the optical path length difference (OPD) between the beams (in nm), and $\lambda = 632.8$ nm is the wavelength of the laser. Note that with equal fringe contrast at both photodiodes (when the second quarter-wave plate is oriented correctly), $E1_{max} = E2_{max}$.

In simple terms, the fact that the two resulting beams that shine on the photodiodes have complementary interferences means that when the two spatially coherent, interfering beams are aligned to infinite fringe spacing, the patterns shining on the photodiodes are shifted by one fringe. That is, when a bright fringe shines on the first photodiode because there is no relative phase shift between the beams in the test section and they interfere 100% constructively, there will be a dark fringe shining on the second photodiode. Now, when a phase shift between the beams in the test section is introduced, the irradiance will decrease at the first photodiode and increase by exactly the same amount at the second photodiode as shown in Figure 3.9.

The balanced photo receiver in the LDI subtracts the photocurrent produced by the first photodiode from the photocurrent produced by the second photodiode and outputs the voltage difference. The optical path length difference between the beams in the test section and the voltage generated by the balanced photo detector are related by subtracting Equations 3.3 & 3.4 as shown in Figure 3.10.

In this research the LDI was used to detect rather small changes in the density of the flow that are manifested in small index of refraction fluctuations that in turn cause small phase shifts between the beams in the test section. For this reason, it is convenient to use only the linear portion of the photodiodes' induced voltage difference, as shown in Figure 3.10. Also note that this is where the system is the most sensitive to relative phase shift fluctuations. This linearized relation between relative phase shift and output voltage is thus given by

$$\frac{E}{E_0} = \pi \frac{\delta\Phi}{\lambda} \Rightarrow \delta\Phi = \frac{\lambda}{\pi}\frac{E}{E_0}, \tag{3.5}$$

where E is the induced voltage difference from the photo receiver's output and E_{max} is the maximum voltage swing of the receiver's output. This value is called the calibration voltage of the system and is equal to $E1_{max} + E2_{max}$. Equation 3.5 is valid over a region of approximately $\lambda/10$, thus the calibrated output of the system is quantitative (see Figure 3.10).

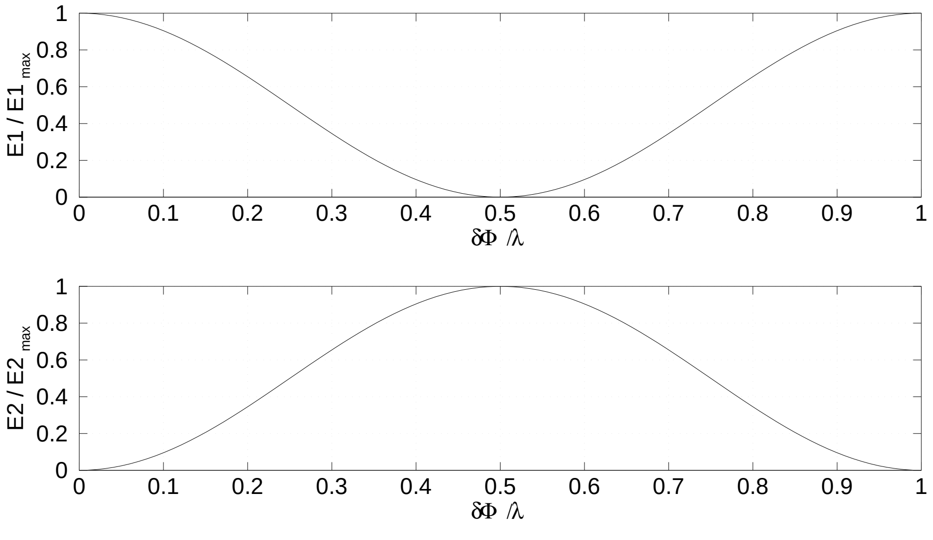

Figure 3.9: Interference slopes for individual photodiodes

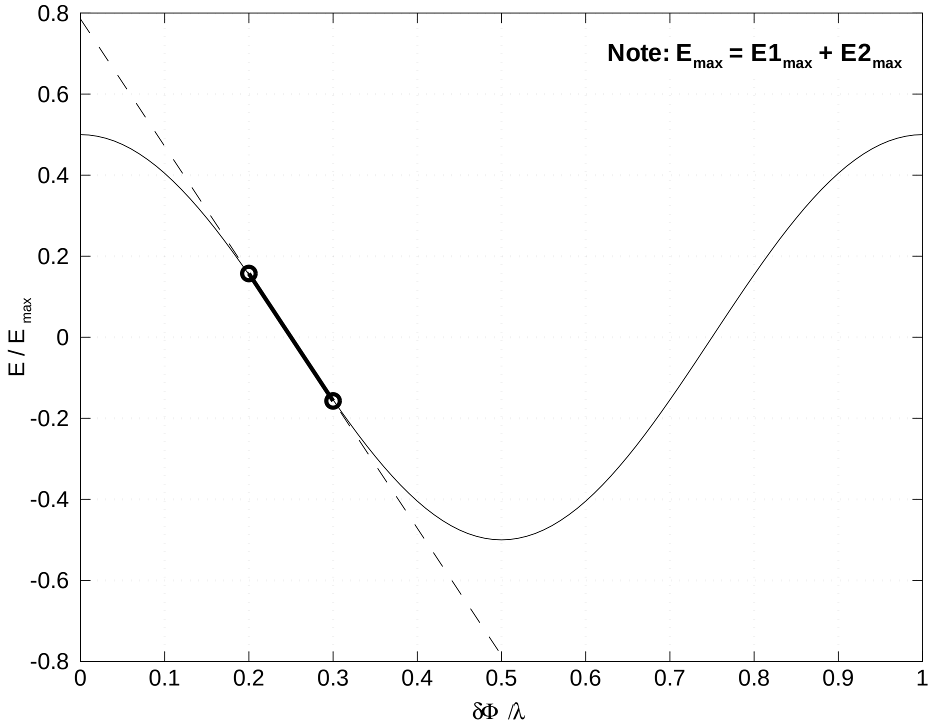

Figure 3.10: Interference slope for differenced photodiodes

For a detailed LDI alignment procedure refer to Appendix C. Appendices A & B also contain drawings with precise optical component locations as well as high resolution photographs of the system.

3.4 Balanced Photodiode Receiver

A New-Focus Model 1807-FS Balanced Photodiode Receiver was used as the photodetector for the LDI. This was an upgrade from the home-built photoreceivers that Salyer used for his research in the PQFLT [15–18]. Recall that the function of this receiver is to subtract the photocurrent generated by the two photodiodes. By doing this, common-mode-noise (such as laser-intensity noise) that is present on both the reference and signal beams is canceled out and suppressed from the signal. In addition, a signal twice as large in amplitude is obtained. The receiver consists of two matched photodiodes and a high-frequency amplifier that generates an output voltage proportional to the difference between the photocurrents produced by the photodiodes, as shown in Figure 3.11.

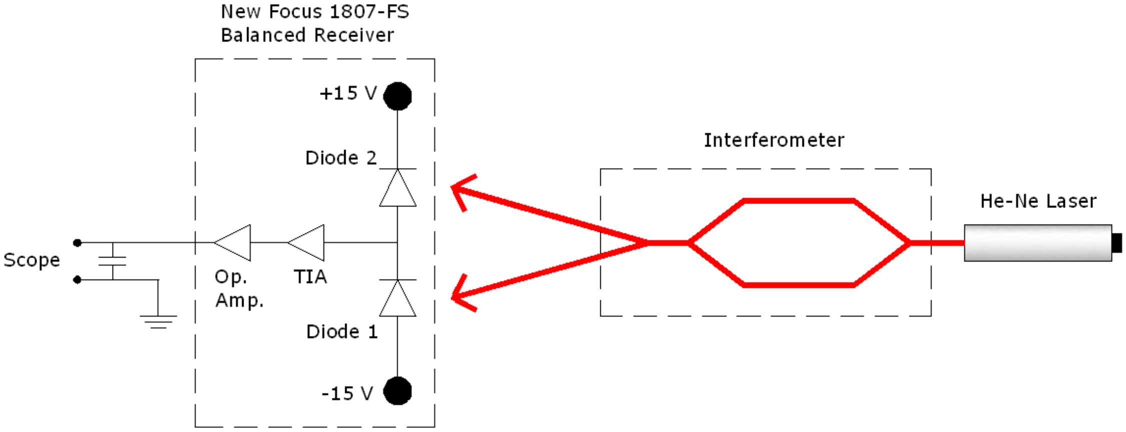

Figure 3.11: Schematic of balanced photoreceiver electronics

According to the manufacturer, the frequency response of the photoreceiver shown in Figure 3.12 displays a drop of 3.0 dB between 80 and about 100 MHz [44].

Measurements of the noise in the LDI signal were made in both the PQFLT and the BAM6QT experimental facilities. Furthermore, measurements with and without vibration damping were also made to observe the effect of the vibration control system on the LDI performance. Figure 3.13a shows a 0.2 s LDI calibrated optical path difference output signal, sampled at 125 KHz, while both beams were passing through stagnant room air in the PQFLT. To estimate the peak-to-peak amplitude of the noise, the very low frequencies were canceled by subtracting from the data a running average with a window size equal to 1% of the number of data points in the set as shown in Figure 3.13b. The power spectrum of the noise is shown in Figure 3.13c. Note the large-amplitude, low-frequency noise in the signal. The

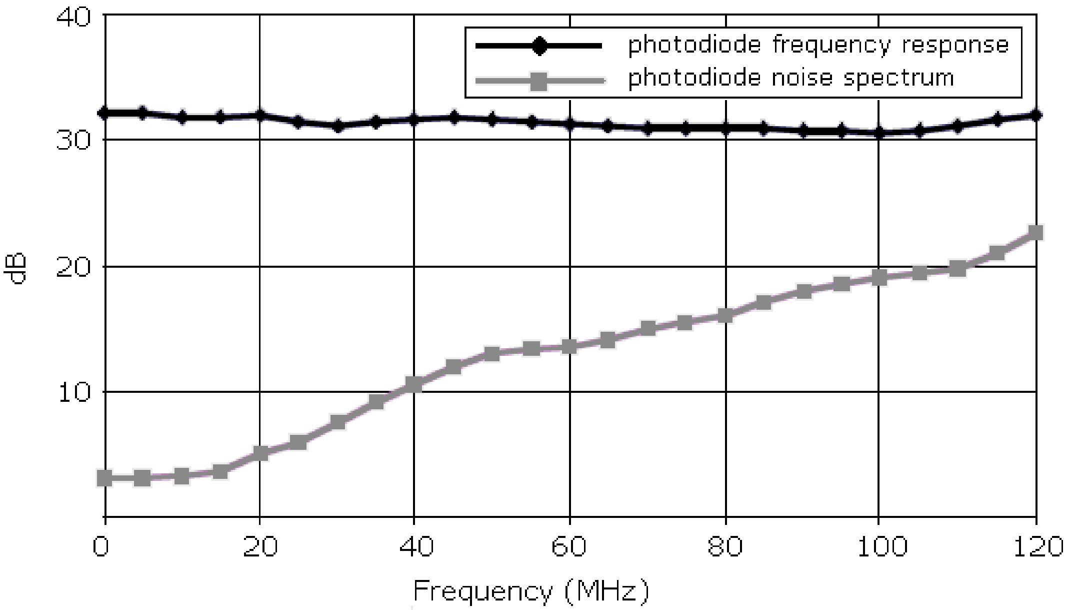

Figure 3.12: Frequency response and typical noise spectrum of photoreceiver (Ref. [44])

author believes that mechanical vibrations in the room or in the optical mounts are the primary source of this noise. It has a pronounced resonant frequency of about 425 Hz with an amplitude of approximately $2 \cdot 10^3$ nm^2/Hz. A closer look was taken at similar data and the high-frequency noise was analyzed. The instabilities that the LDI is intended to detect, happen at a far smaller time scale than the time scale at which mechanical vibrations do. Thus, the minimum optical path length difference detectable by the LDI, for the purposes of this research, is determined by the peak-to-peak amplitude of this high-frequency noise. Figure 3.14b shows a 1 ms calibrated set of filtered LDI data, sampled at 500KHz (filtered in the same fashion as the low-frequency noise data). Hence, the LDI, as it was setup in the PQFLT, has a minimum detectable optical path length difference of approximately $\lambda/21,000$, obtained by dividing the amplitude of the noise by λ. The root-mean-square (RMS) of the noise was 0.39 mV. This is an improvement from Salyer's active photodiode receiver capable of detecting optical path length differences as small as

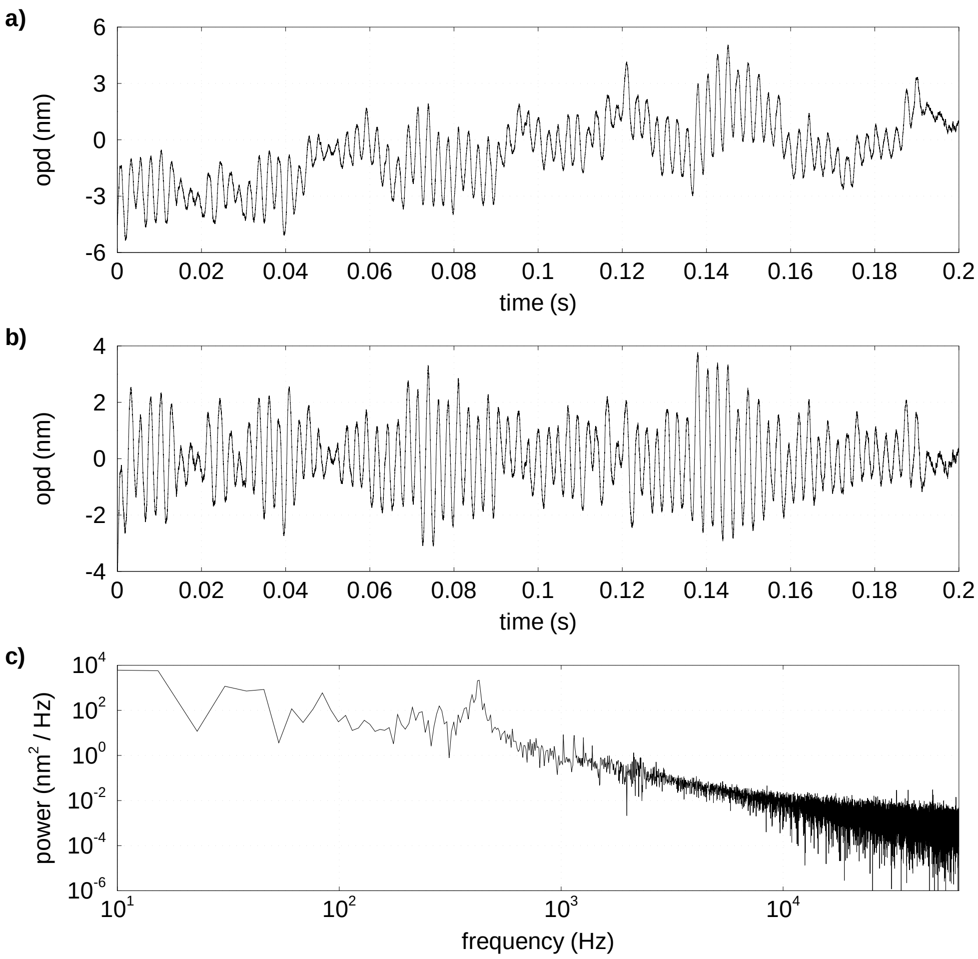

Figure 3.13: LDI noise due to vibrations in the PQFLT laboratory: a) raw noise trace, b) raw signal minus running average, c) noise power spectrum

$\lambda/13,000$ with a noise RMS value of 0.84 mV (Ref. [17] pg. 42). Note, however, that Salyer used alternating high-performance LED lamps to measure the bandwidth of the system and the peak-to-peak amplitude of the electrical noise as opposed to the signal of the feedback stabilized LDI. Although it would be expected that more sources of noise affect the signal of the feedback stabilized LDI than those that affect the signal from a pair of alternating LED lamps shining on the photoreceiver, the sampling frequencies are not the same and the data obtained from each are not precisely comparable.

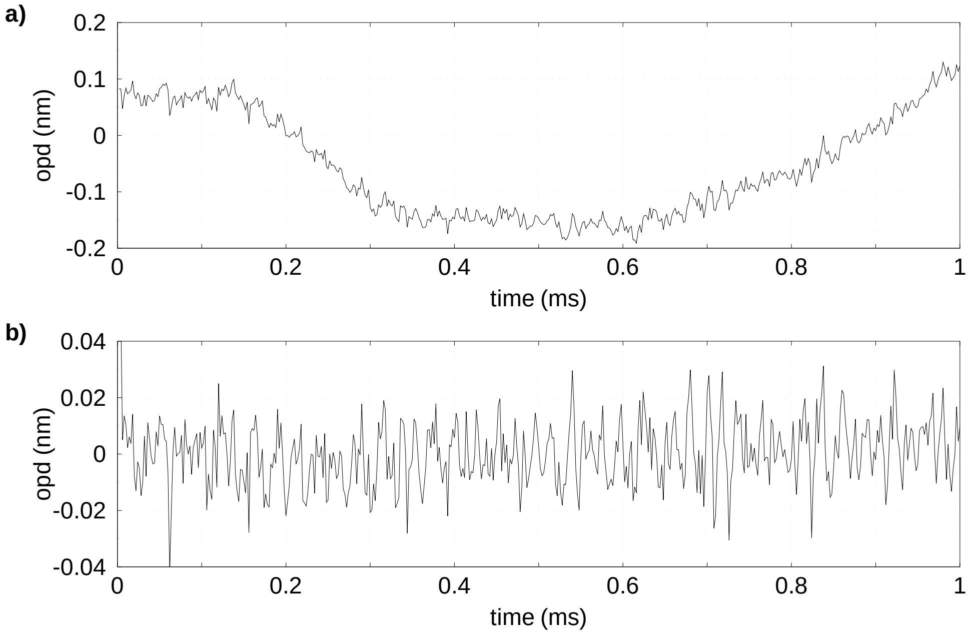

Figure 3.14: LDI electrical noise in the PQFLT: a) raw noise trace, b) raw signal minus running average

Similar measurements were made in the BAM6QT without vibration control on the system. Figures 3.15b and Figure 3.15c show a 0.2 s filtered LDI output signal, sampled at 1 MHz, and its power spectrum while both beams were passing through stagnant room air in the BAM6QT. Note that the signal has a pronounced resonant frequency of about 235 Hz with an amplitude of approximately 10^5 nm^2/Hz. The cause for the difference in low frequency noise in the PQFLT and the BAM6QT is not known. Figure 3.16b shows a 1 ms calibrated set of filtered data for the high-frequency noise detected by the LDI, sampled at 1 MHz, in the BAM6QT. Thus, the LDI, as it was setup in the BAM6QT without vibration control, also has a minimum detectable optical path length difference of approximately $\lambda/21,000$. Furthermore, the root-mean-square (RMS) of the noise shown in Figure 3.15b was also 0.39 mV.

Finally, measurements were made in the BAM6QT with the vibration isolation system. Figures 3.17b and Figure 3.17c show a 0.2 s filtered LDI output signal,

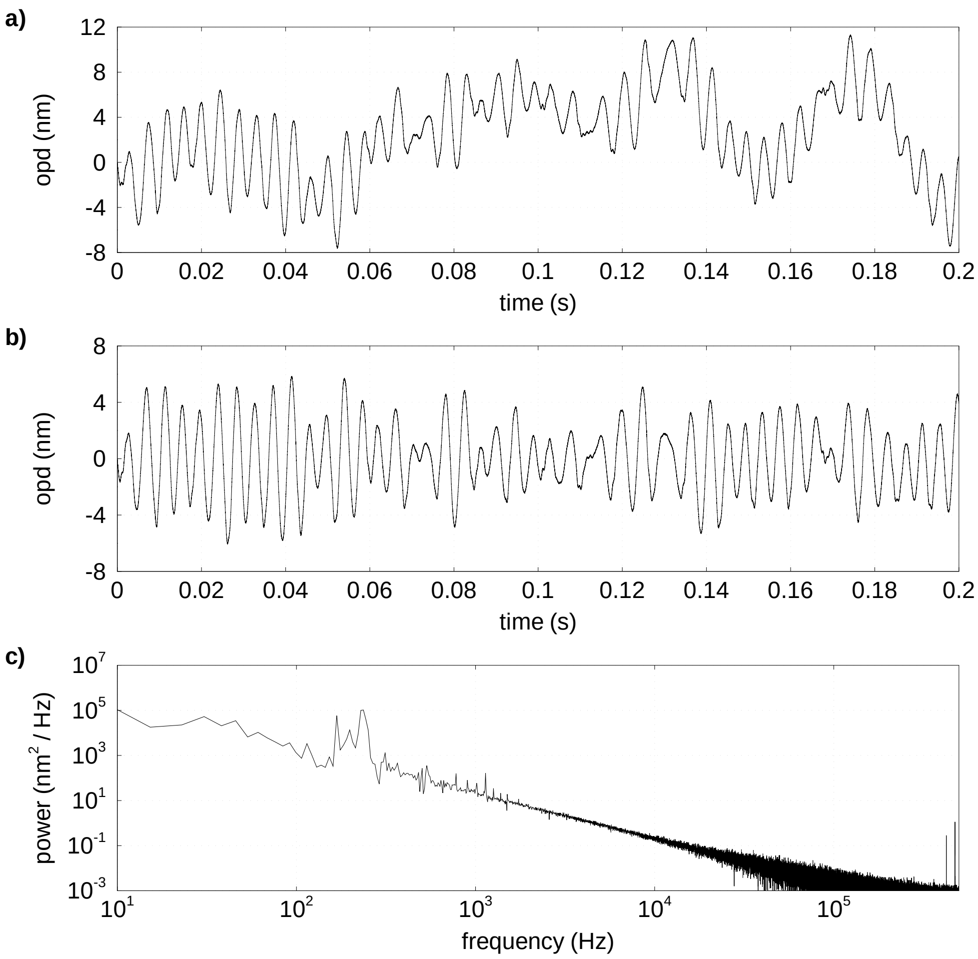

Figure 3.15: LDI noise due to vibrations in the BAM6QT laboratory without vibration control: a) raw noise trace, b) raw signal minus running average, c) noise power spectrum

sampled at 1 MHz, and its power spectrum in the BAM6QT with the optical table floated. Note that the low-frequency oscillations decreased by a factor of two after floating the table. Furthermore, the peak frequency of what is believed to be mostly due to mechanical noise is approximately the same as that for the undamped signal. However, the amplitude of the peak frequency was about 10^4 nm^2/Hz, which is an order of magnitude less than the amplitude recorded without damping. Also note that when the table is floated in the BAM6QT, the amplitude of the low-

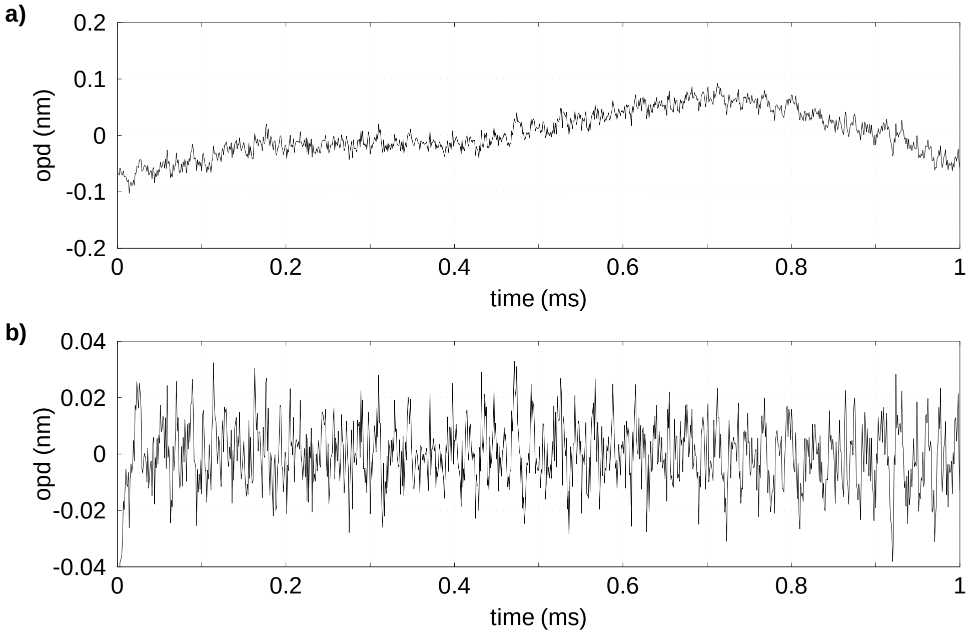

Figure 3.16: LDI electrical noise in the BAM6QT without vibration control: a) raw noise trace, b) raw signal minus running average

frequency peak in the noise spectrum is less than that for the undamped system but remains higher than the peak of the noise spectrum measured in the PQFLT (without vibration control). Figure 3.18b shows a 1 ms calibrated set of filtered data for the high-frequency noise detected by the LDI, sampled at 1 MHz, in the BAM6QT with the table floated. As it would be expected, the peak-to-peak amplitude of the high-frequency noise did not change much by floating the table. Once again, the minimum detectable optical path length difference detectable by this LDI was found to be approximately $\lambda/21,000$ and the RMS value for the noise was 0.39 mV.

The rupture of the diaphragm that establishes supersonic flow inside the tunnel generates a loud noise and the tunnel shakes axially in reaction to the increased momentum of the gas downstream, thus vibrating the floor where the optical table sits. Part of the purpose of installing the vibration control system was to counteract for this strong mechanical shock at the beginning of a run. Note that the air

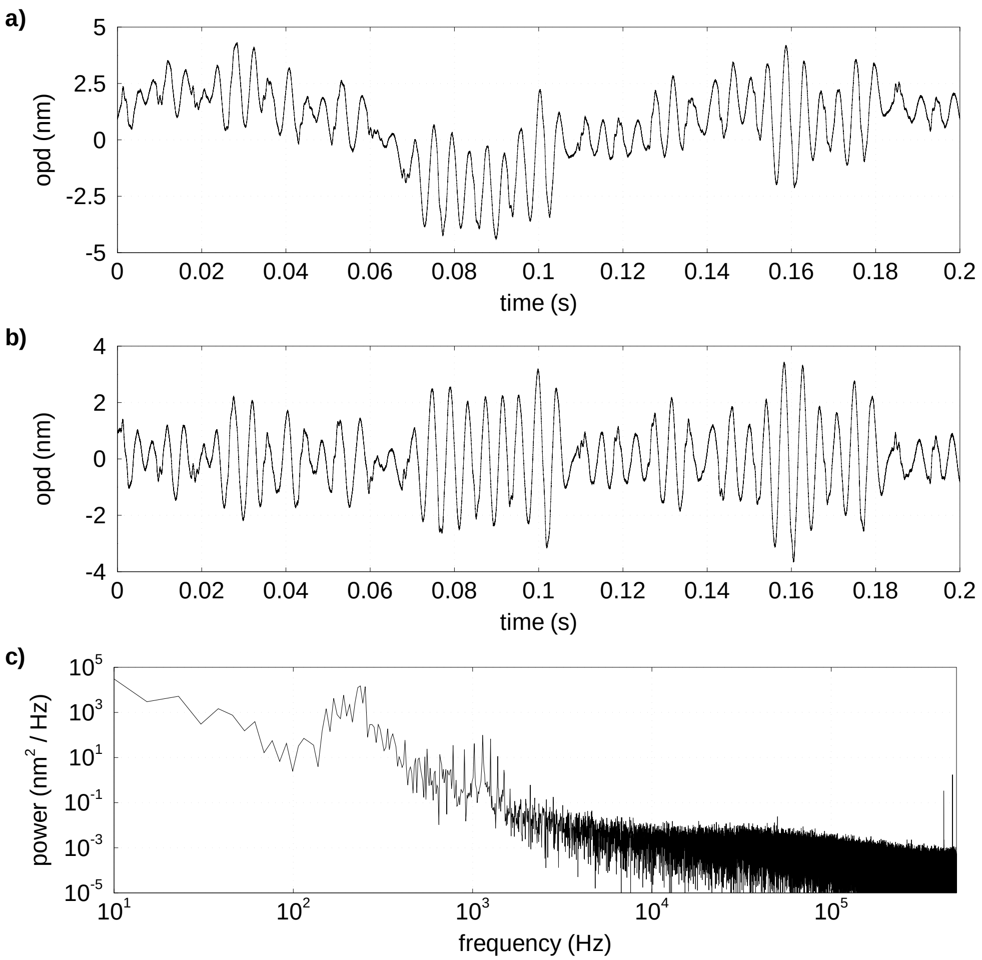

Figure 3.17: Mechanically damped LDI noise due to vibrations in the BAM6QT laboratory: a) raw noise trace, b) raw signal minus running average, c) noise power spectrum

compressor for the wind tunnel was down at the time these experiments were made so an artificial vibration was induced by hitting the floor of the BAM6QT platform with a hammer and recording the LDI output. Figures 3.19(a,b) and 3.20(a,b) show calibrated LDI data, sampled at 1 MHz, along with the signal's power spectrum when the vibration was induced with and without floating the optical table. When the hammer hits the floor of the platform, many objects in the laboratory vibrate at different frequencies thus generating a large amplitude random noise which the

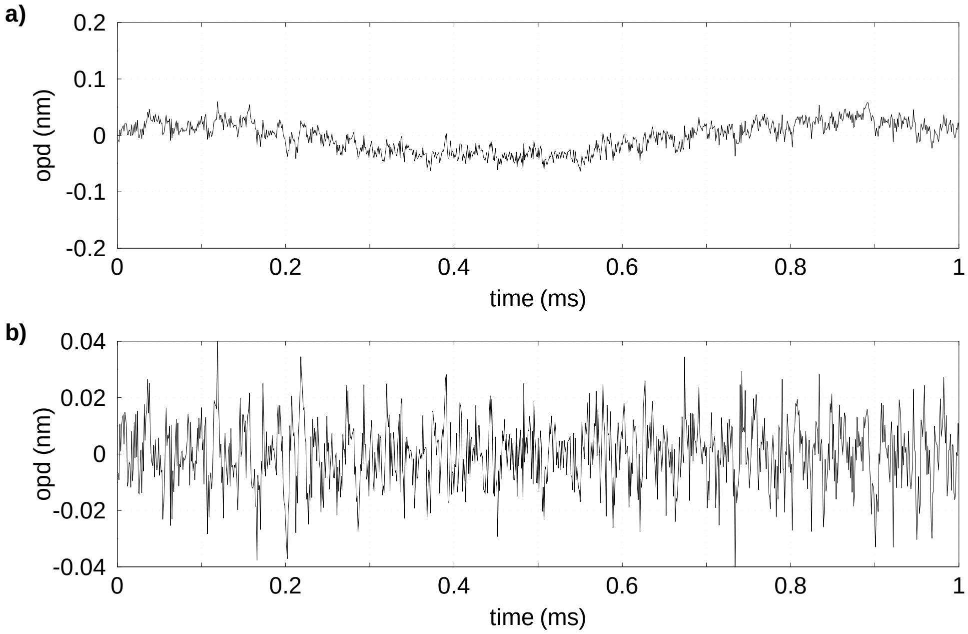

Figure 3.18: Mechanically damped LDI electrical noise in the BAM6QT: a) raw noise trace, b) raw signal minus running average

LDI clearly detects. When the table is floated, the random noise is damped but the original resonant vibration frequency of about 235 Hz can still be seen clearly in the power spectrum of the signal. Although the vibration control system damps external vibrations, it does not isolate the LDI completely and the induced vibration has an effect on the signal.

3.5 Feedback Stabilization System

Strong density gradients in a flow, such as the boundary layer or shock-wave on a model, can introduce a large relative phase shift between the LDI beams passing through opposite sides of the gradient. To compensate for these low-frequency large phase shifts and stabilize the LDI signal to the linear range where its calibration is valid, an autonomous feedback control system was installed. With feedback sta-

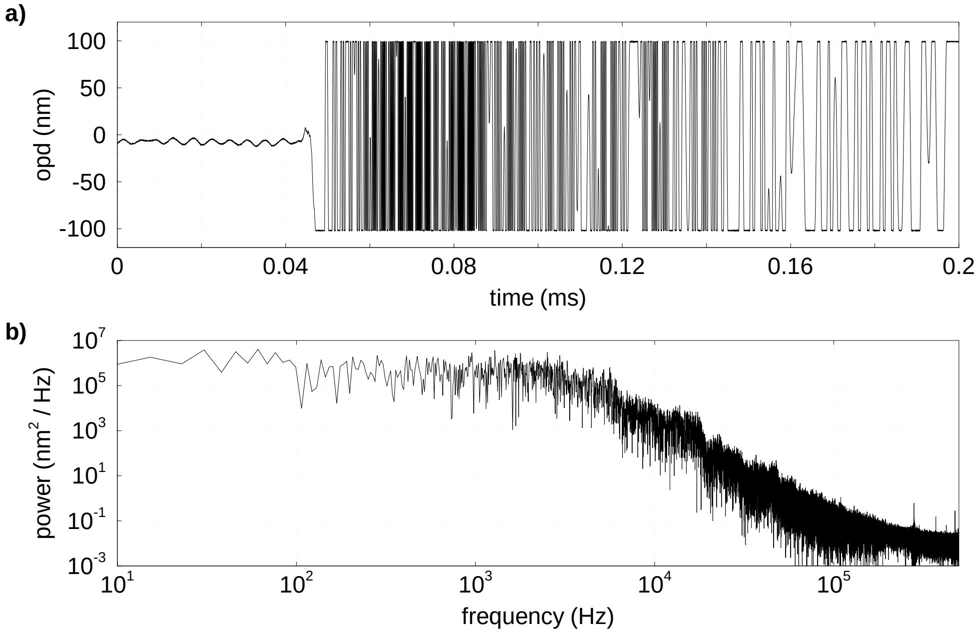

Figure 3.19: Mechanical LDI noise due to vibrations in the laboratory: a) induced vibration profile, b) induced vibration power spectrum

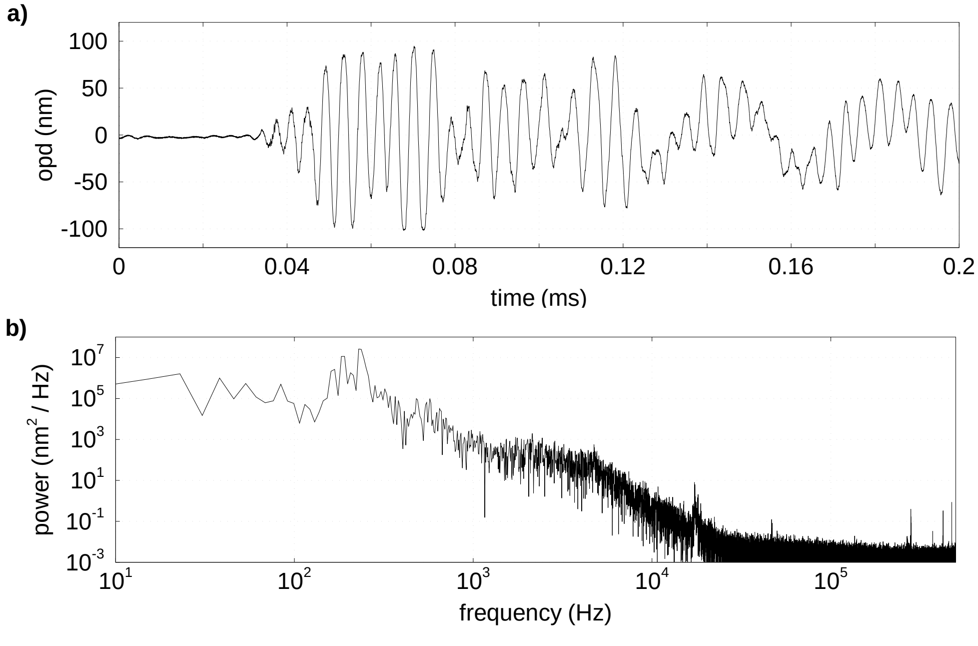

Figure 3.20: Mechanical damped LDI noise due to vibrations in the laboratory: a) induced vibration profile, b) induced vibration power spectrum

bilization, only the bias in the beams is removed while the desired high frequency output signal remains unaffected [10, 17].

A Quantum Technology, Inc. model 28P ADP 2.5mm aperture phase modulator powered by a model HVA-100K high-voltage driver was the active phase compensating device used to stabilize the system. This transverse, low-voltage, electro-optic phase modulator works on the Pockels effect. The Pockels effect is a linear electro-optical effect caused by changes in birefringence of a crystal induced by an electric field (Ref. [43] chapter 8-11). In other words, index of refraction of the crystal in the phase modulator changes in one of its axes when an electric field is applied to it. This system is capable of half-wave phase modulating a 633 nm light beam up to 250 MHz which is well above the frequency response of the low-pass filter and the integrator used to generate the control voltage signal that drives it.

The basic principle and performance of the LDI does not change with the addition of the feedback stabilization system; it is an extra component to keep the LDI centered within the accepted linear range. This is particularly convenient at the beginning of a tunnel run when the shock waves and boundary layers are formed, and more than a full wavelength relative phase shift is introduced. At this point the phase modulator compensates for the large phase shift and returns the LDI signal to the center of the linear region of the interference slope where the optical path length difference is $\delta\Phi = \lambda/4$, for convenience purposes called equilibrium. From this point on, the small density changes in the flow that happen during the run are linearly calibrated (see Equation 3.5).

The phase modulator is inserted in the current LDI setup after the beams in the test section are reunited by the second wollaston prism and are coincident, but before they become spatially coherent at the second quarter-wave plate and can interfere. This way, the beams still have orthogonal linear polarizations and the phase modulator can alter the phase of one of the beams and compensate for the large optical path length difference introduced by the strong density gradients formed in the test section at the beginning of a run. Obviously, the phase modulator must be oriented such that its optical axis is aligned with the polarization of one of the beams, hence when activated, can alter its phase.

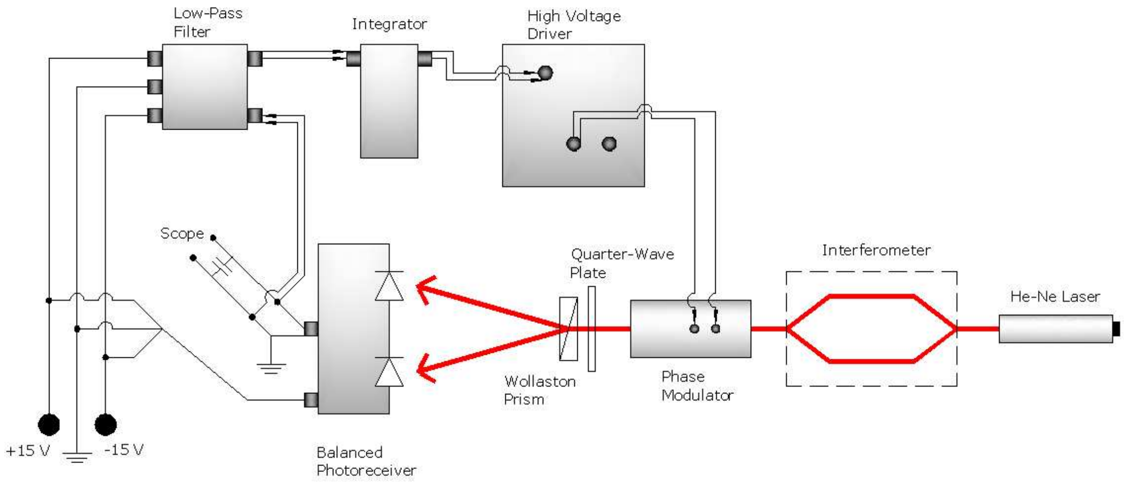

Figure 3.21: Schematic of feedback-stabilized LDI

A schematic of the feedback-stabilized LDI is shown in Figure 3.21. The output signal from the balanced receiver was low-pass filtered at a cutoff frequency of 28 Hz (based on a -0.5 dB criterion) and buffered to an integrator circuit that generates a low amplitude control voltage to be fed back to the high voltage driver. The high voltage driver amplifies the signal into a sufficiently high voltage replica that activates the phase modulator to remove the phase offset. This feedback stabilization control system returns the LDI signal to equilibrium within the limits of the phase modulator. The stability regions of the interference slope are shown in Figure 3.22 where the $C+$ & $C-$ denote the polarities of the integrated control voltage. The control system drives the LDI from the unstable points to the stable ones in the direction of the arrows. Smeets and George developed and described with great detail similar phase compensation control systems for various other purposes [7, 10–12].

The low-pass filter and buffer was adapted from a section of Salyer's active photoreceiver circuit [17]. It uses a Burr-Brown model OPA627AP precision high speed Difet op amp (see Figure 3.23). The amplifier was powered with the same 15 V

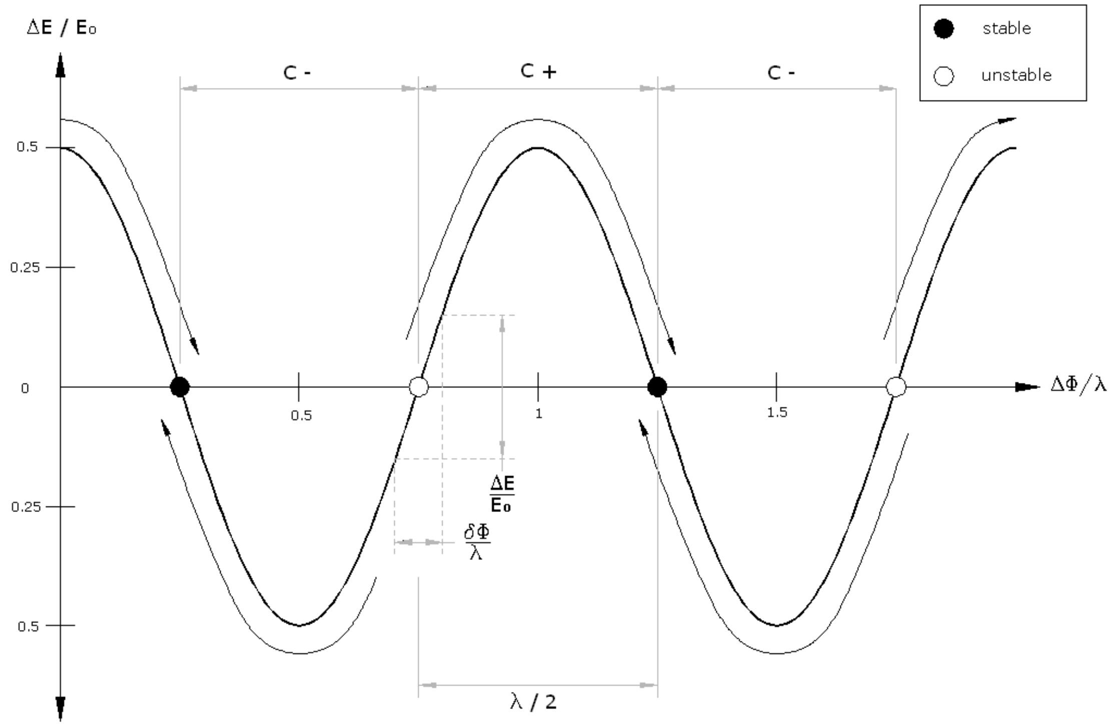

Figure 3.22: Stability regions in LDI interference slope. Drawn based on Ref. [17], Figure 3.17

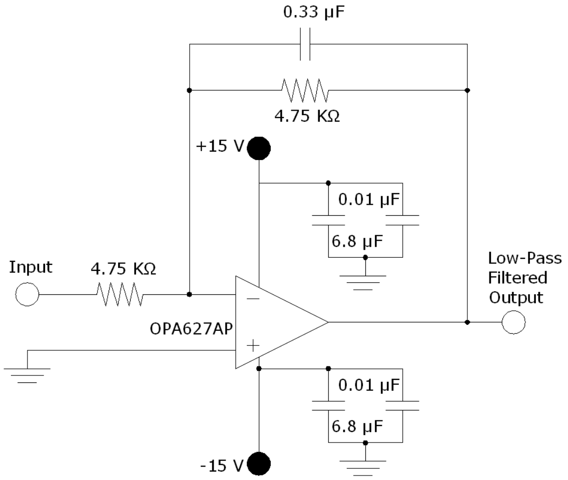

Figure 3.23: Low-pass filter circuit

power supply that powered the photo receiver. The power supply connections were bypassed to ground through two parallel capacitors for noise suppression. This combination of one 6.8 μF tantalum capacitor and one 0.01 μF ceramic capacitor in parallel was also used to keep the impedance of the power supply low throughout the bandwidth of the circuit. A $4.75K\ \Omega$ feedback resistor was used in parallel with a high quality 1.0 μF polycarbonate feedback capacitor to effectively reduce the bandwidth of the amplifier. Unity gain was set using another $4.75K\ \Omega$ intermediary resistor between the output of the photo receiver and the input of the amplifier.

The integrator circuit design shown in Figure 3.24 uses one high quality 0.33 μF polycarbonate capacitor in the feedback path of a Burr-Brown model OPA627AP precision high-speed Difet op amp to integrate the signal. This amplifier is powered with two switch-controlled 9 V batteries and has the same parallel bypass capacitors on the power leads as found in the low-pass filter circuit shown in Figure 3.23. A 500 kΩ variable resistor in conjunction with a 1 kΩ fixed resistor at the negative input of the amplifier serves to alter the time constant of the integrator (in combination with the feedback capacitor of the integrator). A 100 kΩ variable resistor at the amplifier is used to control integration offset voltage, and a switch across the feedback capacitor resets the integration by shorting the capacitor. The voltage output of the circuit is controlled with a combination of a fixed 1 kΩ resistor, a variable 50 kΩ resistor, and a two voltage limiting diodes. The values of the electrical components used in this circuit design were chosen to limit the output to ±0.5 V (1 V peak-to-peak) in order to avoid damaging the high voltage driver as well as to allow for the adjustment of the frequency response between 1 Hz & 50 Hz [17].

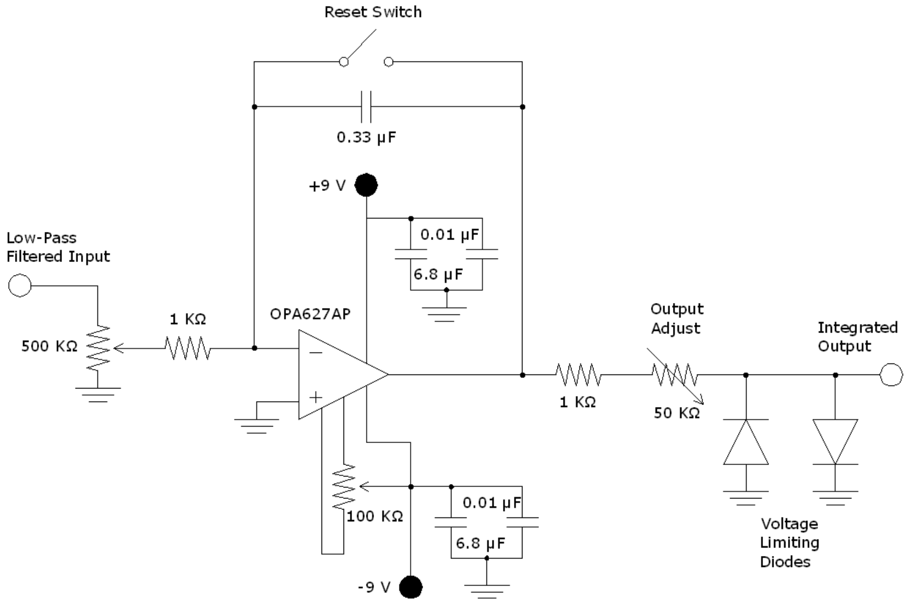

Figure 3.24: Integrator circuit

4. Results

4.1 Hemispherical Nose Studies in PQFLT

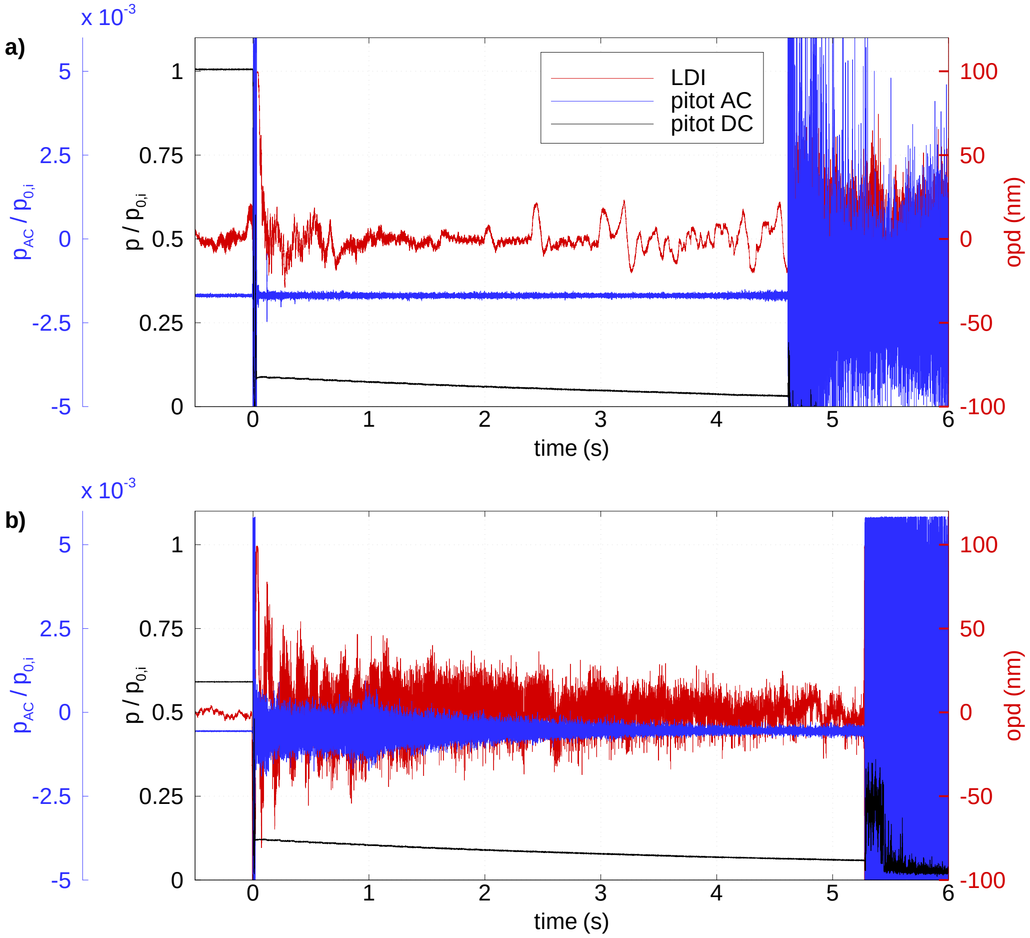

Figure 4.1: Calibrated Kulite and LDI data traces: a) quiet, b) noisy

LDI measurements behind the bow-shock of the hemispherical nose were made and compared to the fluctuations recorded by the Kulite mounted on the tip of the model. Figure 4.1 shows calibrated data sets for the Kulite pressure drop and the

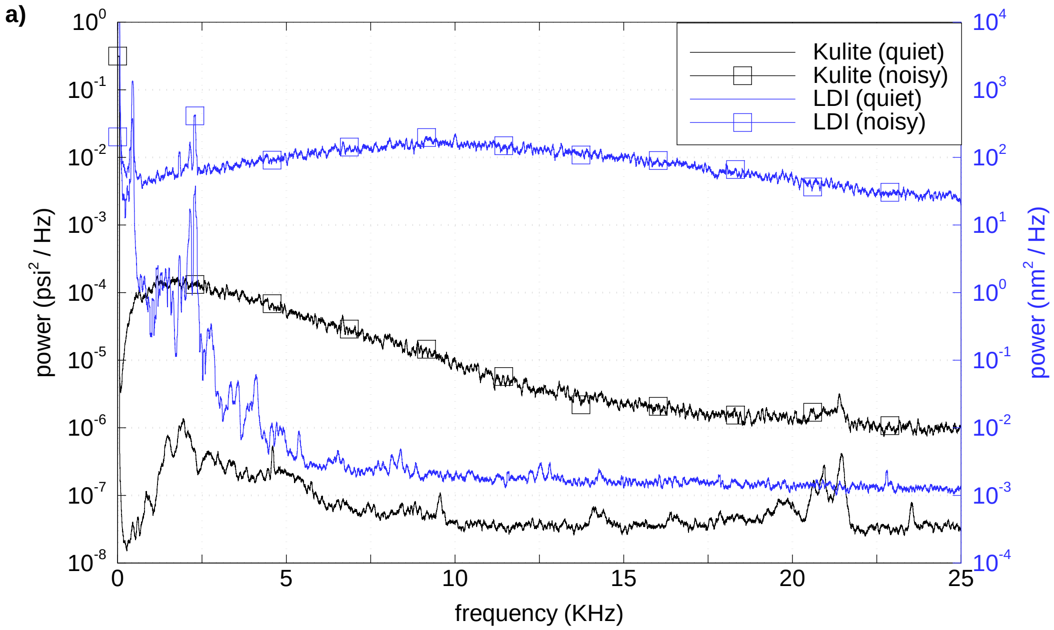

Figure 4.2: Power spectra of hemispherical nose Kulite and LDI data

LDI optical path difference along runs made with $p_{0,i} = 8$ psi and $p_{0,i} = 24$ psi before the nozzle was repolished. The spectrum for the respective data sets are shown in Figure 4.2. It can be observed that the fluctuations recorded by the LDI during the run with $p_{0,i} = 24$ psi have no relation to those recorded by the Kulite. On the other hand, during the run with $p_{0,i} = 8$ psi, they are similar. However, it could be argued that, coincidentally, the LDI might not have detected the same fluctuations that the Kulite failed to detect. Hence, this data is inconclusive at best and further tests had to be made. Also note the two frequency peaks around 435 & 2300 Hz in both LDI traces. The first one is very likely to be caused by mechanical vibrations discussed in Section 3.4. The source of the oscillations causing the second peak remains uncertain. With the current beam spacing of approximately 1.1 mm, the convective speed of the disturbance causing this peak is about 23.5 m/s. This is much slower than the speed of processes that happen inside a turbulent boundary layer. Thus, the possibility that the peak may be due to the fluctuations inside a turbulent window boundary layer is unlikely (see Figure 3.7).

4.2 LDI Sound Wave Detection

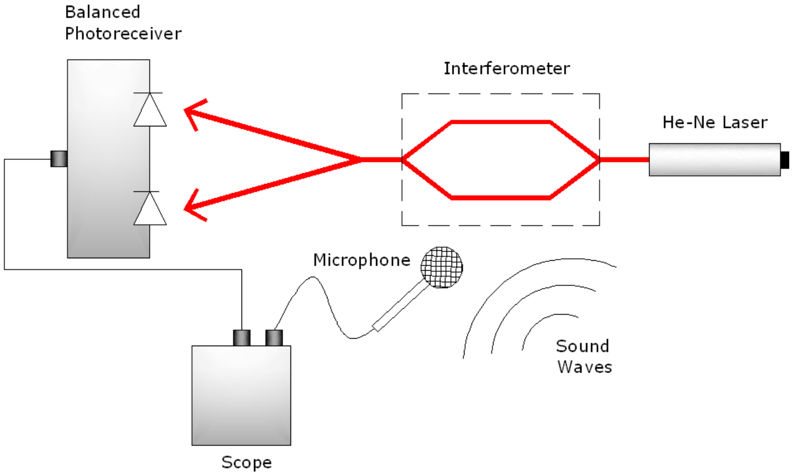

Figure 4.3: Schematic of setup for microphone test with the LDI

Because the LDI is very sensitive to phase shift differences between the parallel beams, it can be used to detect fluctuations caused by sound waves in the path of the beams [7]. In the event that the noise caused by vibrations in the laboratory is too high for the sound waves to be noticed in the signal with the naked eye, a sound with a pronounced primary frequency should generate a peak in the power spectrum of the LDI signal as well as in the power spectrum of a signal recorded by a microphone. While the LDI was connected to one of the oscilloscope's input channels, a microphone was connected to another one as shown in Figure 4.3. A loud sound was made and the signal from both the microphone and the LDI was recorded. Figure 4.4a shows a calibrated data trace from the LDI in the PQFLT and Figure 4.4b shows a trace of the signal detected by the microphone. It can be observed that both signals increase in amplitude when the noise is made but it is not evident they are detecting the same signal. Furthermore, Figure 4.4c shows a plot of

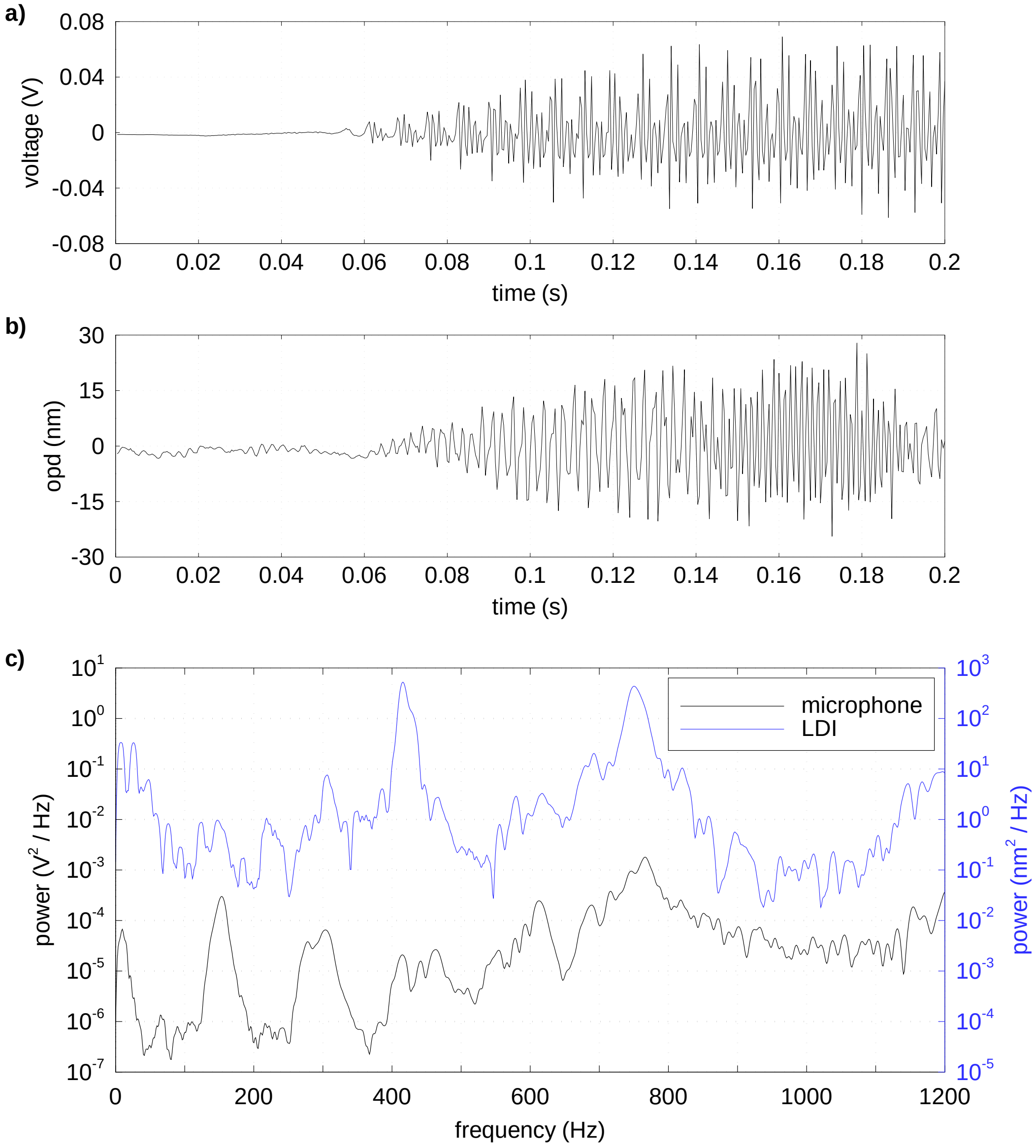

Figure 4.4: a) Sound signal recorded by microphone, b) Calibrated LDI data for sound signal in the PQFLT, c) LDI and microphone data power spectra

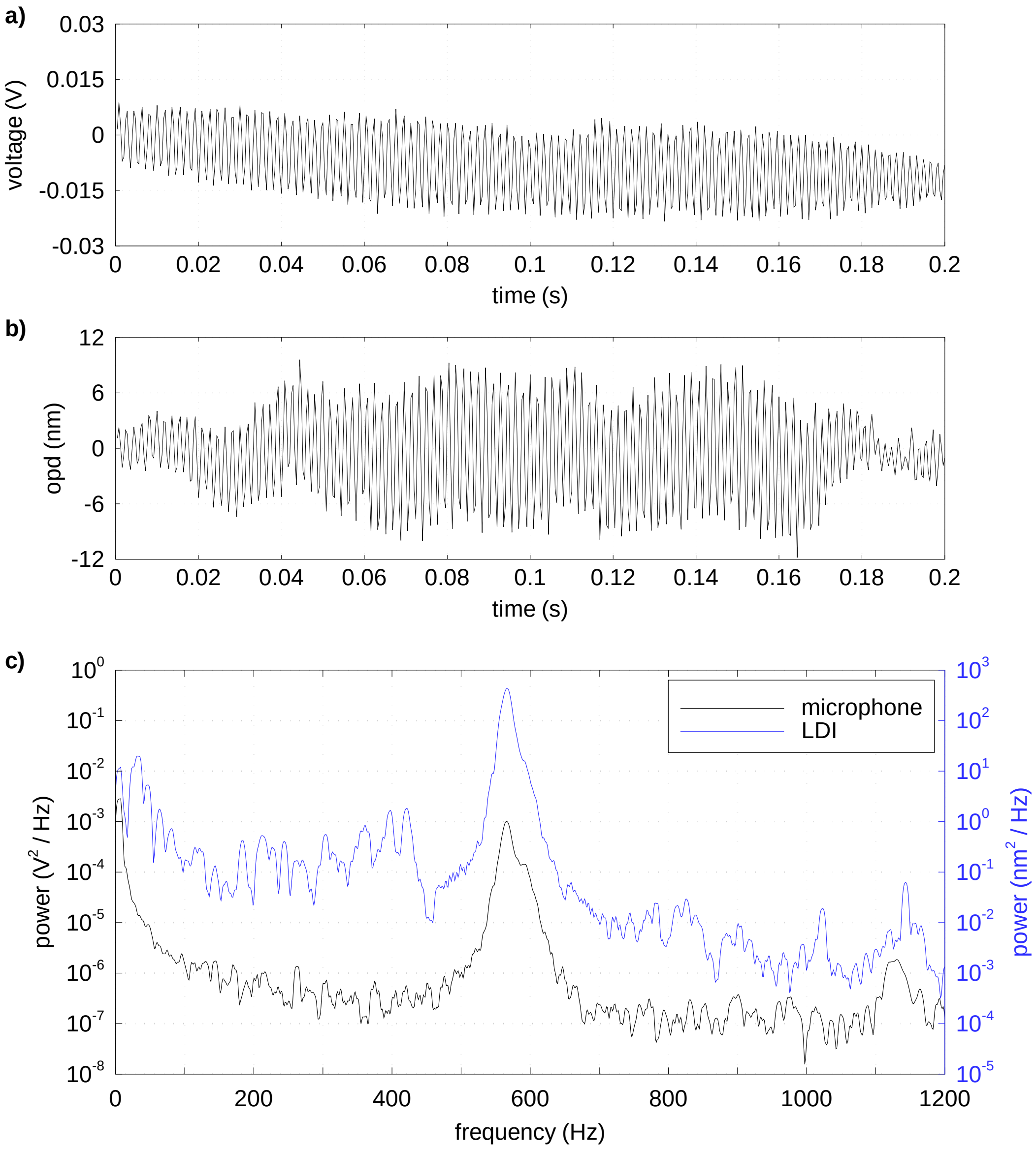

Figure 4.5: a) Whistle signal recorded by microphone, b) Calibrated LDI data for whistle signal in the PQFLT, c) LDI and microphone data power spectra

the power spectrum of both traces which coincide at a dominating frequency of about 750 Hz. Note that the LDI signal has a second high frequency peak around 435 Hz which is believed to be caused by the mechanical vibrations and matches the noise measurements discussed in Section 3.4. A second attempt to measure acoustic noise with the LDI in the PQFLT was made by making a loud whistle. Figures 4.5a, 4.5b and 4.5c show traces and power spectra for the signals recorded by the LDI and the microphone. This noise clearly has a more pronounced primary frequency and it can be observed in the power spectra that the high peaks at about 560 Hz match well.

Experiments were also made in the BAM6QT with and without the vibration control system. Figures 4.6 & 4.7 show LDI and microphone data when a loud sound was made and a recorder note was played in the BAM6QT without floating the table. Moreover, data for similar sounds with the table floated is plotted in Figures 4.8 & 4.9. The frequency of both sounds is clearly detectable and matches the frequencies measured by the microphone.

To obtain further confirmation that the LDI was indeed detecting the sound waves recorded by the microphone, a song was played and the output from the LDI was digitized by a sound recorder as shown in Figure 4.10. The recording was then played back through a pair of speakers and although the sound was not as clean as the original version of the song, the melody was clearly noticeable.

4.3 Forward-Facing Cavity Studies

As a final test of the LDI performance, the signal beam was focused in the subsonic region upstream of the entrance of a forward-facing cavity while the reference beam was focused in the freestream upstream of the bow shock as shown in Figure 3.7. The forward facing-cavity has the characteristic that it generates known ringing frequencies inversely proportional to cavity depth which were measured with a Kulite pressure transducer mounted at the base of the cavity. These fluctuations that exist at the base of the cavity should also exist in the subsonic region ahead of

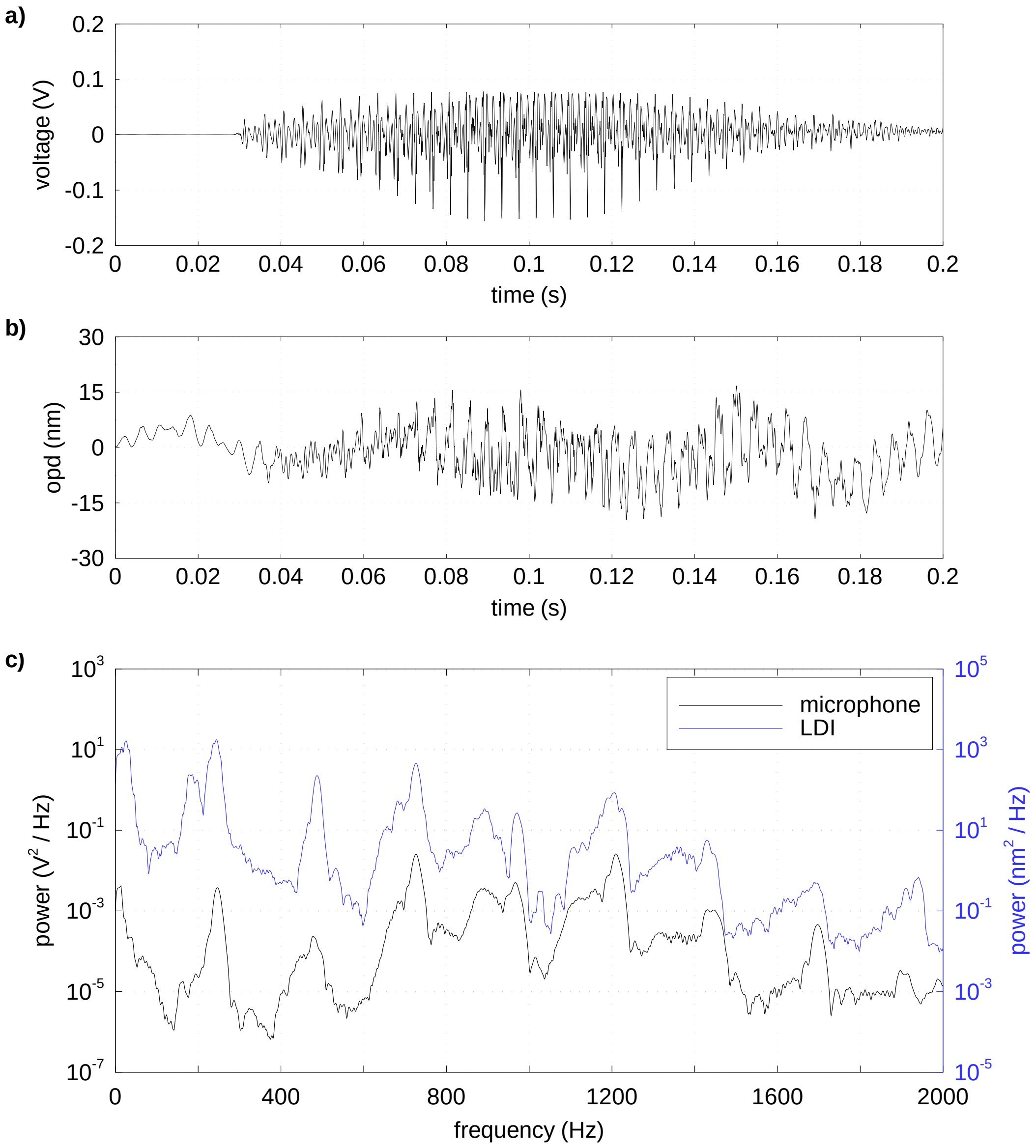

Figure 4.6: a) Sound signal recorded by microphone, b) Calibrated LDI data for sound signal in the BAM6QT, c) LDI and microphone data power spectra

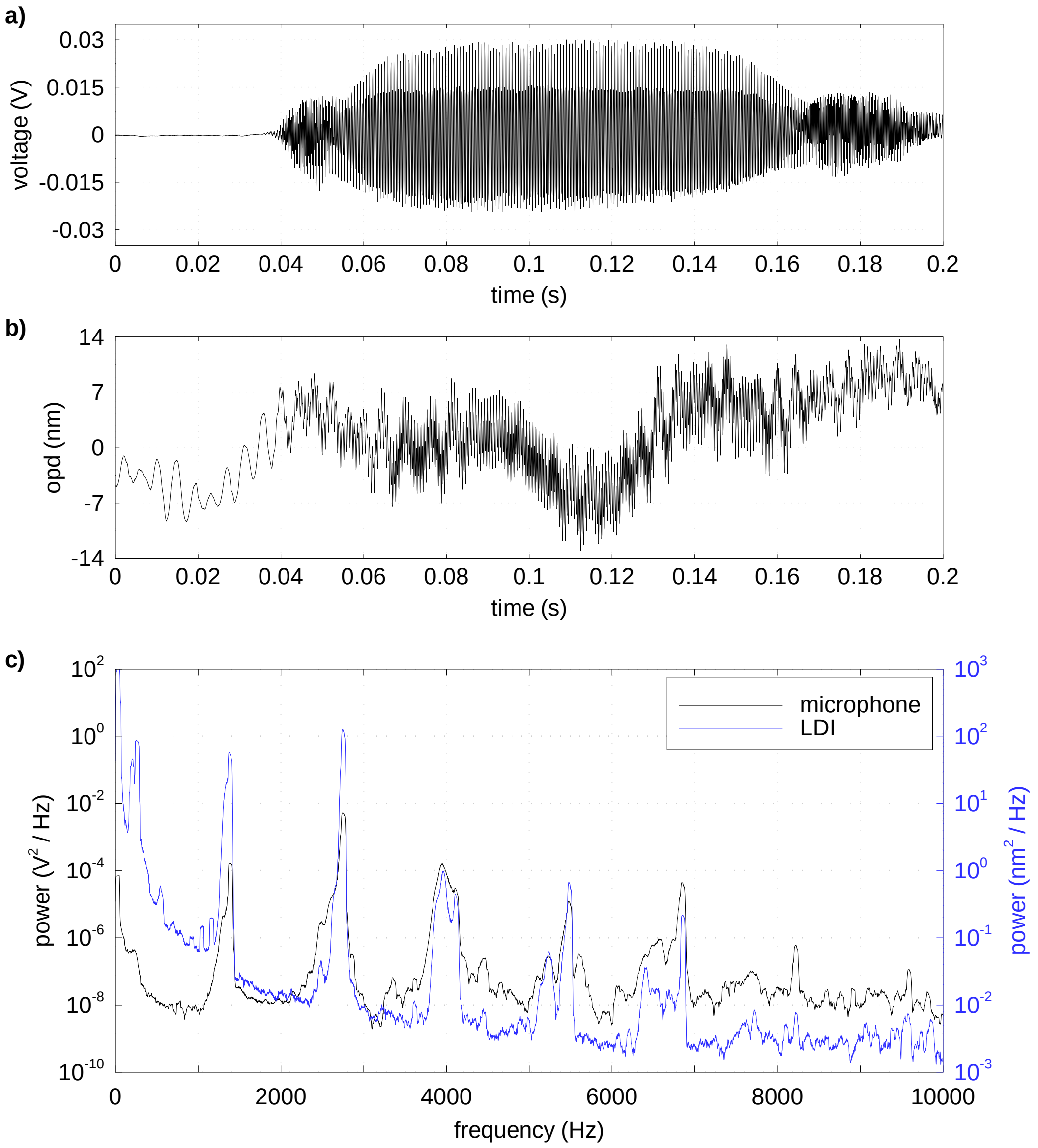

Figure 4.7: a) Recorder note signal recorded by microphone, b) Calibrated LDI data for recorder note signal in the BAM6QT, c) LDI and microphone data power spectra

p]

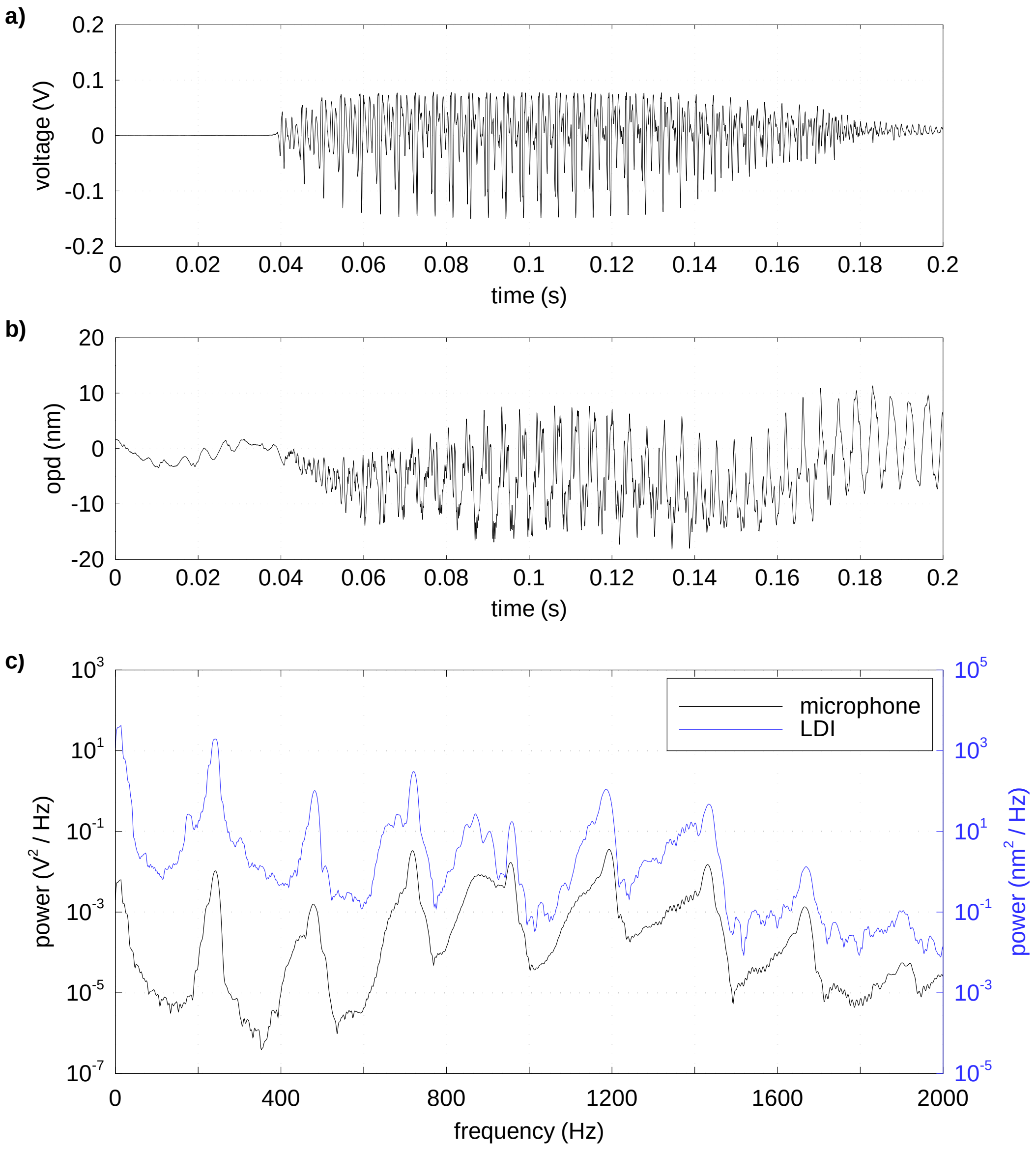

Figure 4.8: a) Sound signal recorded by microphone, b) Mechanically damped, calibrated LDI data for sound signal in the BAM6QT, c) LDI and microphone data power spectra

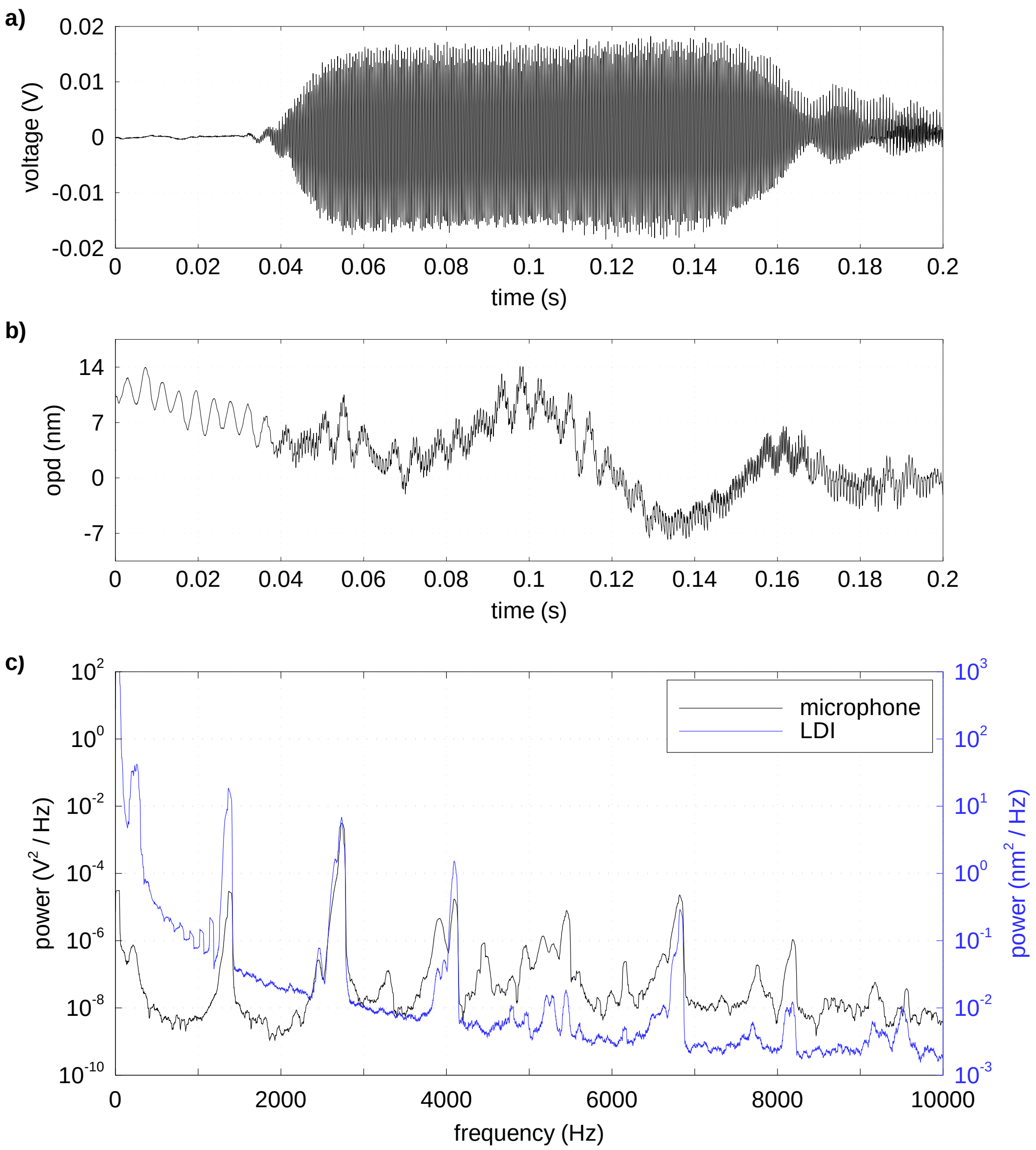

Figure 4.9: a) Recorder note signal recorded by microphone, b) Mechanically damped, Calibrated LDI data for recorder note signal in the BAM6QT, c) LDI and microphone data power spectra

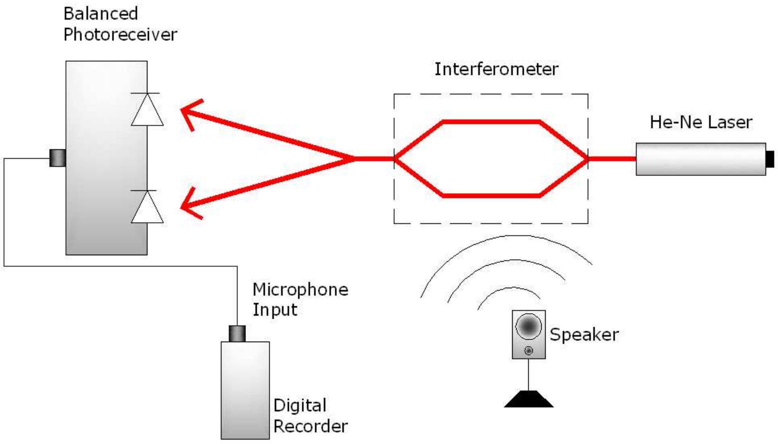

Figure 4.10: Schematic of test for LDI acting as a microphone

its entrance, thus making the LDI able to detect them as well. Furthermore, Ladoon et al. predicted a critical cavity length-to-diameter ratio $L_{crit}/D \approx 2.7$ for which the cavity would self-oscillate even under quiet flow conditions, although there are no experimental results that support this theory because the models previously tested were not deep enough [23]. Note that experiments made to compare the LDI signal to that of the Kulite mounted at the base of the cavity were made before the nozzle was repolished. During that time, the quietness of the flow at low pressures was not reliable and its effect on the cavity oscillations is not addressed in this report. During the time the nozzle was repolished, the LDI was transferred to the BAM6QT. Experiments the nozzle was repolished and quiet flow was confirmed, experiments were made to evaluate the critical depth at which the cavity self-oscillates in quiet flow.

A forward-facing cavity model capable of cavity depth adjustment ranging from $0-3$ D was built and mounted in the test section of the PQFLT. The pressure oscillations' ringing frequencies measured by a Kulite pressure transducer at the base of the cavity were compared to the ringing frequencies detected by the LDI in the subsonic region upstream of the cavity entrance.

Figure 4.11 shows the power spectra of the forward-facing cavity Kulite data at various depths. All of the power spectra displayed in Figure 4.11 are for runs with $p_{0,i} = 24$ psi in the PQFLT before it was repolished. Note that the primary mode frequency peak for the lowest cavity depth (0.6 D) is broader than the peaks for the deeper cavities. Figure 4.12 shows the cavity depth plotted against primary mode resonant frequency and amplitude along with the theoretical 'Organ-Pipe' frequency f as a function of cavity depth given by

$$\omega = 2\pi f = \pi \frac{a}{2L^\star}, \tag{4.1}$$

where

$$L^\star = L + \delta, \tag{4.2}$$

is the distance from the cavity base to the mean shock position [23]. The bow-shock standoff distance value, δ, was obtained from Figure 4.15 in Ref. [45] since it is not known for a forward-facing cavity. An approximation of $\delta/d = 0.24$ was chosen between the value for a 3-dimensional cylinder with a flat nose, and a sphere. Note that the points plotted in Figure 4.12 are only for the primary mode frequency peaks displayed in Figure 4.11 and not for any of the harmonics also displayed in the plot.

A comparison was made between the fluctuations measured by the Kulite and those made by the LDI. Power spectra of both the LDI and the Kulite data are displayed in Figures 4.13 - 4.18 for runs with $p_{0,i} = 8$ psi and $p_{0,i} = 24$ psi at several cavity depths ranging from 0.6 D to 3.0 D before the nozzle was repolished.

For shallow cavity depths ($L/D < 2$), during tunnel runs made with $p_{0,i} = 8$ psi, there is no apparent resonance of freestream disturbances inside the cavity, therefore there is no evident correlation between the fluctuations measured by the LDI and those measured by the Kulite. On the other hand, during runs with higher initial stagnation pressure ($p_{0,i} = 24$ psi), freestream disturbances are amplified by the cavity and the primary ringing frequency of the oscillation is detected by the LDI and also by the Kulite at the base of the cavity. As cavity depth increases, the ringing

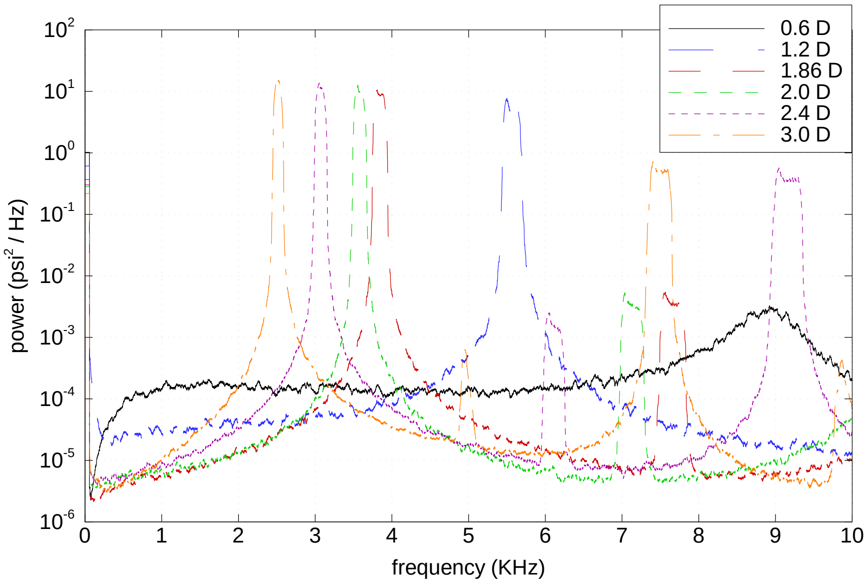

Figure 4.11: Power spectra of forward-facing cavity Kulite data at various depths (before nozzle repolish)

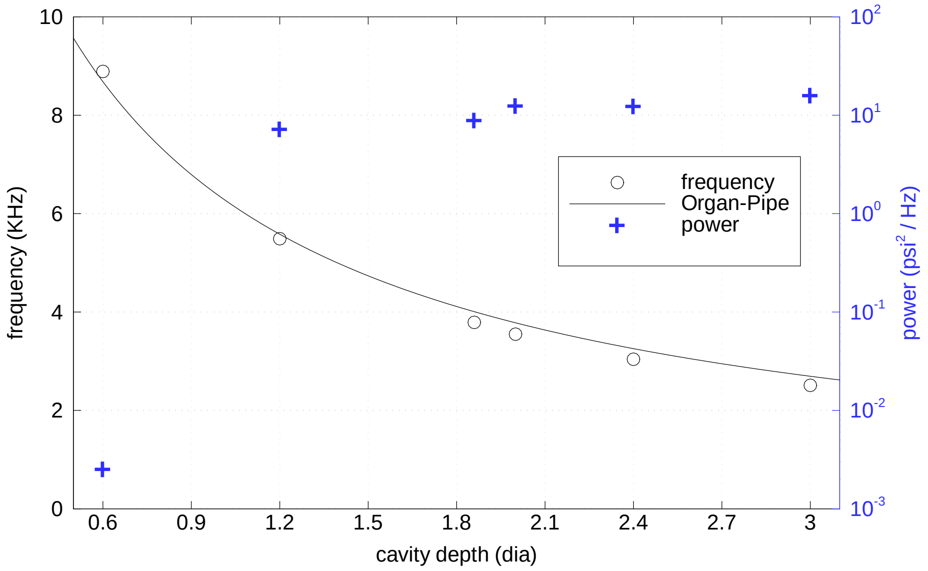

Figure 4.12: a) Forward-facing cavity depth plotted against primary mode resonant frequency (before nozzle repolish), b) Forward-facing cavity depth plotted against amplitude of primary mode resonant frequency (before nozzle repolish)

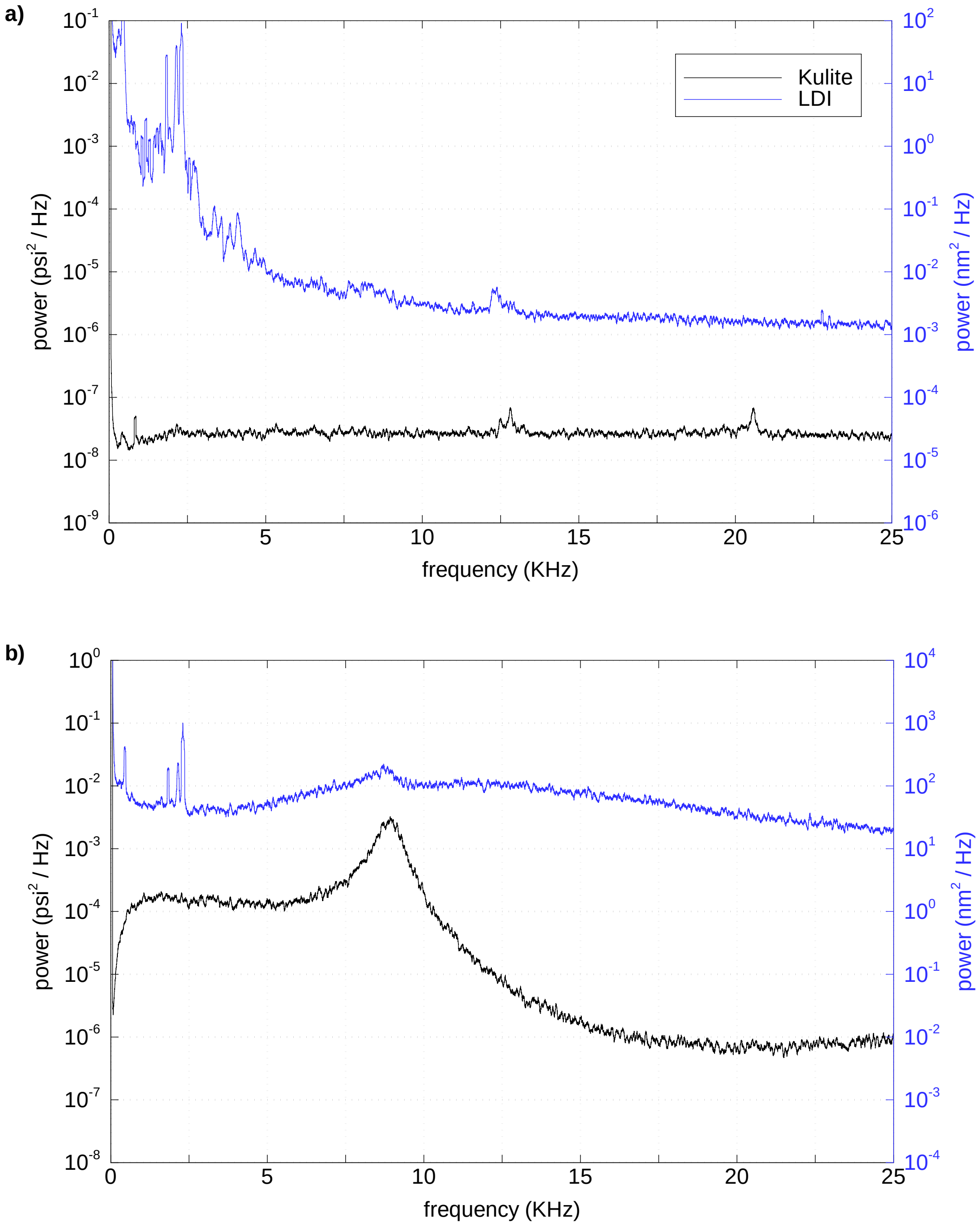

Figure 4.13: Power spectra of forward-facing cavity Kulite and LDI at cavity depth $\frac{L}{D} = 0.6$ D (before nozzle repolish): a) $p_{0,i} = 8$ psi, b) $p_{0,i} = 24$ psi

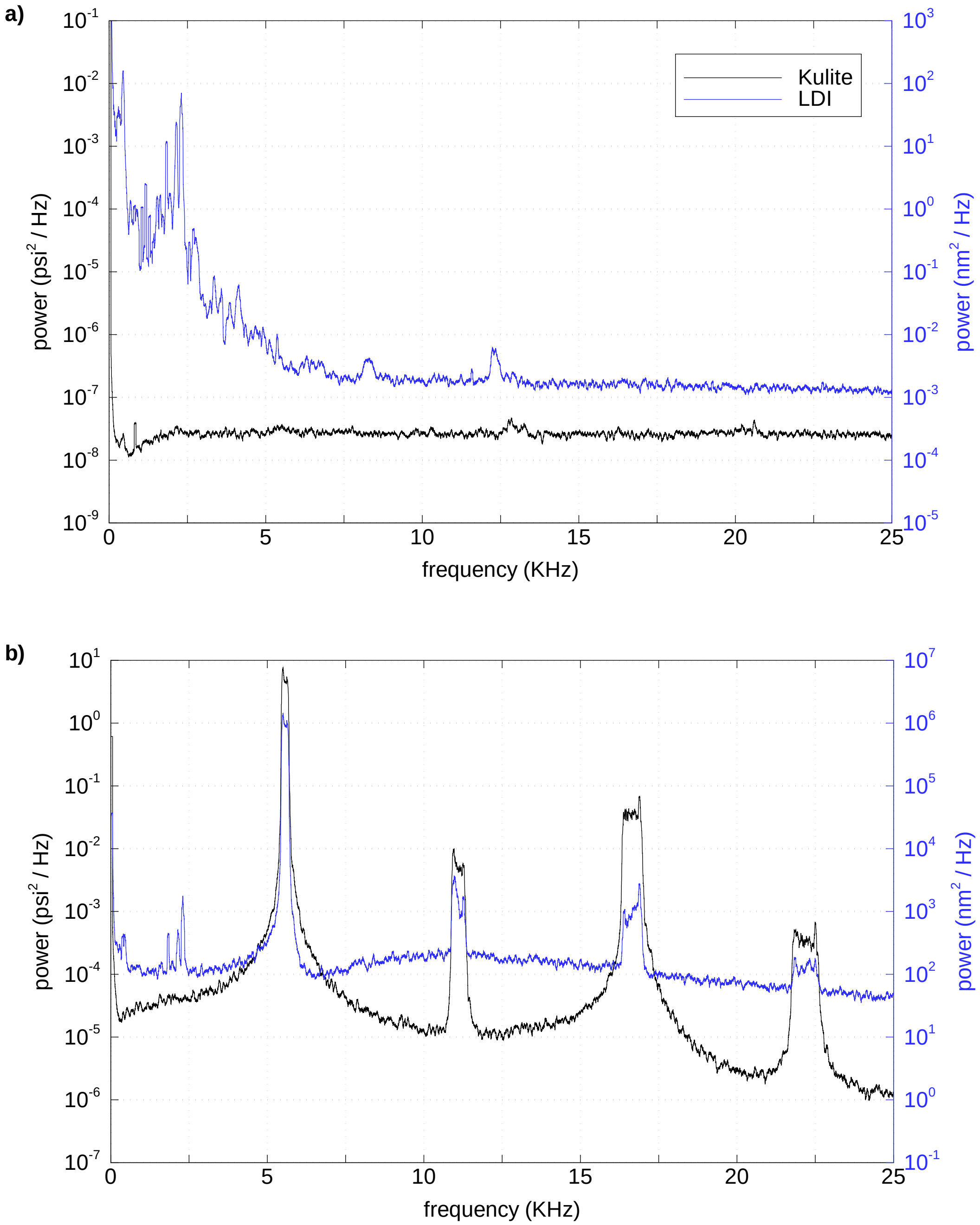

Figure 4.14: Power spectra of forward-facing cavity Kulite and LDI at cavity depth $\frac{L}{D} = 1.2$ D (before nozzle repolish): a) $p_{0,i} = 8$ psi, b) $p_{0,i} = 24$ psi

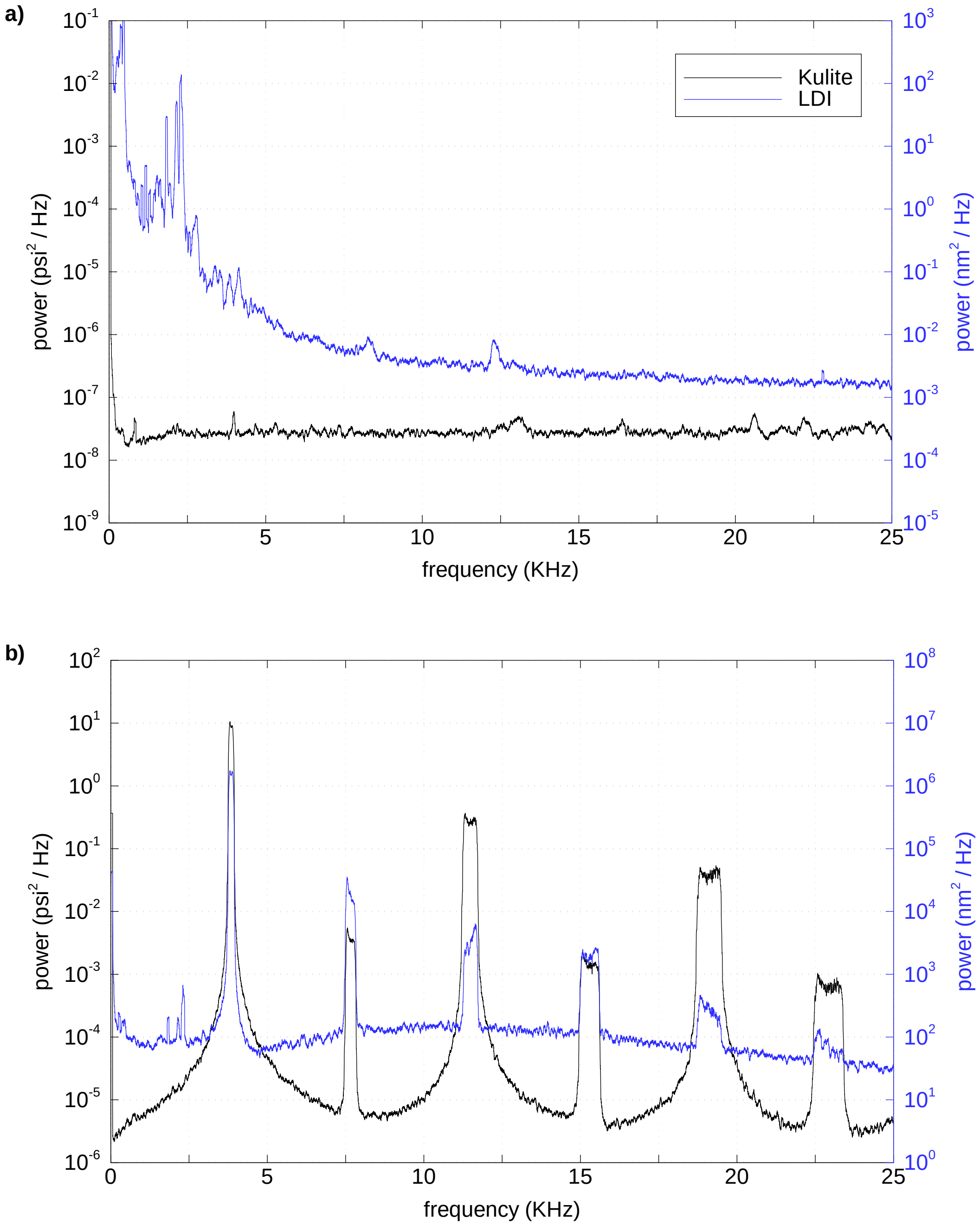

Figure 4.15: Power spectra of forward-facing cavity Kulite and LDI at cavity depth $\frac{L}{D} = 1.86$ D (before nozzle repolish): a) $p_{0,i} = 8$ psi, b) $p_{0,i} = 24$ psi

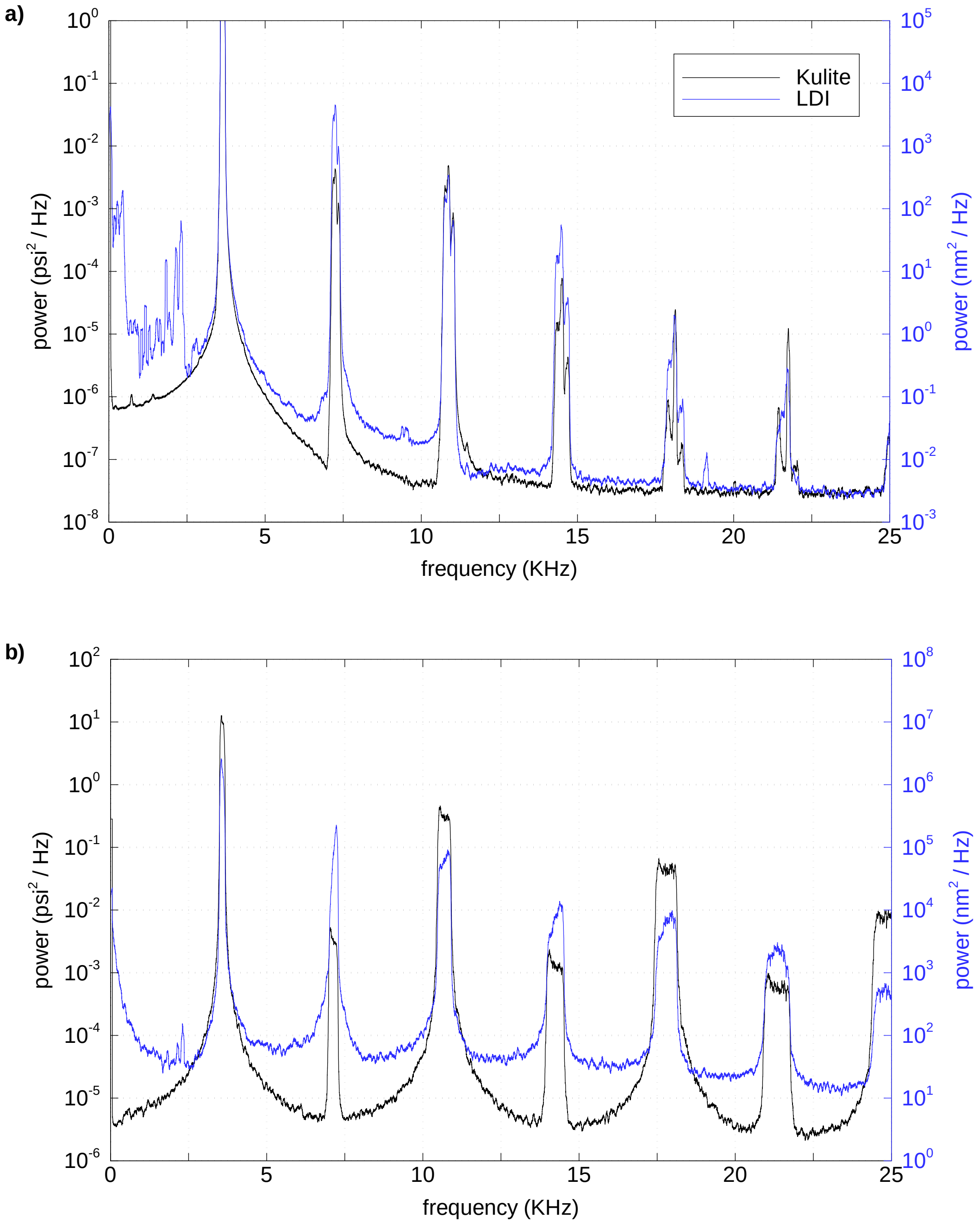

Figure 4.16: Power spectra of forward-facing cavity Kulite and LDI at cavity depth $\frac{L}{D} = 2.0$ D (before nozzle repolish): a) $p_{0,i} = 8$ psi, b) $p_{0,i} = 24$ psi

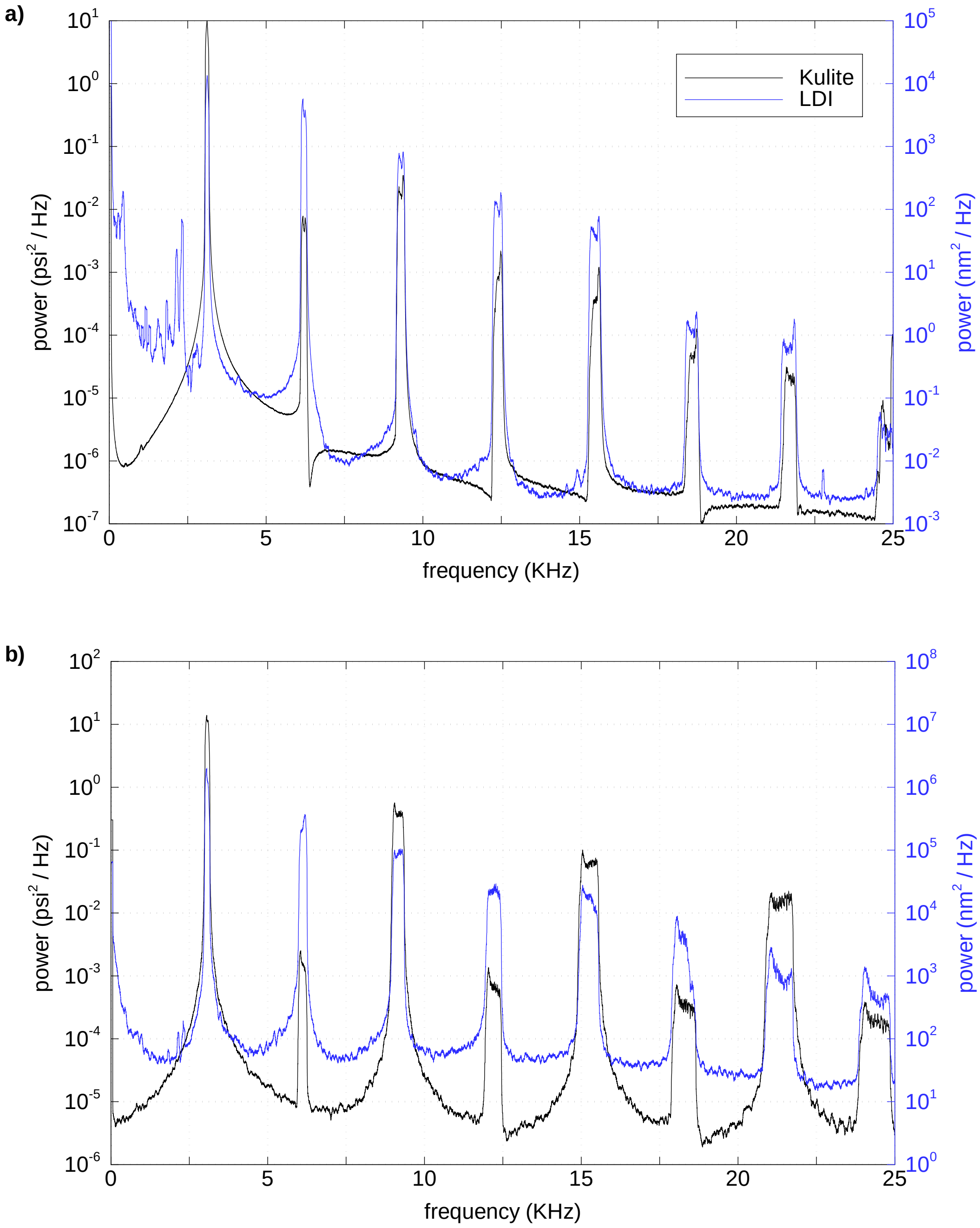

Figure 4.17: Power spectra of forward-facing cavity Kulite and LDI at cavity depth $\frac{L}{D} = 2.4$ D (before nozzle repolish): a) $p_{0,i} = 8$ psi, b) $p_{0,i} = 24$ psi

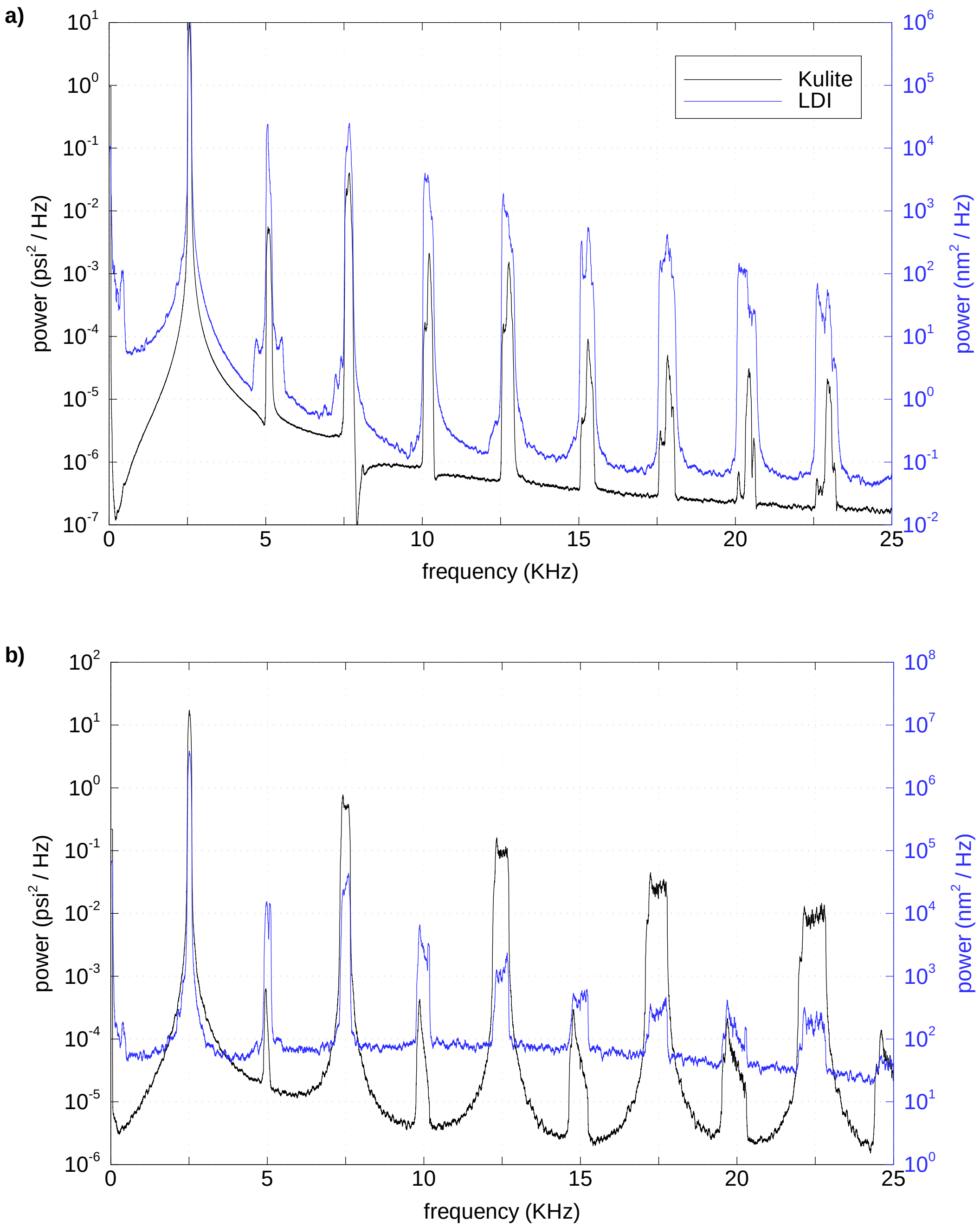

Figure 4.18: Power spectra of forward-facing cavity Kulite and LDI at cavity depth $\frac{L}{D} = 3.0$ D (before nozzle repolish): a) $p_{0,i} = 8$ psi, b) $p_{0,i} = 24$ psi

frequency of the oscillations becomes more pronounced and increases in magnitude. Note that the peaks in the data measured by the LDI match the peaks in the data measured by the Kulite, across the spectrum. Furthermore, it can be observed that for cavity depths greater than $L/D \approx 2.0$ the cavity begins to self-resonate and the flow inside it oscillates at the ringing frequency independent of the initial driver pressure of the run.

After repolishing the PQFLT nozzle, measurements with the forward-facing cavity were made again with reliable quiet flow. Figure 4.19 shows the power spectra of the forward-facing cavity Kulite data at various depths. Figure 4.20 shows the cavity depth plotted against primary mode resonant frequency and amplitude along with the theoretical 'Organ-Pipe' frequency f as a function of cavity depth given by Equation 4.1, with $L^{\star}$ obtained in the same manner as for Figure 4.12. Power spectra of the Kulite data are displayed in Figures 4.22 - 4.25 for quiet ($p_{0,i} = 8$ psi) and noisy ($p_{0,i} = 24$ psi) runs at several low cavity depths ranging from 0.5 D to 1.2 D. Note that at a cavity depth of 0.5 D the cavity resonates in quiet flow. This is a repeatable phenomenon but the cause is unknown. For other depths under 1.2 D the cavity does not display any pronounced resonance under quiet flow (except for0.5 D). However, a small peak can be observed in the spectra of quiet runs at depths of 1.0 D, 1.1 D, and 1.2 D. This indicates that the forward-facing cavity also works as a mechanical amplifier of the freestream disturbances present in quiet flow. On the other hand, for depths of 1.3 D and above, the cavity self-resonates even in quiet-flow and a clear ringing frequency for several cavity depths ranging from 1.3 D to 3.0 D can be observed in Figure 4.26 during runs with $p_{0,i} = 8$ psi. The amplitudes of the primary resonant frequencies of runs made under noisy conditions at depths of 1.3 D, 1.5 D, and 1.8 D are plotted in Figure 4.20. It can be observed that the amplitude of the primary resonant frequency does not vary much with freestream noise when the cavity is deeper than 1.2 D.

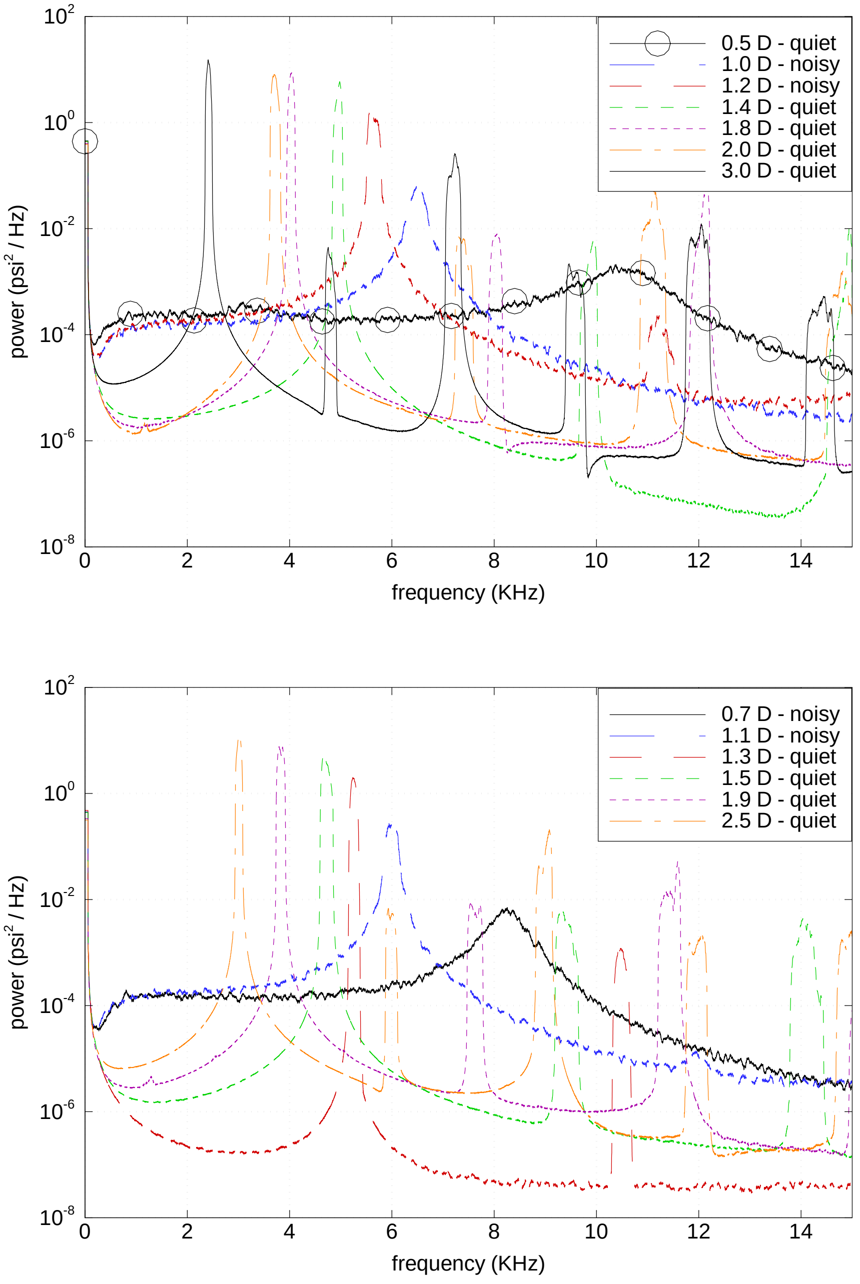

Figure 4.19: Power spectra of forward-facing cavity Kulite data at various depths after repolishing PQFLT nozzle

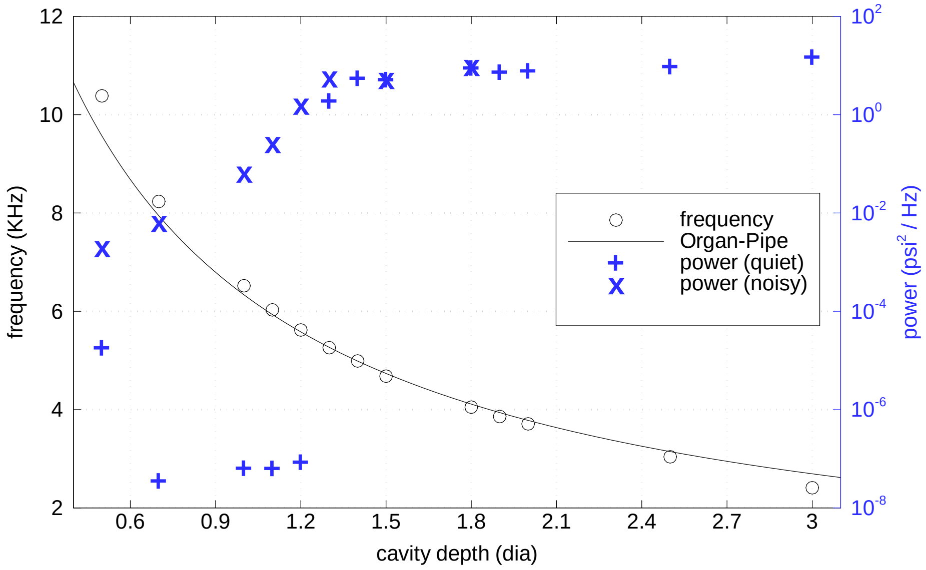

Figure 4.20: a) Forward-facing cavity depth plotted against primary mode resonant frequency after repolishing PQFLT nozzle, b) Forward-facing cavity depth plotted against primary mode resonant frequency's amplitude after repolishing PQFLT nozzle

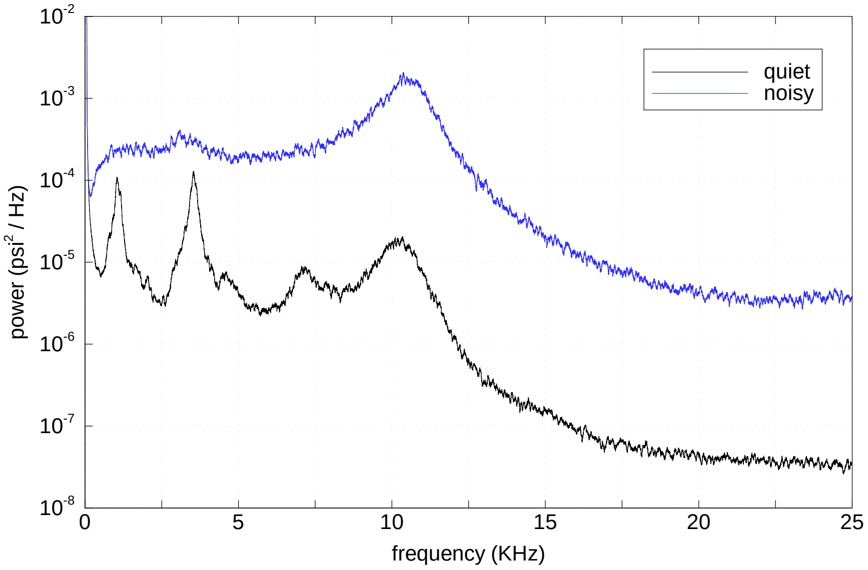

Figure 4.21: Power spectra of forward-facing cavity Kulite and LDI at cavity depth $\frac{L}{D} = 0.5$ D: a) quiet, b) noisy

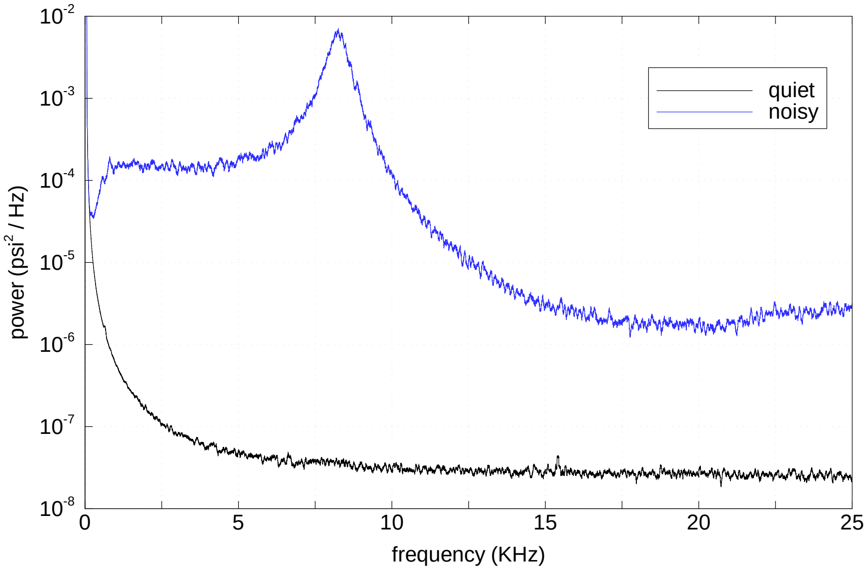

Figure 4.22: Power spectra of forward-facing cavity Kulite and LDI at cavity depth $\frac{L}{D} = 0.7$ D: a) quiet, b) noisy

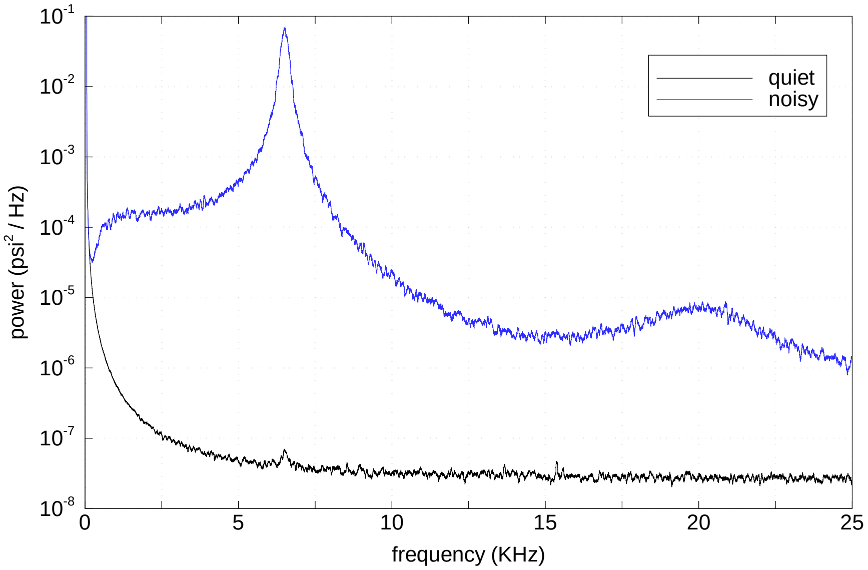

Figure 4.23: Power spectra of forward-facing cavity Kulite and LDI at cavity depth $\frac{L}{D} = 1.0$ D: a) quiet, b) noisy

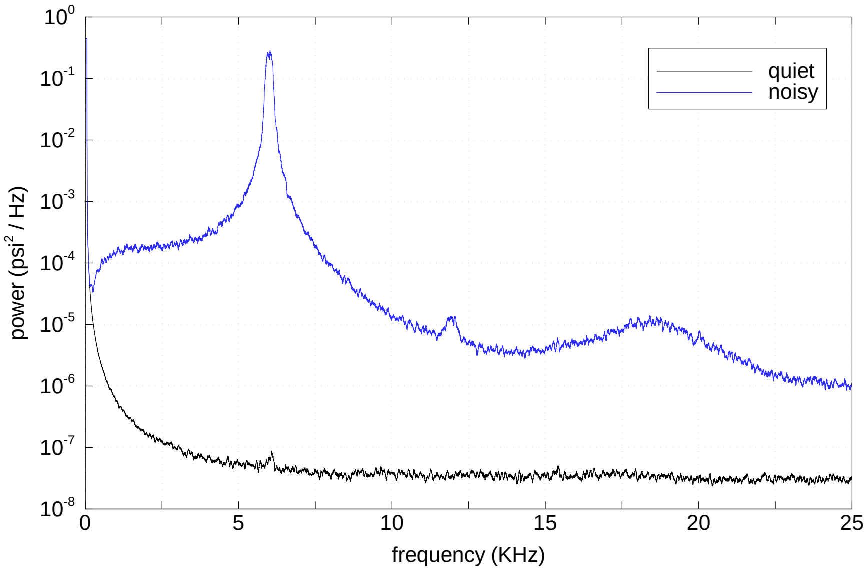

Figure 4.24: Power spectra of forward-facing cavity Kulite and LDI at cavity depth $\frac{L}{D} = 1.1$ D: a) quiet, b) noisy

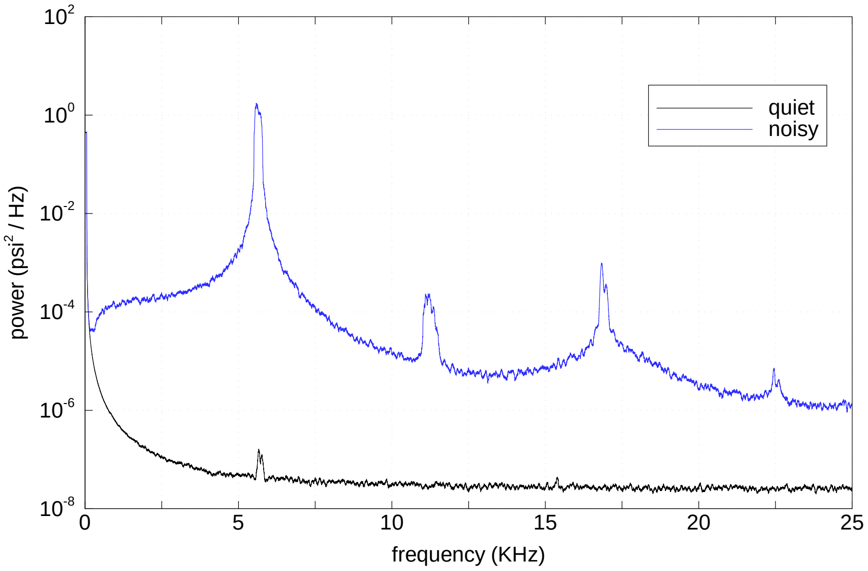

Figure 4.25: Power spectra of forward-facing cavity Kulite and LDI at cavity depth $\frac{L}{D} = 1.2$ D: a) quiet, b) noisy

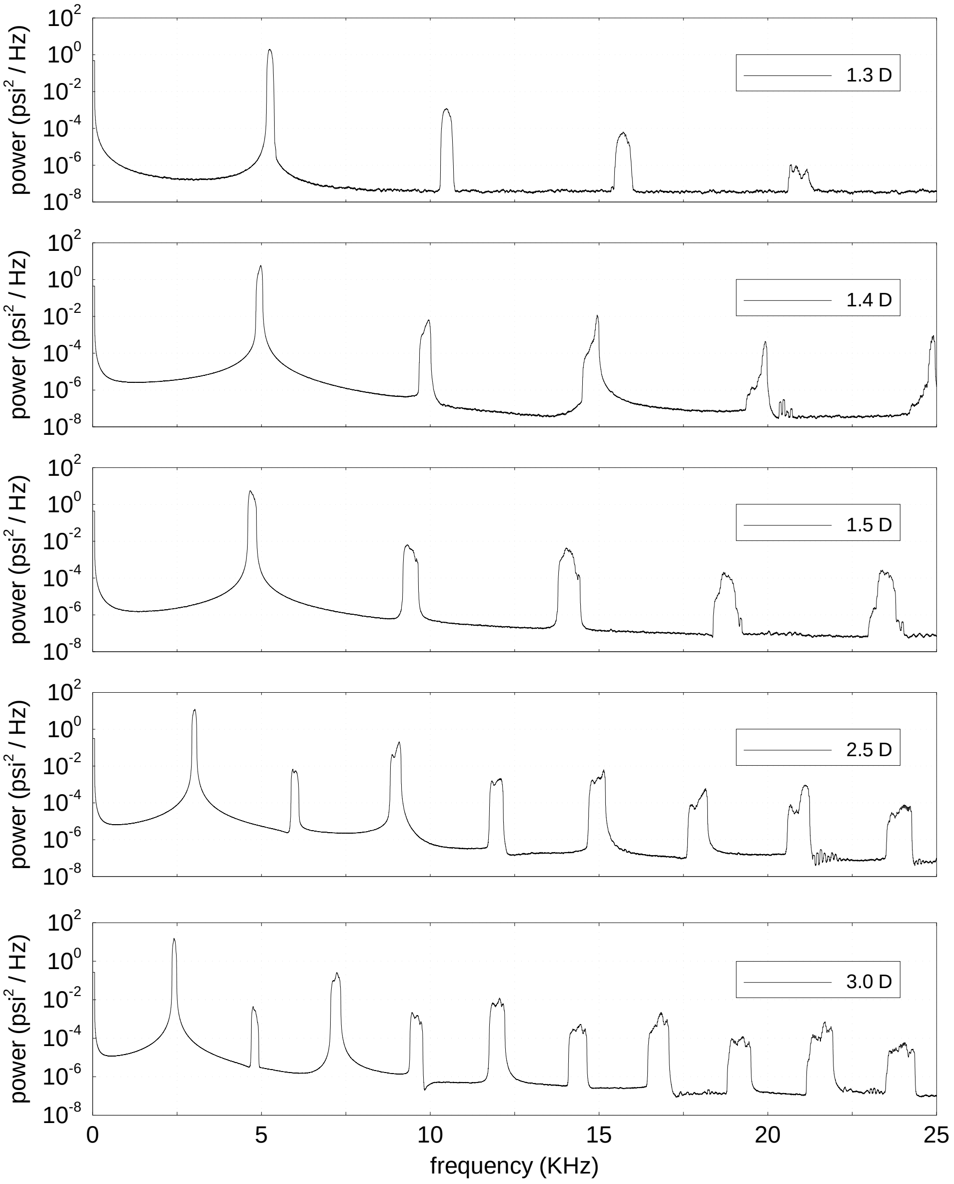

Figure 4.26: Power spectra of self-oscillating forward-facing cavity Kulite data at various depths after repolishing PQFLT nozzle (quiet flow)

5. Conclusions

The LDI was successfuly reassembled and tested in the PQFLT. The system built previously by Salyer [17] was upgraded using a commercially designed balanced photoreceiver. The system is now able to resolve optical path length differences as small as $\frac{\lambda}{21{,}000}$ and has an operational bandwidth from DC to 80 MHz.

In addition, the LDI was redesigned and installed in the BAM6QT experimental facility. Further improvements were made to allow for larger beam spacing in the test section and to isolate the LDI from vibrations. This was done primarily to enable measurements of second-mode instabilities in the BAM6QT. The LDI has several advantages over other diagnostic methods. Its high sensitivity, good axial spatial resolution, and large bandwidth make it an important complement to hot wires, hot films and flush-mounted pressure transducers. The main drawback of the LDI is the extended integration over the beam path. The feedback stabilization system included in this LDI stabilizes the system at equilibrium, compensating for strong density gradients introduced in the flow. This allowed for quantitative measurements in the subsonic region behind the bow shock of a hemispherical nose and a forward-facing cavity.

Flow fluctuations inside an adjustable forward-facing cavity were made using Kulite pressure transducers and the LDI. Predictions made by Ladoon et al. [23] of a self-resonating forward facing cavity were confirmed, although the critical length-to-diameter ratio predicted is considerably higher than the one observed. Furthermore, small primary mode frequency peaks were detected by the Kulite even under quiet flow at low cavities. The LDI and the Kulite detected primary mode frequencies inside the cavity. These were compared with the theoretical 'Organ-Pipe' frequencies. The fit between experimental data and theory is somewhat ambiguous, due to the uncertainty of the bow-shock standoff distance for an oscillating forward-facing cavity. Schlieren studies should be made with the forward-facing cavity to measure the shock standoff distance for the cavity depths used in this experiment.

Though this work is a substantial advance towards the operation of the LDI in the BAM6QT, further experimentation is still required for the system to perform correctly. Portal windows have yet to be installed on both sides of the test section to enable the LDI beams to pass through. Alignment adjustments to compensate for the curvature of the windows will also be necessary. The author recommends that the forward-facing cavity be used to test the instrument once the windows are installed. It may also be desirable to raise the cutoff frequency of the feedback stabilization low-pass filter to remove the low frequency noise present in the LDI signal.

LIST OF REFERENCES

LIST OF REFERENCES

[1] S. P. Schneider. Hypersonic laminar-turbulent transition on circular cones and scramjet forebodies. *Progress in Aerospace Sciences*, 40:1–50, 2004.

[2] T. C. Lin. The influence of laminar boundary layer transition on entry vehicle design and its performance. AIAA Paper 2007-309, January 2007.

[3] C. H. Campbell, B. Anderson, G. Bourland, S. Bouslog, A. Cassady, T. J. Horvath, S. A. Berry, P. A. Gnoffo, W. A. Wood, J. J. Reuther, D. M. Driver, D. C. Chao, J. Hyatt, and D. Picetti. Orbiter return to flight entry aeroheating. AIAA Paper 2006-2917, June 2006.

[4] F. T. Hung, S. N. Greenschlag, and C. A. Scottoline. Shock-wave-boundary-layer interaction effects on aerodynamic heating. *Journal of Spacecraft and Rockets*, 14(1):25–31, January 1977.

[5] L. E. Ericsson. Transition effects on slender vehicle stability and trim characteristics. AIAA Paper 2006-2917, January 1973.

[6] G. Smeets and A. George. Gas-dynamic investigations in a shock tube using a highly sensitive interferometer. French-German Research Institute (ISL) Technical Report R 14/71. Translated by Andreas R. Goetz, June 1971. DTIC ADA307743.

[7] G. Smeets and A. George. Laser-differential interferometer applications in gas dynamics. French-German Research Institute (ISL) Technical Report R 28/73. Translated by Andreas R. Goetz, November 1973. DTIC ADA307459.

[8] G. Smeets and A. George. Investigation of shock boundary layers with a laser interferometer. *Stanford University Press, Stanford, California. Recent Development in Shock Tube Research*, pages 429–438, 1973. D. Bershader and W. Griffith, editors.

[9] G. Smeets. Density profiles of a subsonic free jet (d=80 mm), measured using the laser-differential interferometer. French-German Research Institute (ISL) Technical Note N 620/75. Translated by Andreas R. Goetz, November 1975. DTIC ADA307509.

[10] G. Smeets and A. George. Laser-interferometer with phase compensation. French-German Research Institute (ISL) Technical Report R 28/73. Translated by Andreas R. Goetz, December 1975. DTIC ADA307458.

[11] G. Smeets. Flow diagnostics by laser interferometry. *IEEE Transactions on Aerospace and Electronic Systems*, 13(2):82–90, March 1977.

[12] G. Smeets. Interferometry. French-German Research Institute (ISL) Technical Report CO 214/90, May-June 1990.

[13] G. Smeets. Interferometry in rarefied gas flows. French-German Research Institute (ISL) Technical Report CO 207/92, April 1992.

[14] S. H. Collicott, S. P. Schneider, and N. L. Messersmith. Review of optical diagnostic methods for hypersonic low-noise faclities. AIAA Paper 1996-0851, January 1996.

[15] T. R. Salyer, Laura A. Randall, S. H. Collicott, and S. P. Schneider. Use of laser differential interferometry to study receptivity on a hemispherical nose at Mach 4. AIAA Paper 1998-0238, 1998.

[16] T. R. Salyer, S. H. Collicott, and S. P. Schneider. Feedback stabilized laser differential interferometry for supersonic blunt body receptivity experiments. AIAA Paper 2000-0416, January 2000.

[17] T.R. Salyer. *Laser Differential Interferometry for Supersonic Blunt Body Receptivity Experiments.* PhD thesis, Purdue University School of Aeronautics & Astronautics, May 2002.

[18] T. R. Salyer, S. H. Collicott, and S. P. Schneider. Characterizing laser-generated hot spots for receptivity experiments. *AIAA Journal*, 44(12):2871–2878, December 2006.

[19] M. Azzazy, D. Modarress, and J. Trolinger. Feasibility study of optical boundary layer transition detection. Contractor Report NASA-CP-178109, June 1986.

[20] J. E. O'Hare. A nonperturbing boundary-layer transition detector. Arnold Engineering Development Center Technical Report AEDC-TR-85-62, November 1985.

[21] J. D. Schmisseur. *Receptivity of the Boundary Layer on a Mach-4 Elliptic Cone to Laser-Generated Localized Freestream Perturbations.* PhD thesis, Purdue University School of Aeronautics & Astronautics, December 1997.

[22] D.W. Ladoon, J. D. Schmisseur, and S. P. Schneider. Laser-induced resonance in a forward-facing cavity at Mach 4. AIAA Paper 97-0339, January 1997.

[23] D. W. Ladoon, S. P. Schneider, and J. D. Schmisseur. Physics of resonance in a supersonic forward-facing cavity. *Journal of Spacecraft and Rockets*, 35(5):626–632, September-October 1998.

[24] W. A. Engblom, B. Yuceil, D. B. Goldstein, and D. S. Dolling. Experimental and numerical study of hypersonic forward-facing cavity flow. *Journal of Spacecraft and Rockets*, 33(3):353–359, May-June 1996.

[25] K. A. Hoffmann, Y. B. Suzen, and M. Papadakis. Numerical simulation of viscous flow for hypervelocity projectiles and interceptors with nose cavity. AIAA Paper 94-0213, January 1994.

[26] J. D. Kim and S. O. Park. Unsteady characteristics of hypersonic forward facing cavity flow. AIAA Paper 2000-3925, 2000.

[27] W. A. Engblom, D. B. Goldstein, D. Ladoon, and S. P. Schneider. Fluid dynamics of hypersonic forward-facing cavity flow. AIAA Paper 96-0667, January 1996.

[28] W. A. Engblom, B. Yuceil, D. B. Goldstein, and D. S. Dolling. Hypersonic forward-facing cavity flow: An experimental and numerical study. AIAA Paper 95-0293, January 1995.

[29] S. I. Silton and D. B. Goldstein. Use of an axial nose-tip cavity for delaying ablation onset in hypersonic flow. *Journal of Fluid Mechanics*, 528:297–321, 2005.

[30] S. J. Rufer. *Hot-Wire Measurements of Instability Waves on Sharp and Blunt Cones at Mach 6*. PhD thesis, Purdue University School of Aeronautics & Astronautics, December 2005.

[31] S. J. Rufer and S. P. Schneider. Hot-wire measurements of instability waves on cones at Mach-6. AIAA Paper 2006-3054, June 2006.

[32] M. Estorf, S. P. Schneider, and Graham V. Candler. Surface-pressure measurements of second-mode instability in quiet hypersonic flow. AIAA Paper 2008-1153, January 2008. To appear.

[33] S. P. Schneider. Effects of high-speed tunnel noise on laminar-turbulent transition. *Journal of Spacecraft and Rockets*, 38(3):323–333, May-June 2001.

[34] S. R. Pate. Radiated aerodynamic noise effects on boundary-layer transition in supersonic and hypersonic wind tunnels. *AIAA Journal*, 7(3):450–457, March 1969.

[35] I. E. Beckwith. Development of a high Reynolds number quiet tunnel for transition research. *AIAA Journal*, 13(3):300–306, March 1975.

[36] S. P. Schneider and C. E. Haven. Quiet-flow Ludwieg tube for high-speed transition research. *AIAA Journal*, 33(4):688–693, April 1995.

[37] S. P. Schneider, S. H. Collicott, J. D. Schmisseur, D. Ladoon, L. A. Randall, S. E. Munro, and T. R. Salyer. Laminar-turbulent transition research in the Purdue Mach-4 quiet-flow Ludwieg tube. AIAA Paper 96-2191, June 1996.

[38] S. P. Schneider and S. E. Munro. Effects of heating on quiet flow in a Mach 4 Ludwieg tube. *AIAA Journal*, 36(5):872–873, 1998.

[39] S. E. Munro. Effects of elevated driver-tube temperatures on the extent of quiet-flow in the Purdue Ludwieg tube. Master's thesis, Purdue University School of Aeronautics & Astronautics, December 1996.

[40] L. M. Fingerson and P. Freymuth; edited by R. J. Goldstein. *Fluid Mechanics Measurements*, chapter 3-7, Thermal Anemometers: Heat Transfer From Fine Wires. Taylor & Francis, 2nd edition, 1996.

[41] E. F. Spina and C. B. McGinley. Constant-temperature anemometry in hypersonic flow: Critical issues and sample results. *Experiments in Fluids*, 17(6):365–374, October 1994.

[42] Newport Corporation. Vibration control system instruction manual, 1991. P/N 18615-01 Rev. H IN-04913 (08-00).

[43] E. Hecht. *Optics*. Addison Wesley Longman, Inc., 4th edition, 2002.

[44] New Focus Inc. 80-mhz balanced photoreceivers model 18x7 user's guide, 2003. Document Number 181710 Rev. A.

[45] H. W. Liepmann and A. Roshko. *Elements of Gasdynamics*, chapter 4-14, Detached Shocks. John Wiley & Sons Inc., 1st edition, 1957.

APPENDIX

A. System Drawings

Detailed LDI layout drawings as assembled in the BAM6QT are shown in Figures A.1 & A.2. Figure A.1 shows a top view of the source end of the system, from the laser head to the mirrors that rise the beams, to the test section. Figure A.2 shows a top view of the receiver end of the system, from the mirrors that lower the beams back to the original level, to the last adjustable aperture. Note that both drawings are made to scale, and the rails, damped rods, rail carriers, and riser plates are drawn at their actual positions in the optical breadboard.

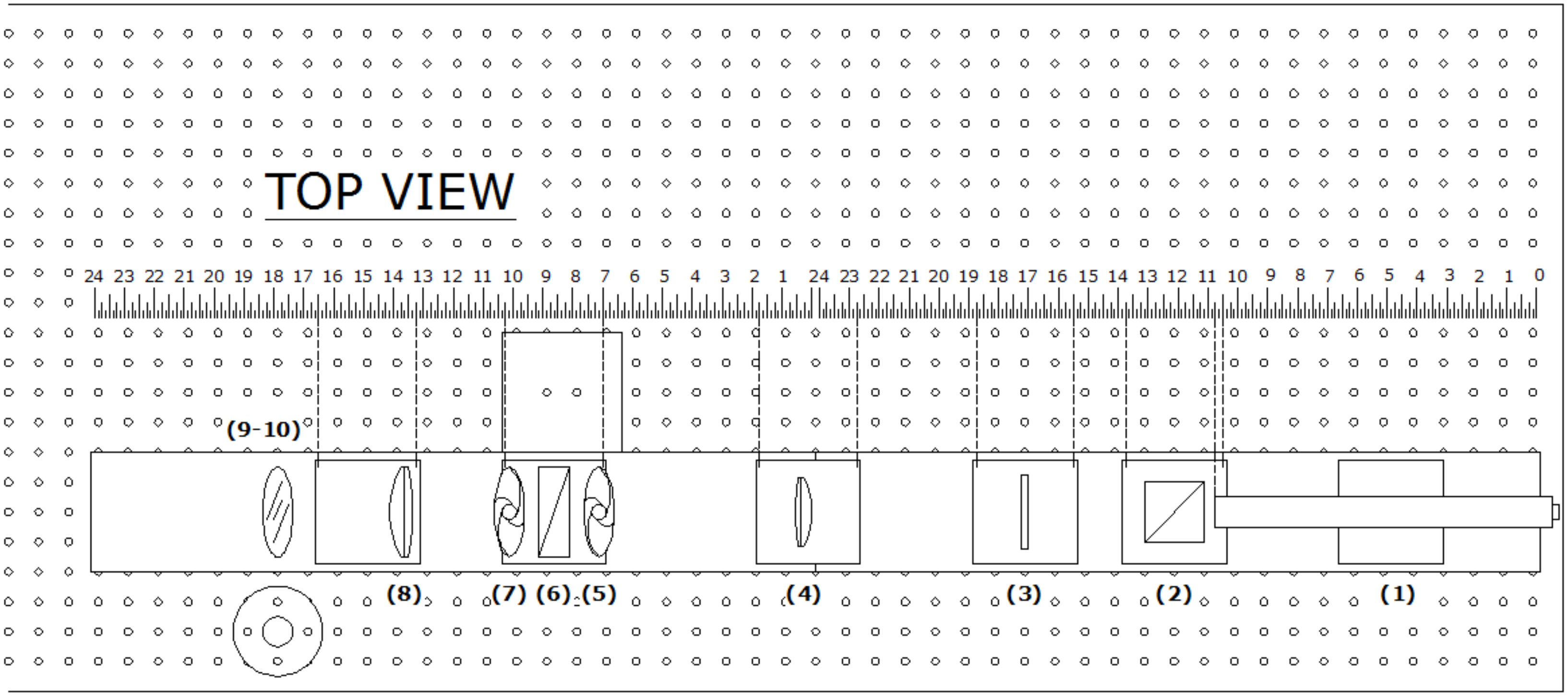

NOTE: All rail carriers slide on four 24" rails (Newport PRL-24). The ruler refers to the inches scale on the rails.

(1) Laser Aperture. The position of the rail carrier is not fixed as the laser can be shifted in the mount. Mounted on a tip/tilt laser mount (Newport ULM-TILT), above a 0.5" riser plate (Model MRP4), above a translational stage (Newfocus 9067), above a precision rail carrier (Newport PRC-3).
(2) Polarising beam splitting cube. Mounted on a 3-axis tilt stage (Newport P032N), above a 1.0" riser plate (Model MRP4), above a precision rail carrier (Newport PRC-3).
(3) Quarter-wave plate. Mounted on a rotational stage (Newport RSP-1T), above one 1.0", one 0.5", and one 0.25" riser plates (Model MRP4), on a precision rail carrier (Newport PRC-3).
(4) Achromatic doublet (f=125 mm). Mounted on a 3-axis translational mount (Newport LP-1A-XYZ), above a 0.5" riser plate (Model MRP4), above a precision rail carrier (Newport PRC-3).
(5) Adjustable aperture (Newport ID-1.0). Mounted on a 3-axis translational stage (Newport MT-XYZ with MT-CL clamp), above one 1.0", and one 0.25" riser plates (Model MRP4), above a precision rail carrier (Newport PRC-3).
(6) Wollaston prism. Mounted on a rotational stage (Newport RSP-1T) which is mounted on a 3-axis translational stage (Newport 562-XYZ), above two 1.0", and one 0.25" riser plates (Model MRP4).
(7) Adjustable aperture(Newport ID-1.0). Mounted on a 3-axis translational stage (Newport MT-XYZ with MT-CL clamp), above same riser plates and precision rail carrier as (5).
(8) Achromatic doublet (f=120.2 mm). Mounted on a 3-axis translational mount (Newport LP-2A-XYZ), above a precision rail carrier (Newport PRC-3).
(9)-(10) Pyrex mirrors. Mounted on tip/tilt mounts (Newport U200-AC2K) with custom-made aluminum standoffs, attached to sliding rod clamps (Newport 370-RC) that slide on steel damped rods (Newport 71, 75).

Figure A.1: Dimensioned LDI layout (part I), source end

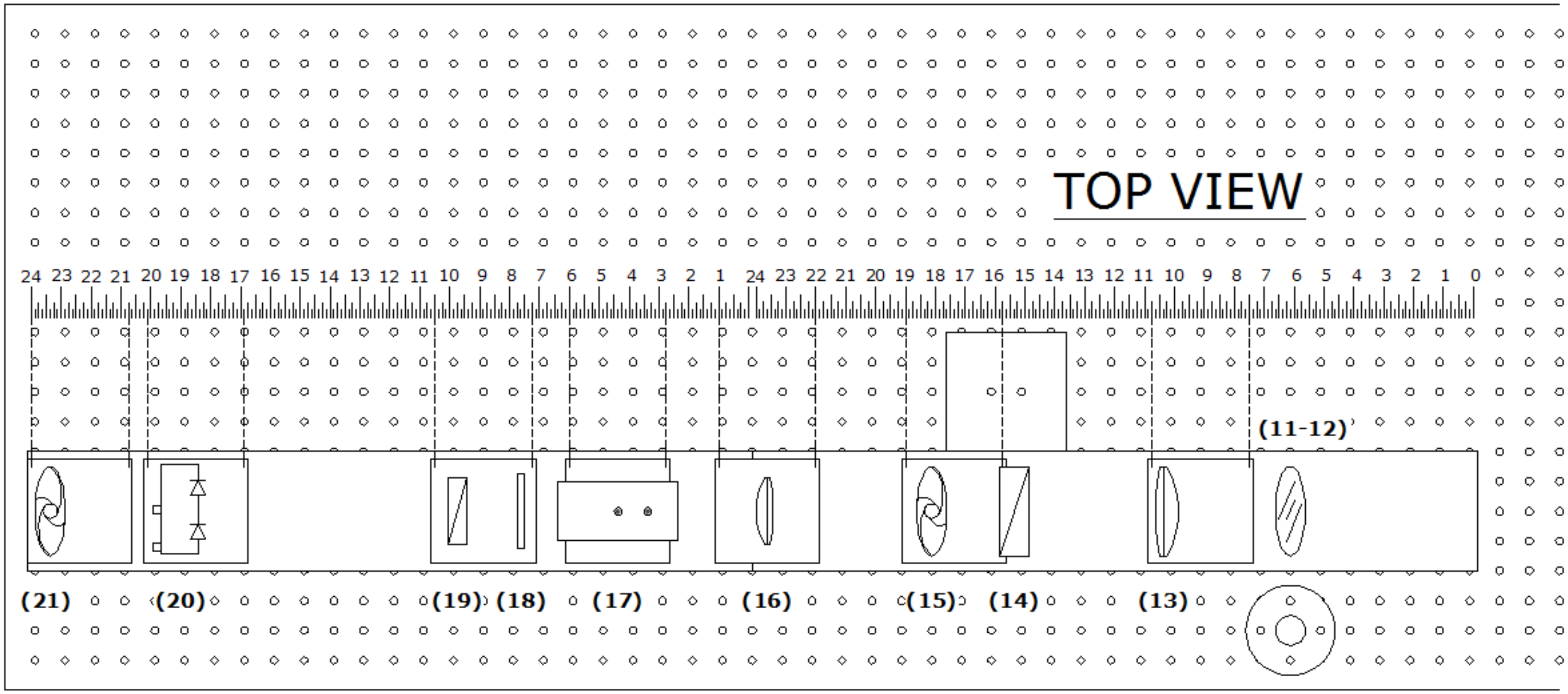

NOTE: All rail carriers slide on four 24" rails (Newport PRL-24). The ruler refers to the inches scale on the rails.

(11)-(12) Pyrex mirrors. Mounted on tip/tilt mounts (Newport U200-AC2K) with custom-made aluminum standoffs, attached to sliding rod clamps (Newport 370-RC) that slide on steel damped rods (Newport 71, 75).
(13) Achromatic doublet (f=120.2 mm). Mounted on a 3-axis translational mount (Newport LP-2A-XYZ), above a precision rail carrier (Newport PRC-3).
(14) Wollaston prism. Mounted on a rotational stage (Newport RSP-1T) which is mounted on a 3-axis translational stage (Newport 562-XYZ), above two 1.0", and one 0.25" riser plates (Model MRP4).
(15) Adjustable aperture (Newport ID-1.0). Mounted on a 3-axis translational stage (Newport MT-XYZ with MT-CL clamp), above one 1.0", and one 0.25" riser plates (Model MRP4), above a precision rail carrier (Newport PRC-3).
(16) Achromatic doublet (f=125 mm). Mounted on a 3-axis translational mount (Newport LP-1A-XYZ), above a 0.5" riser plate (Model MRP4), above a precision rail carrier (Newport PRC-3).
(17) Phase modulator. Mounted on custom mount, above a 1.0" riser plate (Model MRP4), above a precision rail carrier (Newport PRC-3).
(18) Quarter-wave plate. Mounted on a rotational stage (Newport RSP-1T), above one 1.0", one 0.5", and one 0.25" riser plates (Model MRP4), on a precision rail carrier (Newport PRC-3).
(19) Wollaston prism. Mounted on a rotational stage (Newport RSP-1T), above same riser plates and precision rail carrier as (18).
(20) Balanced photodiode receiver. Mounted on translational stage (Newport 422-05S), above one 1.0", and one 0.25" riser plates (Model MRP4), above a precision rail carrier (Newport PRC-3).
(21) Adjustable aperture (Newport ID-1.0). Mounted on a 3-axis translational stage (Newport MT-XYZ with MT-CL clamp), above one 1.0", and one 0.25" riser plates (Model MRP4), above a precision rail carrier (Newport PRC-3).

Figure A.2: Dimensioned LDI layout (part II), receiver end

B. System Photographs

High resolution photographs of the PQFLT facility are shown in Figures B.1 - B.12.

Photographs of the LDI as it was assembled in the PQFLT are shown in Figures B.13 - B.21.

Photographs of the LDI as it was assembled in the BAM6QT are shown in Figures B.17 - B.19.

The vibration control system in the BAM6QT is shown in Figure B.20.

Photographs of the custom-made electronics used in this research are shown in Figures B.22 - B.26.

Photographs of the hemispherical nose model, and the forward-facing cavity models built for the PQFLT and the BAM6QT are shown in Figures B.27 - B.29.

Figure B.1: Aerospace Science Laboratory at Purdue University (aerial photo by Katya Casper)

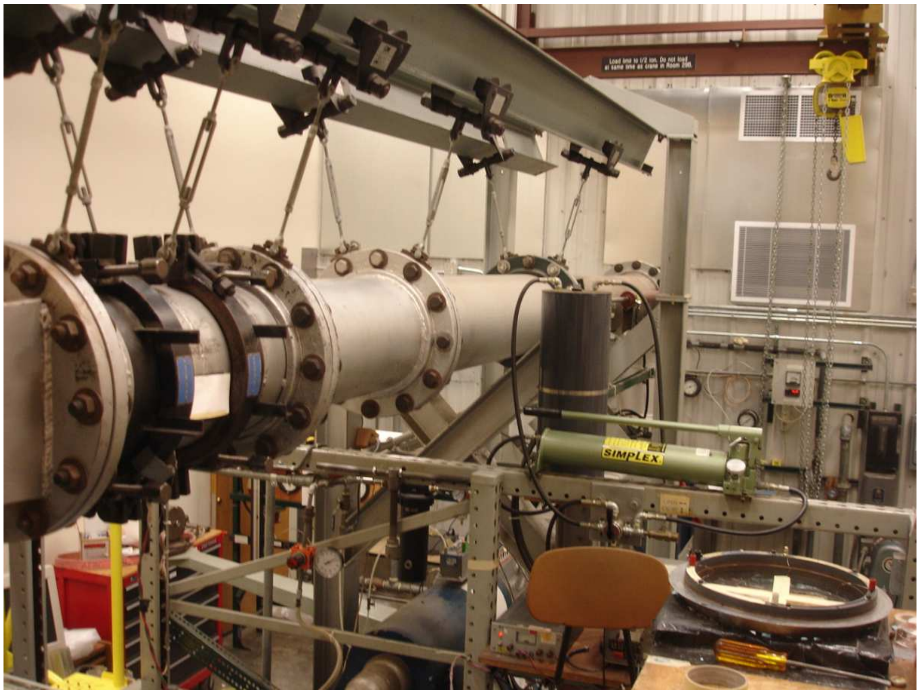

Figure B.2: PQFLT facility, diffuser and diaphragm burst section

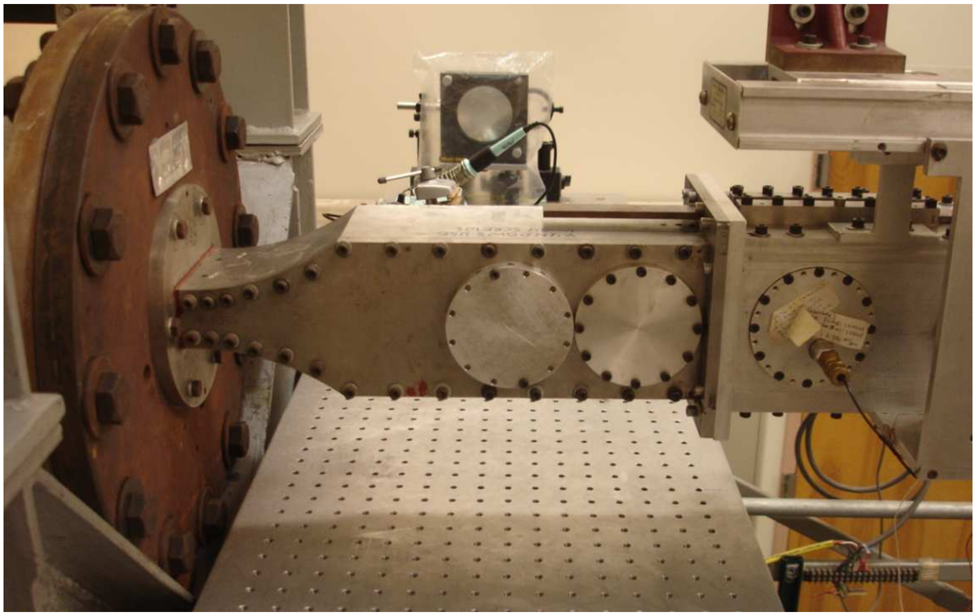

Figure B.3: PQFLT facility, nozzle and portal windows

Figure B.4: PQFLT facility, Mach 4 nozzle

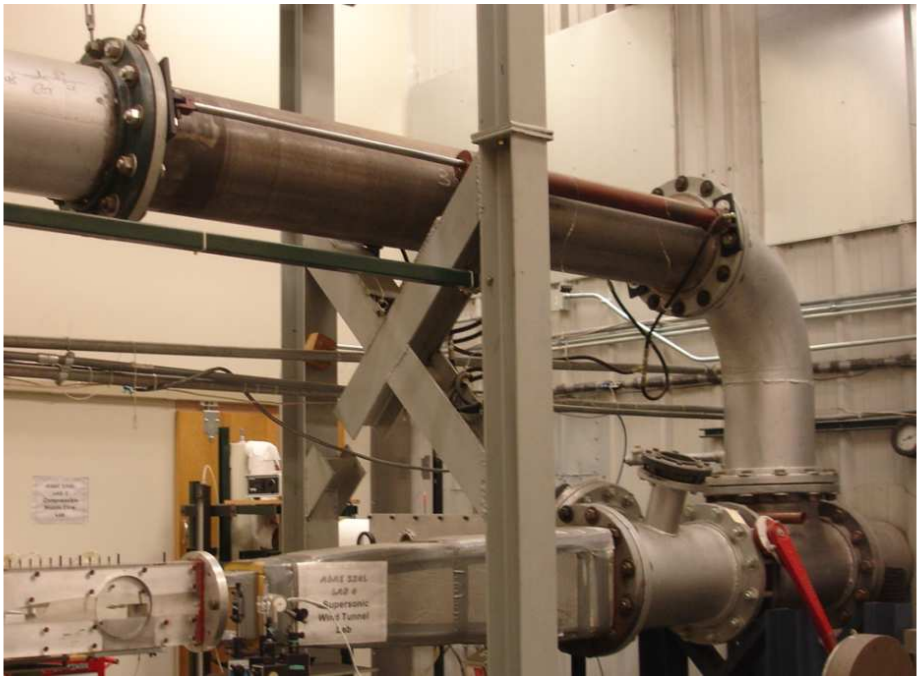

Figure B.5: PQFLT facility, sliding sleeve

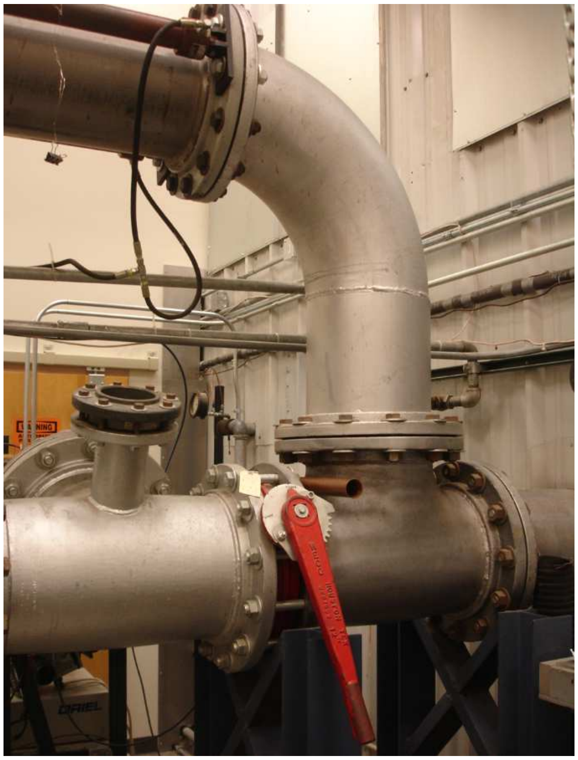

Figure B.6: PQFLT facility, flapper valve junction

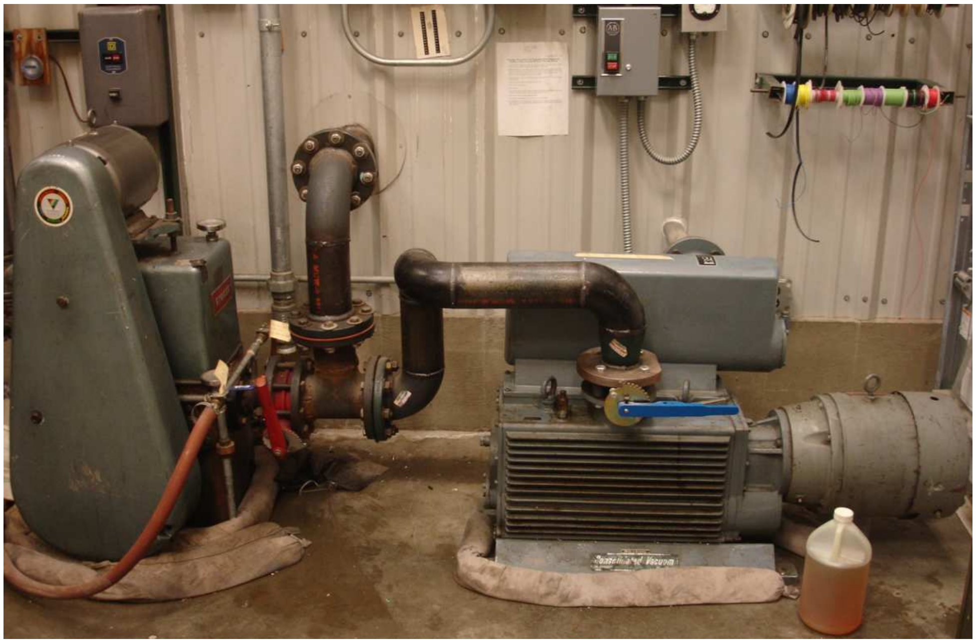

Figure B.7: PQFLT facility, vacuum pumps

Figure B.8: PQFLT facility, vacuum tank

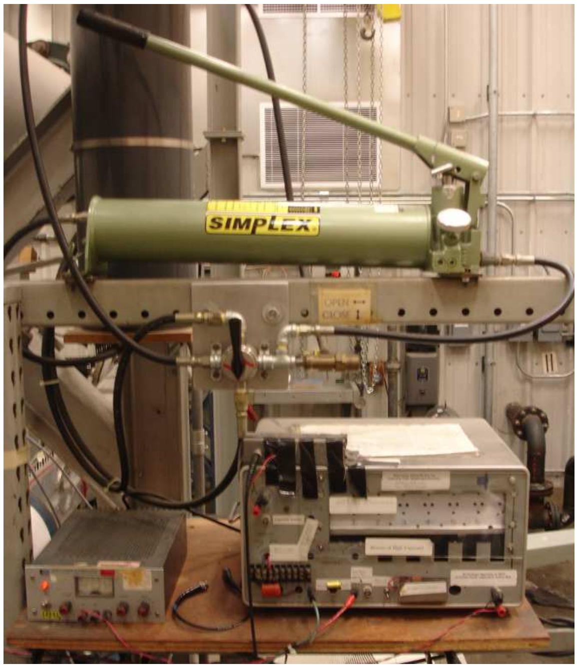

Figure B.9: PQFLT facility, sliding sleeve controls and diaphragm burst electronics

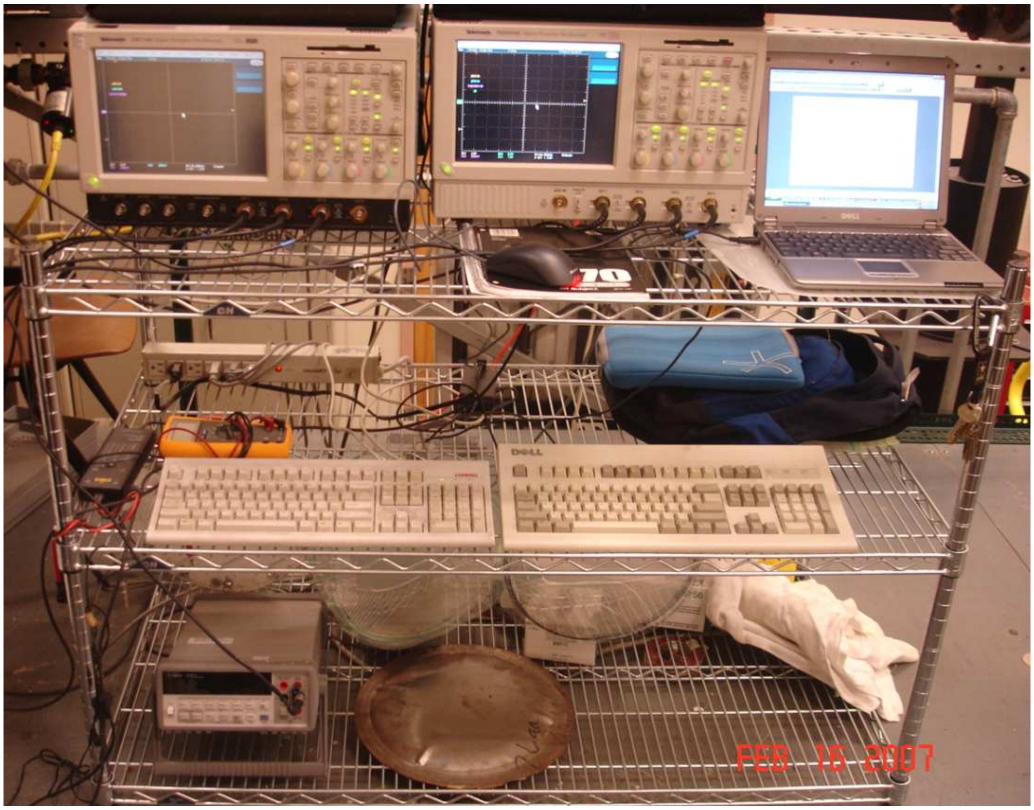

Figure B.10: PQFLT facility, instrumentation work desk

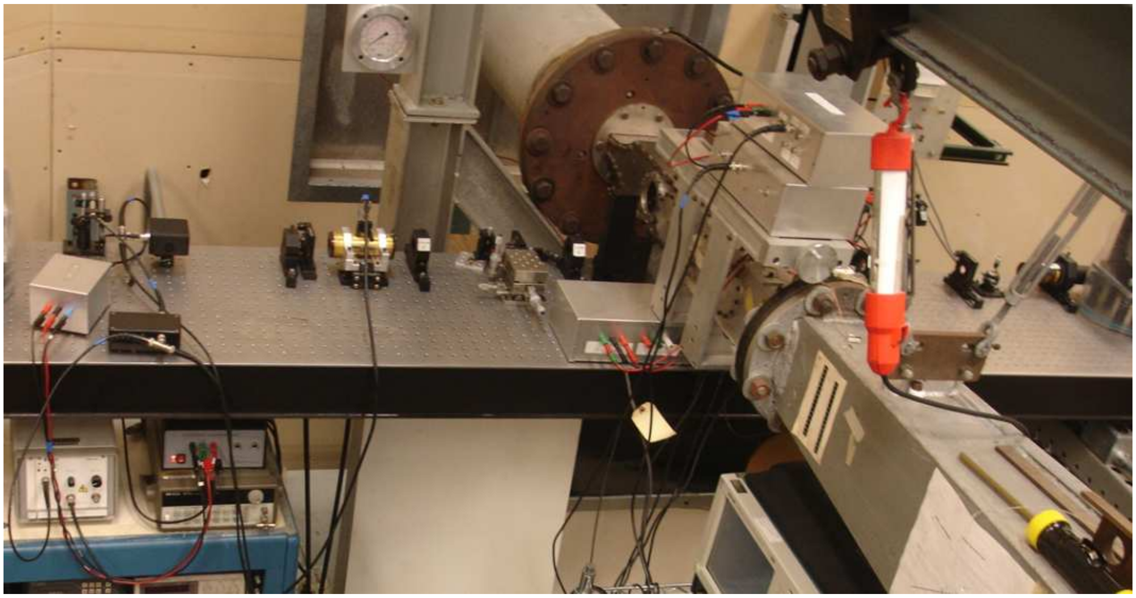

Figure B.11: PQFLT facility, LDI optical table

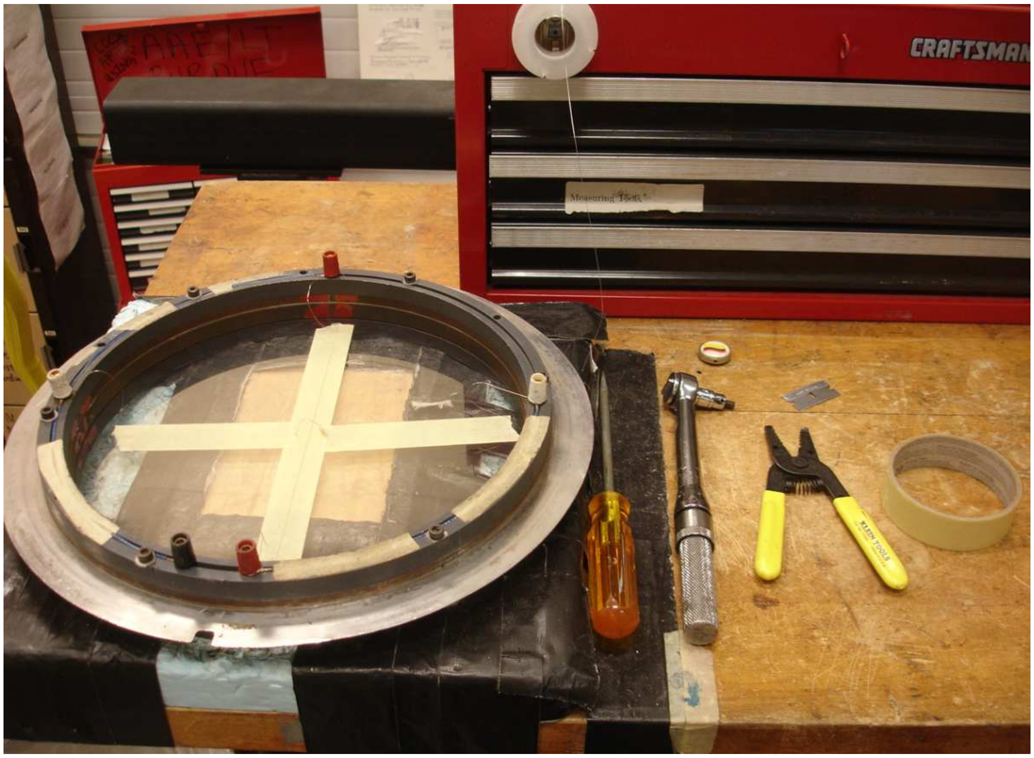

Figure B.12: PQFLT facility, diaphragm assembly workbench

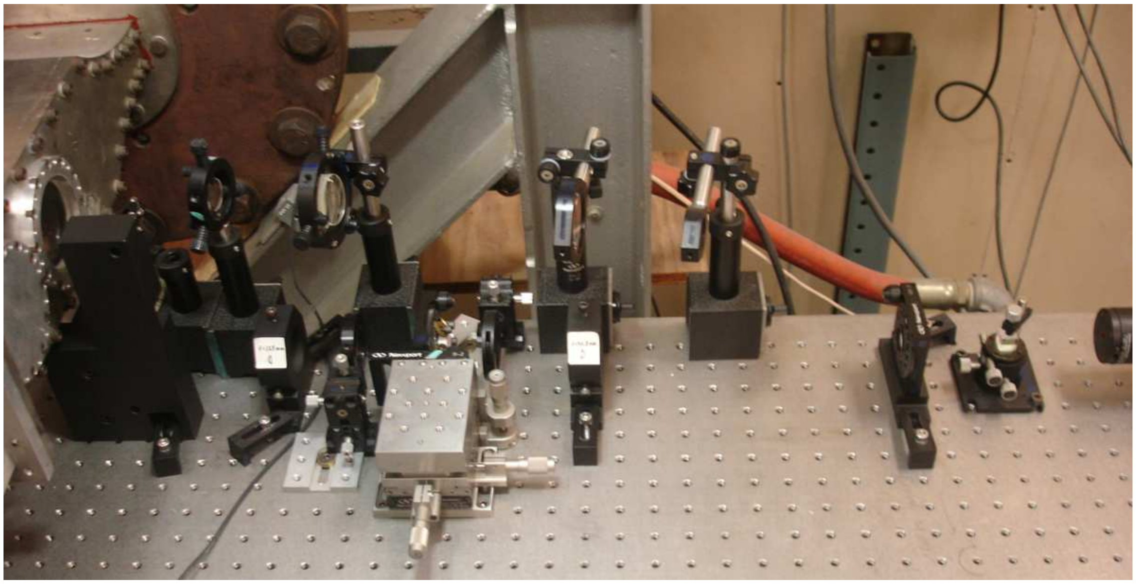

Figure B.13: PQFLT facility, optics breadboard (source end), top view

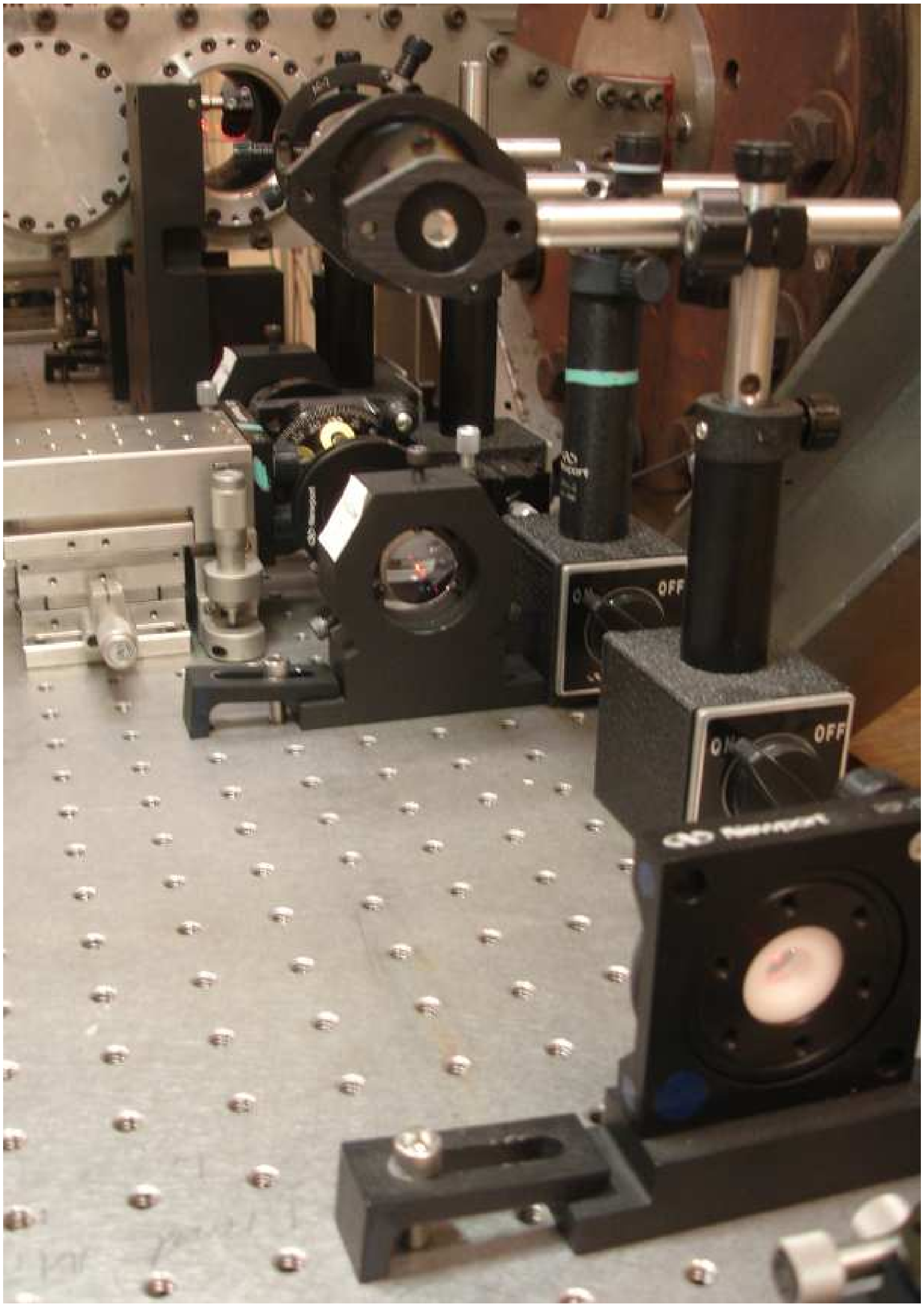

Figure B.14: PQFLT facility, optics breadboard (source end), angled view

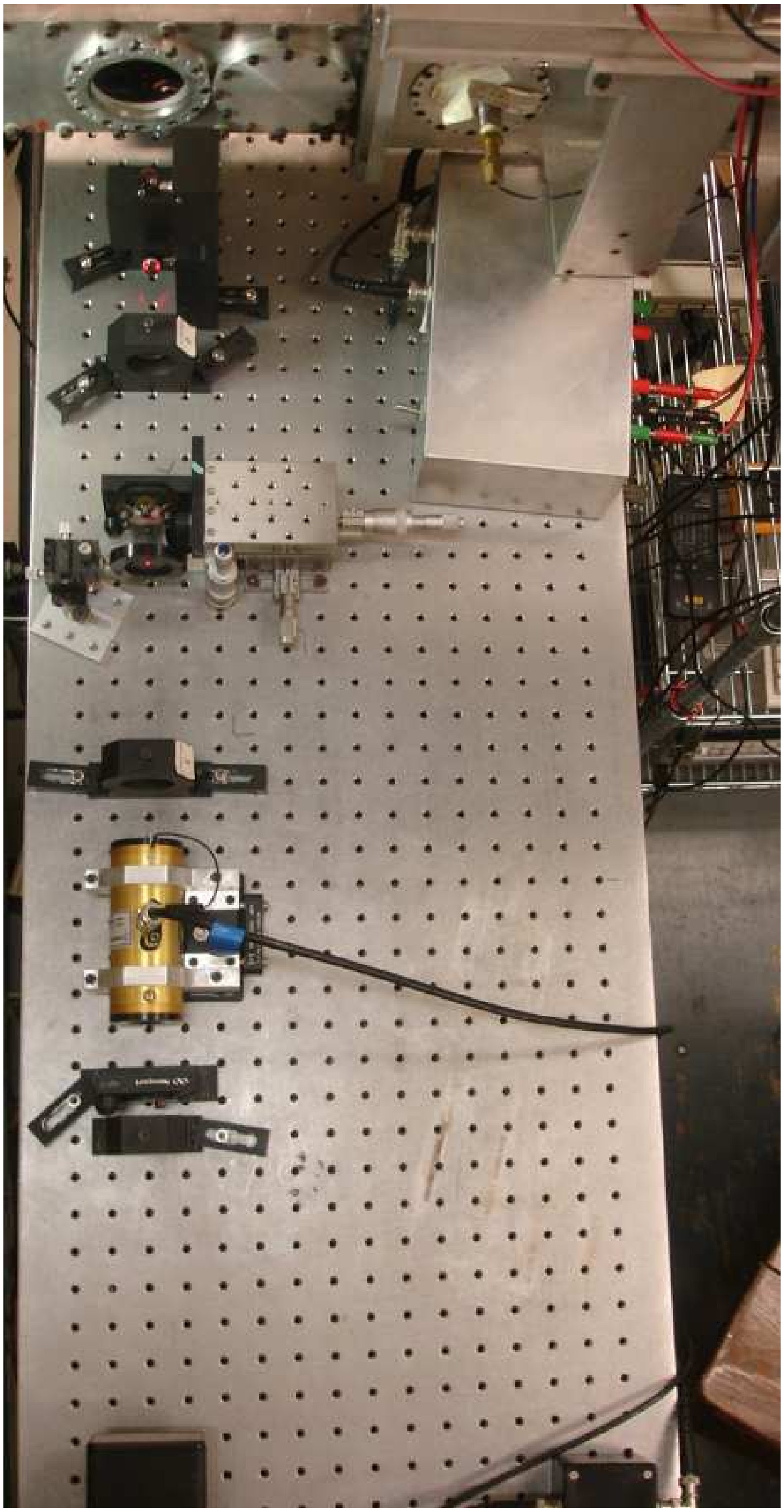

Figure B.15: PQFLT facility, optics breadboard (receiver end), top view

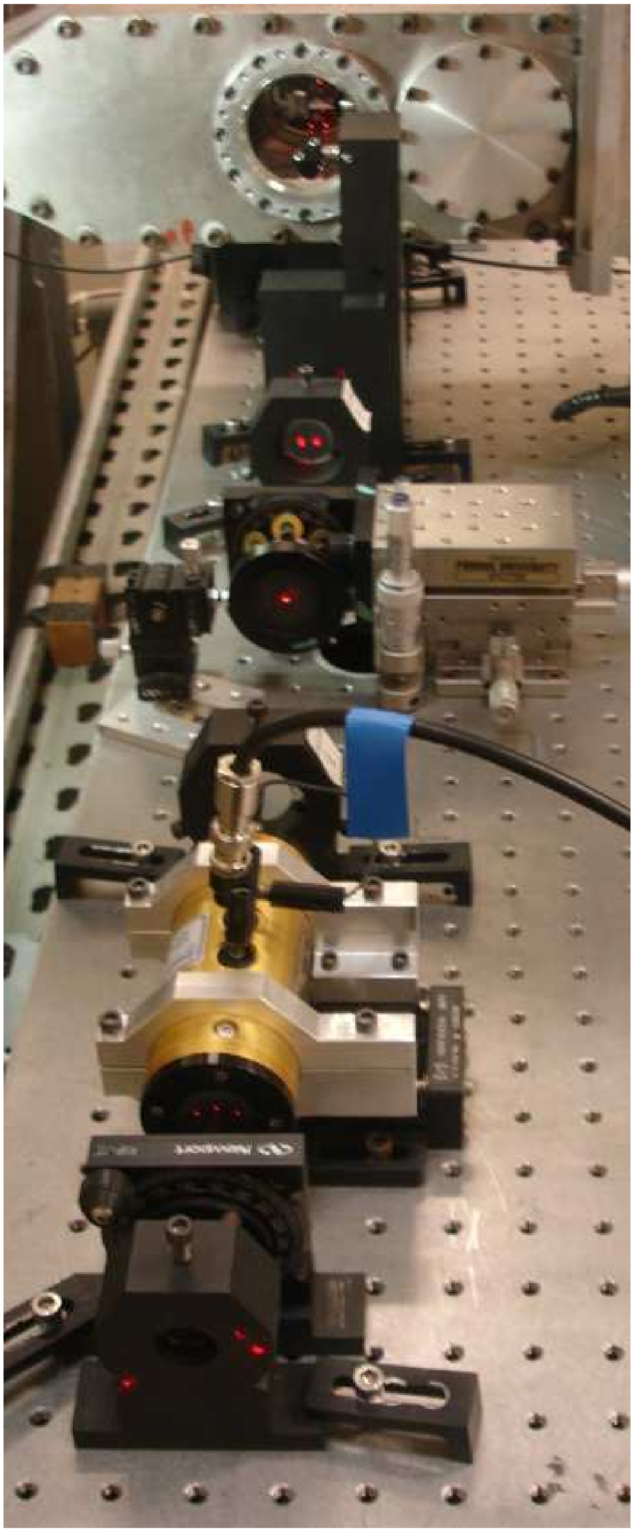

Figure B.16: PQFLT facility, optics breadboard (receiver end), angled view

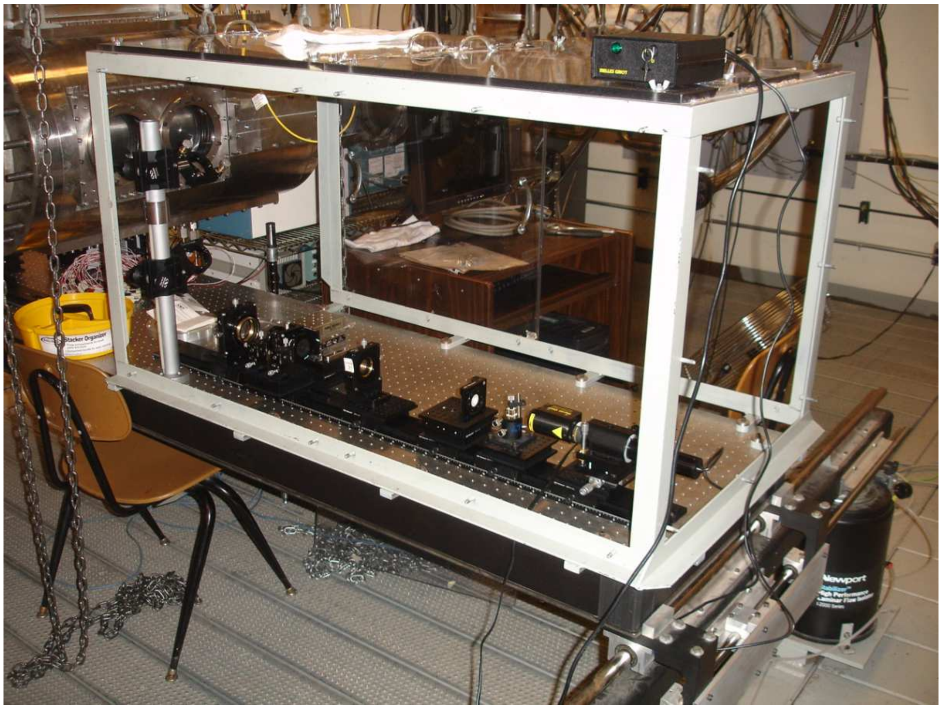

Figure B.17: BAM6QT facility, optics breadboard (source end), angled view

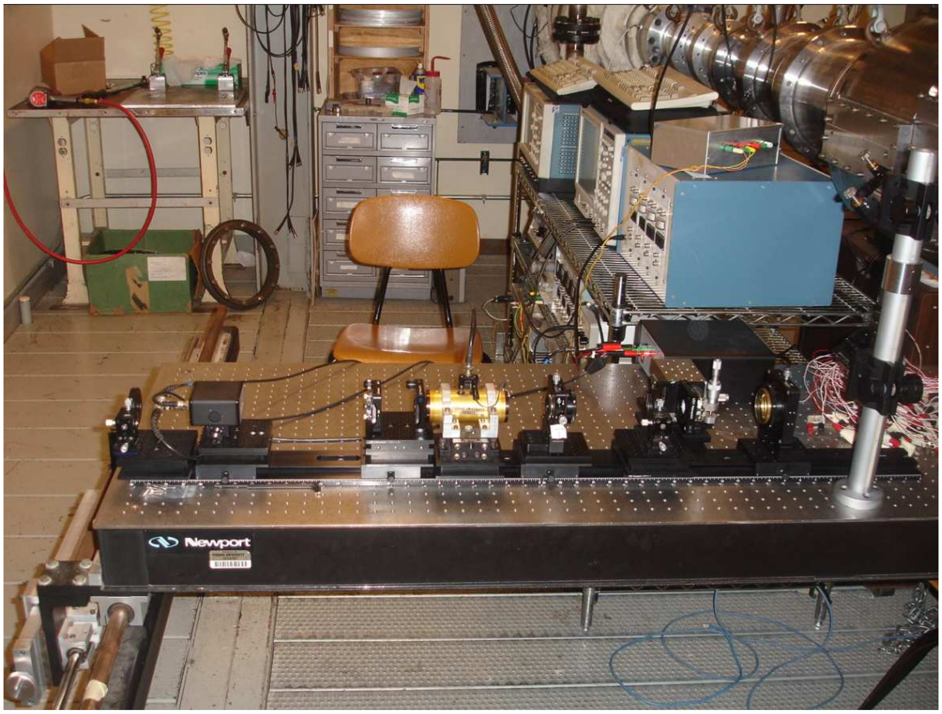

Figure B.18: BAM6QT facility, optics breadboard (receiver end), front view

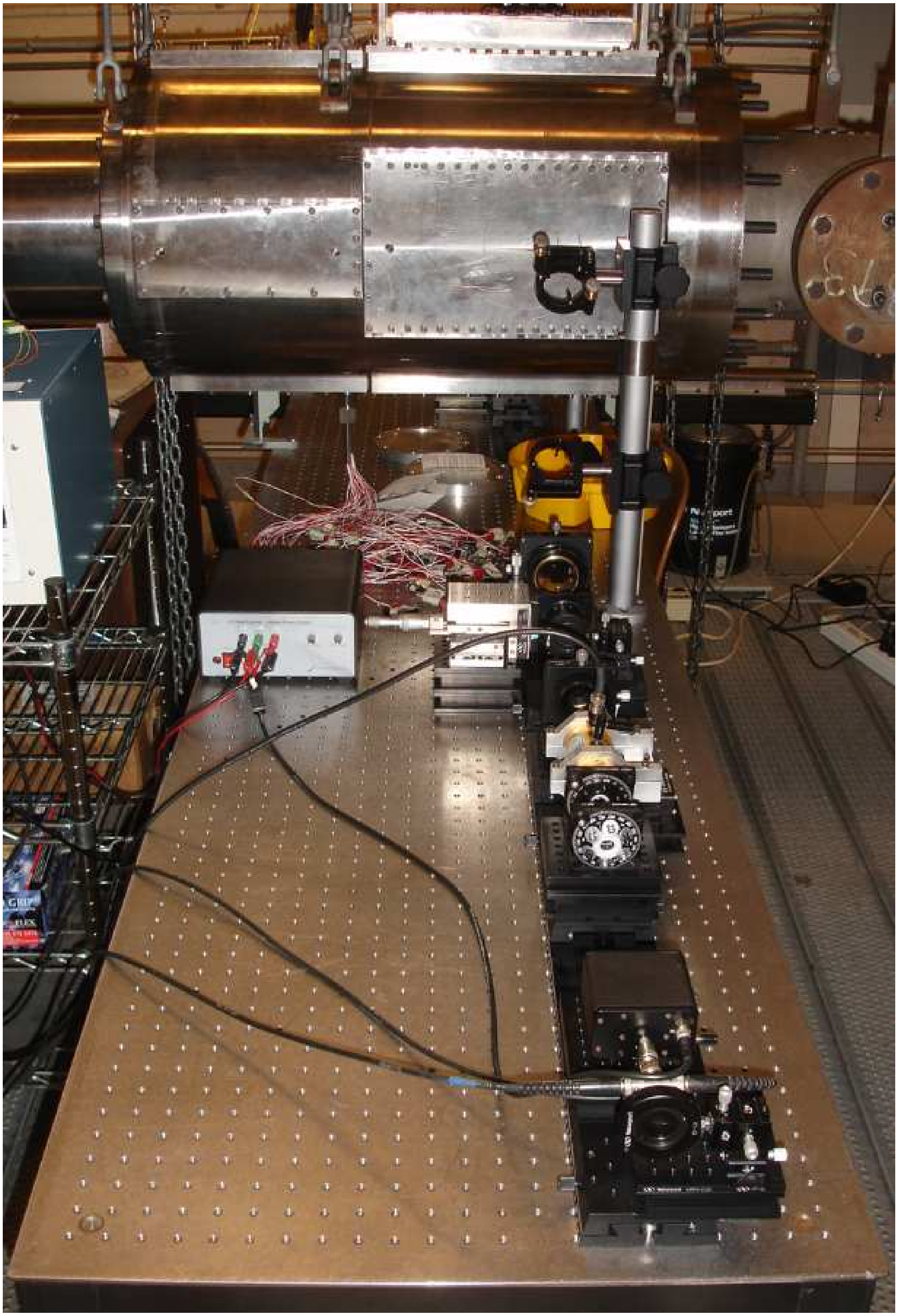

Figure B.19: BAM6QT facility, optics breadboard (receiver end), side view

Figure B.20: BAM6QT facility, vibration control system

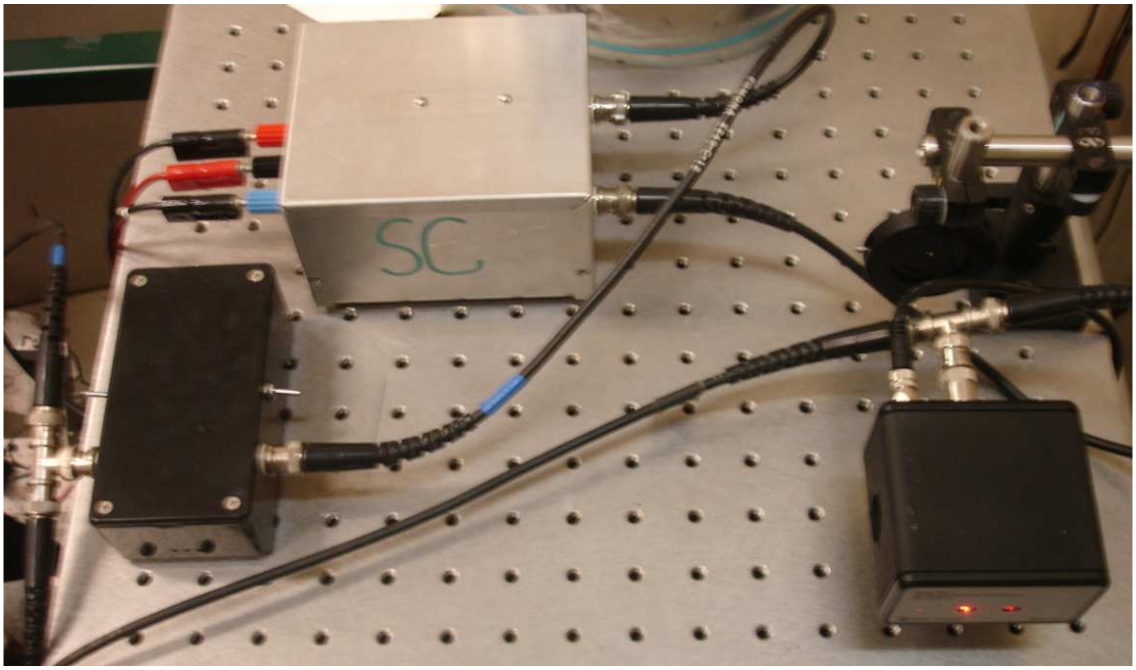

Figure B.21: Balanced photoreceiver, low-pass filter, and integrator

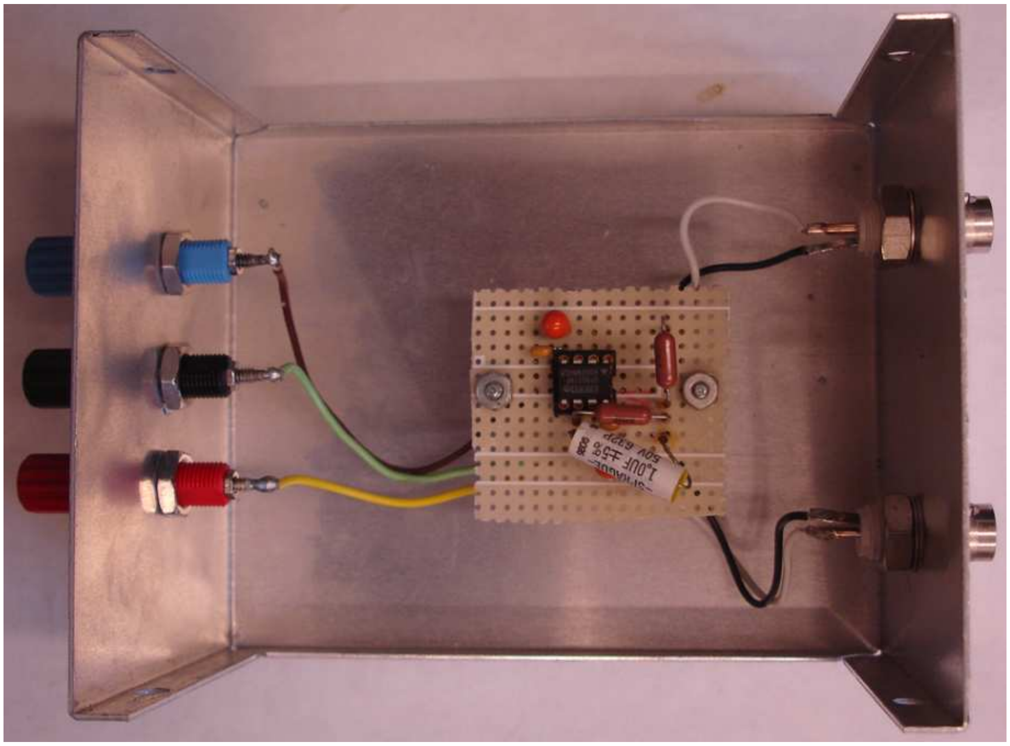

Figure B.22: Low-pass filter

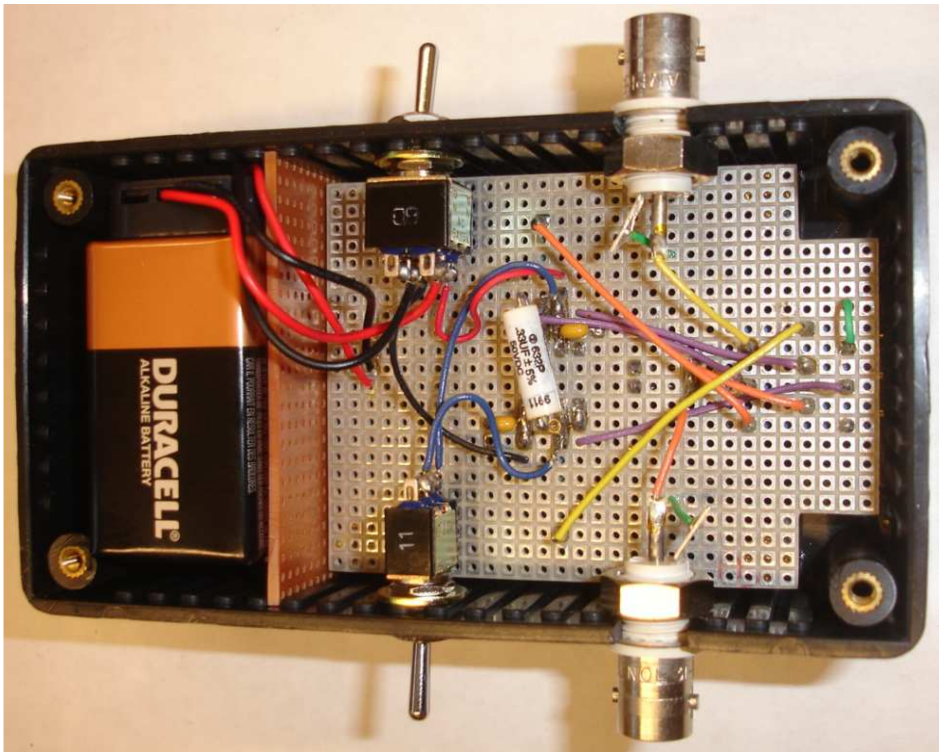

Figure B.23: Integrator

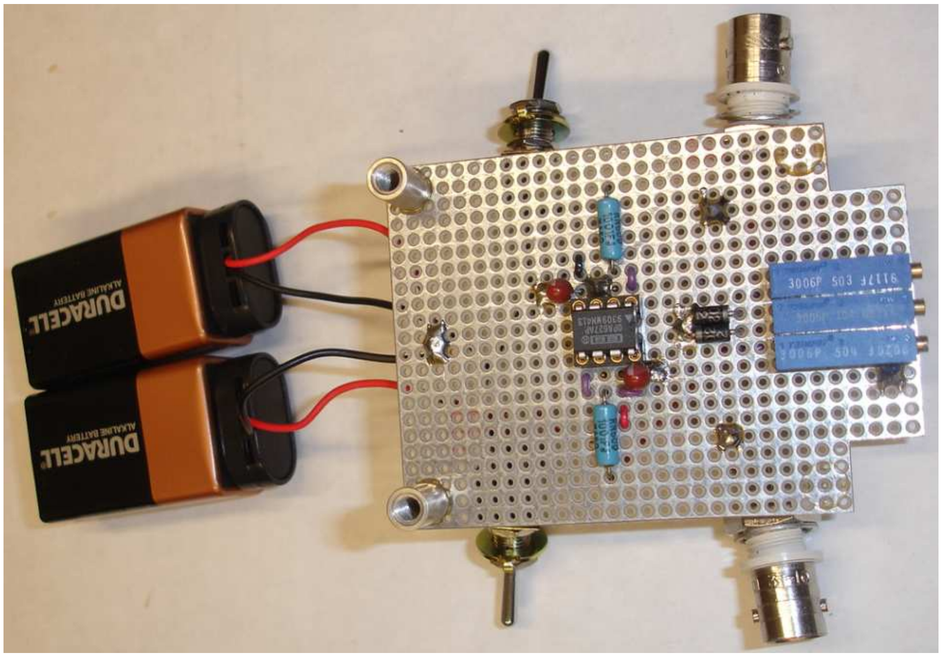

Figure B.24: Integrator, circuit board exposed

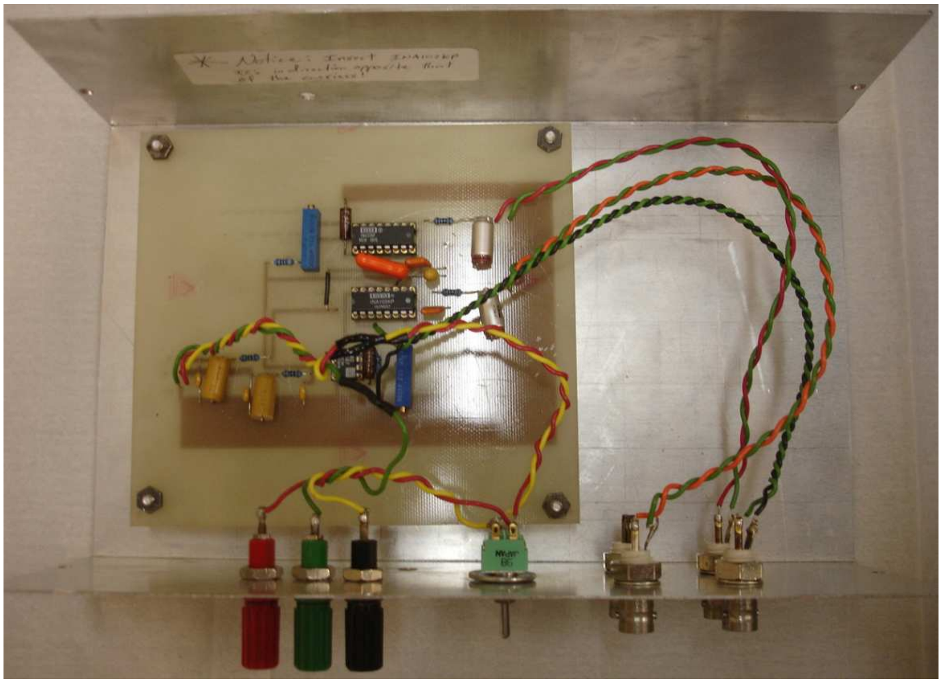

Figure B.25: Kulite box

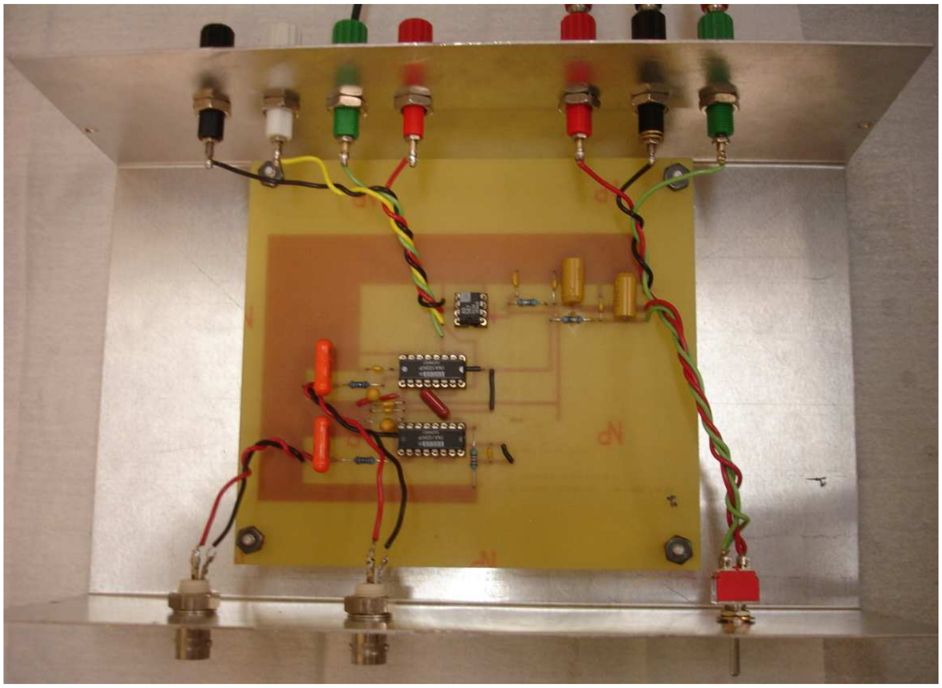

Figure B.26: Constant current anemometer

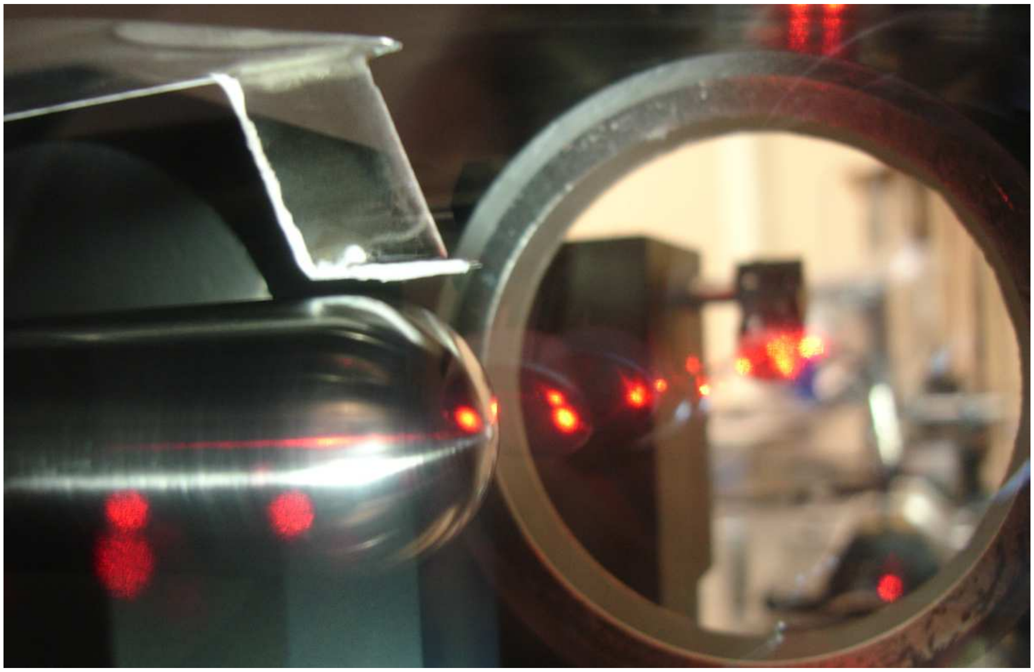

Figure B.27: Hemispherical nose model inside PQFLT

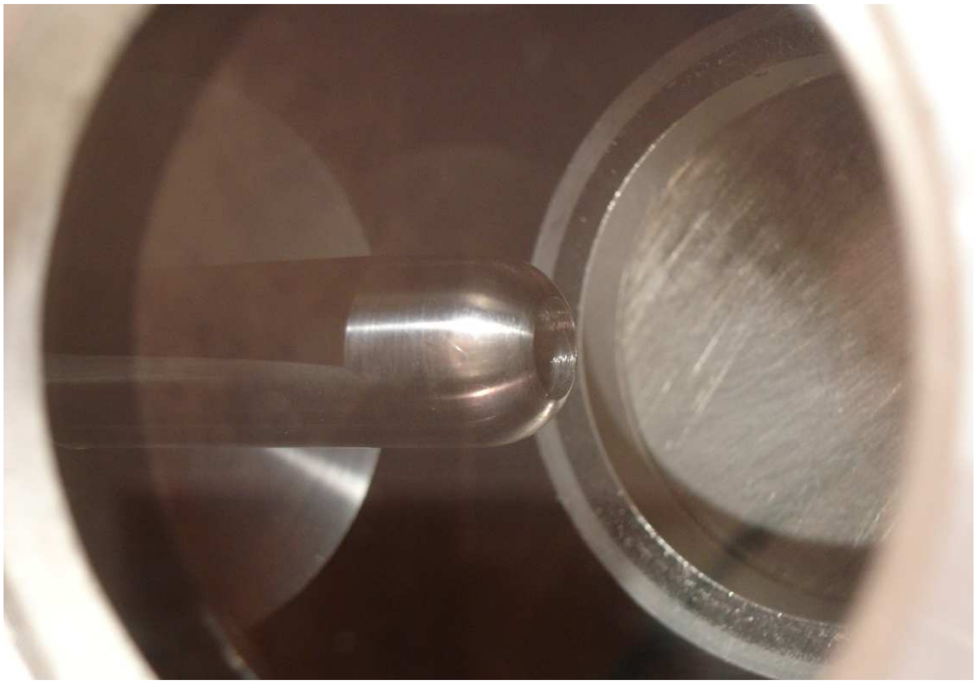

Figure B.28: Forward-facing cavity model inside PQFLT

Figure B.29: Forward-facing cavity model to be used in BAM6QT

C. LDI Alignment Procedure

The detailed alignment procedure given below is for the LDI system currently assembled in the BAM6QT on four precision optical rails (Newport model PRL-24) mounted on an optical breadboard with mounting holes spaced evenly on a 1 in grid. Detailed dimensioned schematics of the system are shown in Figures A.1 & A.2. Exact optical component positions for the laser beams to be focused under the BAM6QT test section and on the surface of the photodiodes should be taken from those drawings.

1. Turn on the intensity-stabilized He-Ne laser's low voltage power supply and the high voltage power supply in this order. Wait approximately 20 minutes for the laser system to stabilize. When the system is stable, the light on the laser head shines green.
2. The laser used is polarized so it must be rotated correctly for optimal performance. Place the rail carriers with the laser head, and the polarizing beam splitting cube at their respective locations. Rotate the laser head so that linear polarization is horizontal. To do this, monitor the intensity of the beam passing through the cube as the laser is rotated. When the intensity is at a maximum, the angle of polarization is correct. Remove the rail carrier with the polarizing beam splitting cube and tighten the laser to its mount.
3. The quarter-wave plates and the third achromatic doublet are the only components of the system that lack a precision translational stage so the beam must be aligned to pass through their center first. Place the rail carriers with the two quarter-wave plates, the third wollaston prism, and all the adjustable apertures at their respective locations. Open the laser cavity and use the adjustable laser mount to direct the beam such that it passes through the center of both quarter

wave plates. Remove the rail carriers with the quarter-wave plates and adjust the position of the adjustable apertures using their respective precision translational stages such that the laser beam passes through their center. These are the permanent positions of these components which define the original beam path (do not modify the position of the adjustable apertures or the orientation of the laser head at any other point of the alignment procedure).

4. Place the rail carrier with the polarizing beam splitting cube again. Precisely adjust its tilt, using the mount, so that the beam remains in its original path (passes through the center of the first and last adjustable aperture).

5. Place the rail carrier with the first quarter-wave plate after the polarizing beam splitting cube in its designated location. For the time being, the angular position of the plate is not important. It will be adjusted later when the probe beams which pass through the test section have been formed.

6. Place the rail carrier with the first achromatic doublet (with the most curved surface towards the laser) after the quarter-wave plate in its designated location. Precisely adjust the lateral position (in the direction perpendicular to the beam path) using the mount so that the beam remains in its original path. Note that the axial location (in the direction of the beams) of this lens varies depending on where the probe beams are focused.

7. The first two adjustable apertures should already be after the first achromatic doublet. These apertures are also used to block some of the unwanted back reflections. At this point the diameter of the beam should be small so both apertures can be reduced to its minimum area.

8. Bolt in the XYZ-translation-stage that holds the first Wollaston prism in its designated location. Precisely adjust its position and rotation using its stage and its mount such that the prism is between the first and second adjustable apertures, the laser beam passes through its center, and the beam separation orientation is the desired one. Open the second adjustable aperture such that

it just encompasses both beams. At this point the rotation of the first quarter-wave plate can be adjusted such that both beams have equal intensities.

9. Place the rail carrier with the second achromatic doublet after the second adjustable aperture in its designated location (at a distance exactly equal to its focal length from the first Wollaston prism, and with its most curved surface away from the laser). Precisely adjust its position using the mount so that both beams pass through the lens, and become parallel.
10. Place the rail carrier with the third achromatic doublet after the second one in its designated location (on the opposite side of the test section with its most curved surface towards the laser). Precisely adjust its position using the mount so that both beams pass through the lens.
11. Bolt in the XYZ-translation-stage that holds the second Wollaston prism in its designated location (at a distance from the third achromatic doublet exactly equal to its focal length). Precisely adjust its position using the stage such that the two beams meet at the prism, become coincident, and only one laser beam can be seen leaving the prism. Further fine adjust the lateral position of the second and third achromatic doublets so that the resulting-single beam lies on the original beam path.
12. At this point, the four mirrors used to traverse the beams up, through the test section, and back down to the original beam path height can be placed between the second and third achromatic doublets. Note that due to time restrictions, only the basic performance experiments were made in the BAM6QT with the beams passing under the test section and these mirrors were not used in this research. The author recommends the following hypothetical procedure for aligning them: Bolt the holding posts to the breadboard in their designated locations. Adjust the height and tilt of the mirrors so that the beams are centered on the first mirror, but close to the edge of the second mirror. Direct the beams from the second mirror to the opposite edge of the third mirror. These

slight offsets at the second and third mirrors allow the beams to pass through the test section at a small angle, necessary to ensure that back reflections from the windows are blocked by the adjustable apertures. Direct the beams from the third mirror to the center of the fourth mirror near the breadboard surface, and then back to their original beam path.

13. Note that after raising the probe beams to pass through the test section, the axial location of the first achromatic doublet must be adjusted to focus them at the desired location (be careful not to move it laterally).
14. The third adjustable aperture should already be after the second Wollaston prism. At this point the diameter of the beam should also be small so the aperture can again be reduced to its minimum area.
15. Place the rail carrier with the fourth achromatic doublet (with the most curved surface away from the laser) after the third adjustable aperture in its designated location. Precisely adjust the lateral position using the mount so that the beam remains in its original path. Note that the axial location of this lens also varies depending on where the probe beams are focused.
16. Place the rail carrier with the phase modulator after the fourth achromatic doublet in its designated location. For a probe beam separation parallel to the breadboard, it should be rotated with the power jacks facing up and the top (and bottom) side of the square apertures parallel to the breadboard surface. This ensures that the crystals in the phase modulator will affect only one of the beams passing through it. Precisely adjust the orientation using the mount so that the beam passes through the center of the square apertures and remains in its original path.
17. Place the rail carrier with the second quarter-wave plate and the third Wollaston prism after the phase modulator in its designated location. Precisely adjust the rotation of the third Wollaston prism using the mount so that the beam is split parallel to the breadboard surface.

18. At this point, the interferometer can be aligned to infinite fringe spacing. To do this, place a white sheet of paper after the third Wollaston prism. If the alignment up to this point was done correctly, interference fringes should be visible in both beam spots. Precisely adjust the rotation of the second Wollaston prism using the mount so that the orientation of the fringes is perpendicular to the breadboard surface. Next, precisely adjust the rotation of the second quarter-wave plate using the mount to achieve maximum fringe contrast. Lastly, precisely adjust the axial location of the second Wollaston prism using the stage to achieve infinite fringe spacing.

19. Place the the rail carrier with the balanced photodiode receiver after the third Wollaston prism at its designated location.

20. The following is the final alignment procedure of the LDI. It should be performed every time the system is used to maintain optimal performance. Adjust the lateral location of the fourth achromatic doublet and the rotation of the third Wollaston prism, using their respective mounts, so that the beams shine on the photodiodes. Then, further adjust the axial, and vertical location of the fourth achromatic doublet to focus the beams exactly on the center of the photodiodes. Connect the photoreceiver to an oscilloscope and monitor its output moving the second Wollaston prism laterally. Repeat this final adjustment procedure until the output of the photoreceiver fluctuates symmetrically around zero when the prism is shifted.

D. Computer Codes

All the codes to used to analyze and process the data used in this research have been verified to run on MATLAB version 7.0.1.24704.

D.1 Tektronix .wfm File Reading Code

The code used to read the Tektronix oscilloscopes .wfm files is listed below.

```
%MATLAB function that reads in a Tektronix file and writes a MATLAB variable.

%Written by Craig Skoch January 10, 2003

%Originally worked with TDS5000/6000/7000 Series Scopes

%Modified by Craig Skoch August 19, 2005 to allow this program to work with
%Tektronix 5034B Scope  (Should work for all TDS5000B Series)

%Modified by Matt Borg November 21, 2006 to allow this program to work with
%Tektronix DPO7054 Scope (Should work for all DPO7000 Series)
%% The big changes are that there needs to be a shift of 4 bytes after
%% each of the following positions: 302, 458, 590, 722

%Command line should look like: [v,t]=tekread('tektronix filename')
%Currently doesn't work with FastFrame Data

function [A,t]=tekread(tekfile)
```

```
%tek_ptr=fopen(tekfile);
tek_ptr=fopen(tekfile,'r','b');%Open for read-only with big-endian format

fseek(tek_ptr,2,'bof');
vers=fread(tek_ptr,8,'char')';%Versioning number

%Account for 2 extra bytes in header for TDS5034B Scope at position 154
%TDS5034B Scope needs file reopened using little-endian format

if vers==':WFM#001'%Version Number for TDS7104 Scope
    shiftbytes=0;
elseif vers==':WFM#002'| vers==':WFM#003'%Version Number for TDS5034B Scope
%     and DPO7054, respectively
    shiftbytes=2;
    tek_ptr=fopen(tekfile);
 end

fseek(tek_ptr,0,'bof');
dec2hex(fread(tek_ptr,1,'uint16'),4);%Byte order verification

fseek(tek_ptr,2,'bof');
vers=fread(tek_ptr,8,'char')';%Versioning number

fseek(tek_ptr,10,'bof');
digbytecount=fread(tek_ptr,1,'char');%Num digits in byte count

fseek(tek_ptr,11,'bof');
fread(tek_ptr,1,'*int32');%Num of bytes to the end of file
```

```
fseek(tek_ptr,15,'bof');
bytesperpnt=fread(tek_ptr,1,'char');%Number of bytes per point
begbuff=fread(tek_ptr,1,'int32');%Byte offset to beginning of curve buffer

%fseek(tek_ptr,40,'bof')
%fread(tek_ptr,32,'char')%Waveform Label

fseek(tek_ptr,76,'bof');
hdrsize=fread(tek_ptr,1,'int16');%Size of Waveform Header

fseek(tek_ptr,122,'bof');
datatype=fread(tek_ptr,1,'int8');%Data Type

fseek(tek_ptr,166+shiftbytes,'bof');
Vscale=fread(tek_ptr,1,'double');%Voltage Scale

fseek(tek_ptr,174+shiftbytes,'bof');
Voff=fread(tek_ptr,1,'double');%Voltage Offset

fseek(tek_ptr,222+shiftbytes,'bof');
fread(tek_ptr,1,'double');%Voltage Resolution



if vers==':WFM#003';shiftbytes=shiftbytes+4;end
%% Insert code here if you want to look at data that is stored between 302
%% and 458
if vers==':WFM#003';shiftbytes=shiftbytes+4;end
```

```
fseek(tek_ptr,478+shiftbytes,'bof');
tscale=fread(tek_ptr,1,'double');%Time Scale

fseek(tek_ptr,486+shiftbytes,'bof');
toff=fread(tek_ptr,1,'double');%Time Offset

fseek(tek_ptr,494+shiftbytes,'bof');
numpts=fread(tek_ptr,1,'int32');%Record Length

if vers==':WFM#003';shiftbytes=shiftbytes+4;end
%% Insert code here if you want to look at data that is stored between 590
%% and 722
if vers==':WFM#003';shiftbytes=shiftbytes+4;end

fseek(tek_ptr,804+shiftbytes,'bof');
buffoffset=fread(tek_ptr,1,'int32');%Bytes of Buffer

fseek(tek_ptr,808+shiftbytes,'bof');
enddata=fread(tek_ptr,1,'int32');%Bytes from Beg Buffer to End of Data

numpts=(enddata-buffoffset)/bytesperpnt;

fseek(tek_ptr,buffoffset+begbuff,'bof');

if bytesperpnt==1
    A=fread(tek_ptr,numpts,'int8');
elseif bytesperpnt==2
    A=fread(tek_ptr,numpts,'int16');
end
```

```
t=(toff+tscale:tscale:toff+tscale*numpts)’;
A=A*Vscale+Voff;

fclose(tek_ptr);
```

D.2 Mean Flow and Freestream Noise Calculation

The code used to calculate the freestream noise levels and the mean flow parameters is listed below.

```
clear; clc; close all; clear variables
set(0,’RecursionLimit’,1500)
tic;
model = ’pitot2’;
date = ’09_28_07’;
run = ’run12’;
data_path = [’..\’,model,’\’,date,’\’,run,’\’];

% tabulate data of respective model
if strcmp(model,’pitot’)
    [v_pitot_dc,t] = tekread([data_path,’ch1.wfm’]);
    [v_pitot_ac,t] = tekread([data_path,’ch2.wfm’]);
    [v_ct,t] = tekread([data_path,’ch3.wfm’]);
    [v_ldi,t] = tekread([data_path,’ch4.wfm’]);
    [v_feedback_control,tlong] = tekread([data_path,’ch5.wfm’]);
    [v_cold_wire,tlong] = tekread([data_path,’ch5.wfm’]);
elseif strcmp(model,’pitot2’)
    [v_pitot_dc,t] = tekread([data_path,’ch1.wfm’]);
    [v_pitot_ac,t] = tekread([data_path,’ch2.wfm’]);
```

```
    [v_ct,t] = tekread([data_path,'ch3.wfm']);
    [v_ldi,t] = tekread([data_path,'ch3.wfm']);
    [v_feedback_control,tlong] = tekread([data_path,'ch3.wfm']);
    [v_cold_wire,tlong] = tekread([data_path,'ch3.wfm']);
elseif strcmp(model,'ffc2')
    [v_pitot_dc,t] = tekread([data_path,'ch1.wfm']);
    [v_pitot_ac,t] = tekread([data_path,'ch2.wfm']);
    [v_ct,t] = tekread([data_path,'ch3.wfm']);
    [v_ldi,t] = tekread([data_path,'ch3.wfm']);
    [v_feedback_control,tlong] = tekread([data_path,'ch3.wfm']);
    [v_cold_wire,tlong] = tekread([data_path,'ch3.wfm']);
else
    [v_pitot_dc,t] = tekread([data_path,'ch1.wfm']);
    [v_pitot_ac,t] = tekread([data_path,'ch2.wfm']);
    [v_ct,t] = tekread([data_path,'ch3.wfm']);
    [v_ldi,t] = tekread([data_path,'ch4.wfm']);
    [v_cold_wire,tlong] = tekread([data_path,'ch5.wfm']);
    [v_feedback_control,tlong] = tekread([data_path,'ch6.wfm']);
end
toc;

gamma = 1.4;
R = 287;
vol = pi*(.305/2)^2*20.7;
c1 = sqrt(gamma*(2/(gamma+1))^((gamma+1)/(gamma-1)));
A_star = 1.368*.0254^2;

% calibration of contraction pitot:
p_ct = 6.5777*v_ct - 8.1631;
```

```
% choose correct calibration curve
if strcmp(model,'hemisphere')
    % calibration of hemispherical model pitot:
    p_pitot_ac = v_pitot_ac*1.1801 / 100;
    p_pitot_dc = 1.1801*v_pitot_dc + .1976;
    fprintf(model)
    fprintf(date)
    fprintf(run)
elseif strcmp(model,'ffc')
    %calibration of forward facing cavity pitot:
    p_pitot_ac = v_pitot_ac*1.4856 / 100;
    p_pitot_dc = 1.4856*v_pitot_dc - .724;
    fprintf(model)
    fprintf(date)
    fprintf(run)
elseif strcmp(model,'pitot')
    %calibration of pitot probe:
    p_pitot_ac = v_pitot_ac*1.0585 / 100;
    p_pitot_dc = 1.0585*v_pitot_dc + .9393;
    fprintf(model)
    fprintf(date)
    fprintf(run)
elseif strcmp(model,'pitot2')
    %calibration of pitot probe 2:
    p_pitot_ac = v_pitot_ac*1.054 / 100;
    p_pitot_dc = 1.054*v_pitot_dc + 1.2441;
    p_ct = 4.9161*v_ct - .9208;
    fprintf(model)
```

```
    fprintf(date)
    fprintf(run)
elseif strcmp(model,'ffc2')
    %calibration of pitot probe 2:
    p_pitot_ac = v_pitot_ac*1.4597 / 100;
    p_pitot_dc = 1.4597*v_pitot_dc - .6848;
    p_ct = 4.9161*v_ct - .9208;
    fprintf(model)
    fprintf(date)
    fprintf(run)
end

% calibration of ldi
Eo = 6.76; % V
lambda = 632.8; % nm
phi = lambda/pi*v_ldi/Eo; % nm

% calibration of cold wire
T_re = ((90.162*(4.0516*v_cold_wire+10.213)-1113.5)-32)*5/9+273.15;
% Recovery Temperature (K)



length_of_record = 10; % s
sampling_freq = length(v_pitot_ac) / length_of_record; % Hz
points = 100;
perpoint = sampling_freq * length_of_record / points;

if strcmp(model,'hemisphere') | strcmp(model,'ffc')
    T_re = T_re(1:2:length(v_cold_wire));   % T_re and v_feedback_ontrol
```

```
%     were sampled at twice the frequency of the rest of the variables
    v_feedback_control = v_feedback_control(1:2:length(v_feedback_control));
    T_tot_i = mean(T_re(1:.05*length_of_record*perpoint));
elseif strcmp(model,'pitot')
    T_re = T_re(1:2:length(v_cold_wire));   % T_re and v_feedback_control
%     were sampled at twice the frequency of the rest of the variables
    v_feedback_control = v_feedback_control(1:2:length(v_feedback_control));
    T_tot_i = load([data_path,'T_ct_i.txt'])*5/9+273.15;
else
    T_tot_i = load([data_path,'T_ct_i.txt'])*5/9+273.15;
end

p_ct_i = mean(p_ct(1:.05*length_of_record*perpoint)) % Initial stagnation
% pressure
T_tot = T_tot_i*(p_ct/p_ct_i).^((gamma-1)/gamma);  % Theoretical Stagnation
% Temperature. note that the real stagnation temperature is the recovery
% temperature divided by the recovery factor eta. namely: T_stagn
rho_tot = (p_ct*6895)./(R*T_tot);
p_ct_theo = p_ct_i*(1+(gamma-1)/2*A_star/vol*sqrt(R*T_tot_i)*t*c1).^...
    (2*gamma/(1-gamma));

eta = [ones(.1*length(t),1)' .98:.03/(.419999*length(t)):1.01 ones...
    (.48*length(t),1)']';
eta_red = [ones(.1*points,1)' .98:.03/(.41*points):1.01 ones...
    (.48*points,1)']';


T_stagn = T_re./eta;
rho_stagn = (p_ct*6895)./(R*T_stagn);
```

```
p_pitot_ac_red = zeros(points,perpoint);
v_pitot_ac_red = zeros(points,perpoint);
t_red = zeros(points,1);
p_rms_red = zeros(points,1);
v_rms_red = zeros(points,1);
p_mean_red = zeros(points,1);
noise_red = zeros(points,1);
p_ct_red = zeros(points,1);
phi_red = zeros(points,1);
T_tot_red = zeros(points,1);
rho_tot_red = zeros(points,1);
T_re_red = zeros(points,1);
v_feedback_control_red = zeros(points,1);
T_stagn_red = zeros(points,1);
rho_stagn_red = zeros(points,1);
M = zeros(points,1);
p_stat = zeros(points,1);
T_stat_theo = zeros(points,1);
rho_stat_theo = zeros(points,1);
a_theo = zeros(points,1);
U_theo = zeros(points,1);
Re_ft_theo = zeros(points,1);
Kn_theo = zeros(points,1);
T_stat = zeros(points,1);
rho_stat = zeros(points,1);
a = zeros(points,1);
U = zeros(points,1);
```

```
Re_ft = zeros(points,1);
Kn = zeros(points,1);




for n = 1:1:points
    p_pitot_ac_red(n,:) = p_pitot_ac(((n-1)*perpoint + 1):n*perpoint)';
    v_pitot_ac_red(n,:) = v_pitot_ac(((n-1)*perpoint + 1):n*perpoint)';
    if max(p_pitot_ac_red(n,1:100)) - p_pitot_ac(1) > 0.1 * (max...
            (p_pitot_ac) - min(p_pitot_ac))
        p_pitot_ac_red(n,:) = p_pitot_dc(((n-1)*perpoint + 1):...
            n*perpoint)';
    end
    t_red(n) = t(perpoint*n);
    p_rms_red(n) = sqrt(mean((p_pitot_ac_red(n,:) - mean...
        (p_pitot_ac_red(n,:))).^2));
    v_rms_red(n) = sqrt(mean((v_pitot_ac_red(n,:) - mean...
        (v_pitot_ac_red(n,:))).^2));
    p_mean_red(n) = mean(p_pitot_dc(((n-1)*perpoint + 1):...
        n*perpoint));
    noise_red(n) = p_rms_red(n) / p_mean_red(n) * 100;
    p_ct_red(n) = mean(p_ct(((n-1)*perpoint + 1):n*perpoint));
    phi_red(n) = mean(phi(((n-1)*perpoint + 1):n*perpoint));
    T_tot_red(n) = mean(T_tot(((n-1)*perpoint + 1):n*perpoint));
    rho_tot_red(n) = mean(rho_tot(((n-1)*perpoint + 1):n*perpoint));
    T_re_red(n) = mean(T_re(((n-1)*perpoint + 1):n*perpoint));
    v_feedback_control_red(n) = mean(v_feedback_control(((n-1)*...
        perpoint + 1):n*perpoint));
```

```
    T_stagn_red(n) = mean(T_stagn(((n-1)*perpoint + 1):n*perpoint));
    rho_stagn_red(n) = mean(rho_stagn(((n-1)*perpoint + 1):...
        n*perpoint));
    if strcmp(model,'hemisphere') | strcmp(model,'pitot') | strcmp...
            (model,'pitot2')
        M(n) = Rayleigh_pitot(p_ct_red(n), p_mean_red(n), 0, 20);
        p_stat(n) = p_ct_red(n)/(1+(gamma-1)/2*M(n)^2)^(gamma/...
            (gamma-1));
        T_stat_theo(n) = T_tot_red(n)/(1+(gamma-1)/2*M(n)^2);
        rho_stat_theo(n) = rho_tot_red(n)/(1+(gamma-1)/2*M(n)^2)^...
            (1/(gamma-1));
        a_theo(n) = sqrt(gamma*R*T_stat_theo(n));
        U_theo(n) = M(n)*a_theo(n);
        Re_ft_theo(n) = reynolds(T_stat_theo(n),rho_stat_theo(n),...
            U_theo(n));
        Kn_theo(n) = knudsen(M(n),Re_ft_theo(n));
        T_stat(n) = T_stagn_red(n)/(1+(gamma-1)/2*M(n)^2);
        rho_stat(n) = rho_stagn_red(n)/(1+(gamma-1)/2*M(n)^2)^(1/...
            (gamma-1));
        a(n) = sqrt(gamma*R*T_stat(n));
        U(n) = M(n)*a(n);
        Re_ft(n) = reynolds(T_stat(n), rho_stat(n), U(n));
        Kn(n) = knudsen(M(n),Re_ft(n));
    end
end
toc;
```

D.3 Mach Number Calculation

The code used to calculate the Mach number is listed below. This function solves the Rayleigh pitot function recursively. It employs the bisector method. It is a helper function for the above noise level calculation.

```
function [M] = Rayleigh_pitot(p01, p02, Mlow, Mhigh);

gamma=1.4;

M = (Mhigh + Mlow)/2;

p02overp1 = ( (gamma+1)^2*M^2 / (4*gamma*M^2-2*(gamma-1)) )^...
    (gamma/(gamma-1)) * (1-gamma+2*gamma*M^2) / (gamma+1);

p01overp1 = (1+(gamma-1)/2*M^2)^(gamma/(gamma-1));

p02overp01 = p02overp1/p01overp1;

if abs(p02overp01 / (p02/p01)) < 0.9999
    [M] = Rayleigh_pitot(p01, p02, Mlow, M);
elseif abs(p02overp01 / (p02/p01)) > 1.0001
    [M] = Rayleigh_pitot(p01, p02, M, Mhigh);
end
```

D.4 Reynolds Number Calculation

The code used to calculate the Reynolds number is listed below. It is a helper function for the above noise level calculation.

```
function Re_ft=reynolds(T,rho,V)
```

```
S = 110.4; %Sutherland Temperature in K

mu_ref = 1.716e-5; %kg/(m*s)

T_ref = 273.15; %K

mu = mu_ref*(T/T_ref)^(3/2)*((T_ref+S)/(T+S));

Re_m = rho*V/mu; % per meter

Re_ft = Re_m/3.281; % per foot
```

D.5 Knudsen Number Calculation

The code used to calculate the Knudsen number is listed below. It is a helper function for the above noise level calculation.

```
function Kn = knudsen(M, Re)

% Re per foot

gamma = 1.4;

d = .00015/12; % Wire diameter in in

Re = Re*d;

Kn = sqrt(pi*gamma/2)*M/Re;
```

D.6 Forward-Facing Cavity Power Spectrum Calculation

The code used to analyze the forward-facing cavity fluctuation data is listed below.

```
clear; clc; close all; clear variables
tic;
model = 'ffc2';
date = '10_02_07';
run = 'run5';
data_path = ['..\',model,'\',date,'\',run,'\'];

[v_pitot_dc,t] = tekread([data_path,'ch1.wfm']);
[v_pitot_ac,t] = tekread([data_path,'ch2.wfm']);
[ldi,t] = tekread([data_path,'ch3.wfm']);
toc;

if strcmp(model,'hemisphere')
    % calibration of hemispherical model pitot:
    p_pitot_ac = v_pitot_ac*1.1801 / 100;
    p_pitot_dc = 1.1801*v_pitot_dc + .1976;
    fprintf(model)
    fprintf(date)
    fprintf(run)
elseif strcmp(model,'ffc')
    %calibration of forward facing cavity pitot:
    p_pitot_ac = v_pitot_ac*1.4856 / 100;
    p_pitot_dc = 1.4856*v_pitot_dc - .724;
    fprintf(model)
    fprintf(date)
```

```
    fprintf(run)
elseif strcmp(model,'pitot')
    %calibration of pitot probe:
    p_pitot_ac = v_pitot_ac*1.0585 / 100;
    p_pitot_dc = 1.0585*v_pitot_dc + .9393;
    fprintf(model)
    fprintf(date)
    fprintf(run)
    elseif strcmp(model,'pitot2')
    %calibration of pitot probe 2:
    p_pitot_ac = v_pitot_ac*1.054 / 100;
    p_pitot_dc = 1.054*v_pitot_dc + 1.2441;
    fprintf(model)
    fprintf(date)
    fprintf(run)
elseif strcmp(model,'ffc2')
    %calibration of pitot probe 2:
    p_pitot_ac = v_pitot_ac*1.4597 / 100;
    p_pitot_dc = 1.4597*v_pitot_dc - .6848;
    fprintf(model)
    fprintf(date)
    fprintf(run)
end

p_i = mean(p_pitot_dc(1:.05*length(p_pitot_dc)/200))

% calibration of ldi
Eo = 6.76; % V
lambda = 632.8; % nm
```

```
ldi = lambda/pi*ldi/Eo; % nm

p_pitot_dc = p_pitot_dc(.16*length(p_pitot_dc):.41*length(p_pitot_dc)-1);
p_pitot_ac = p_pitot_ac(.16*length(p_pitot_ac):.41*length(p_pitot_ac)-1);
ldi = ldi(.16*length(ldi):.41*length(ldi)-1);
t = t(.16*length(t):.41*length(t)-1);

length_of_record = 2.5; % s
sampling_freq = length(p_pitot_ac) / length_of_record; % Hz
n = 2^18;
N = 2^16;
f = sampling_freq*(0:N)/n;
windowsize = 150;

pitot_fft = fft(p_pitot_ac,n);
ldi_fft = fft(ldi,n);

pitot_power = pitot_fft.*conj(pitot_fft)/n;
ldi_power = ldi_fft.*conj(ldi_fft)/n;
pitot_power = filter(ones(1,windowsize)/windowsize,1,pitot_power);
ldi_power = filter(ones(1,windowsize)/windowsize,1,ldi_power);
```

D.7 LDI Noise Analysis

The code used to analyze the LDI noise is listed below.

```
clear; clc; close all; clear variables
tic;
model = 'M6_ldi_noise';
date = '09_19_07';
```

```
run = 'run6';
data_path = ['..\',model,'\',date,'\',run,'\'];

[ldi,t] = tekread([data_path,'ch2.wfm']);
toc;

% calibration of ldi
Eo = 6.76; % V
lambda = 632.8; % nm
ldi = lambda/pi*ldi/Eo; % nm

length_of_record = 1e-3; % s
sampling_freq = length(ldi) / length_of_record; % Hz

n = 2^8;
N = 2^7;
f = sampling_freq*(0:N)/n;
windowsize = 10;

ldi_red = filter(ones(1,windowsize)/windowsize,1,ldi);
noise = ldi-ldi_red;
ldi_fft = fft(ldi,n);
ldi_power = ldi_fft.*conj(ldi_fft)/n;
```

E. Figure Source Data

Table E.1 identifies which tunnel runs were used to create the figures presented herein.

Table E.1: Figure source data

Figure	Model	Year	Month	Day	Run No.
2.8	pitot	2007	Apr	2	1, 4, 7
2.9	pitot	2007	Apr	2	all runs
2.10	hemisphere	2007	Mar	7	all runs
2.12	hemisphere	2007	Mar	7	8
2.13	hemisphere	2007	Mar	7	8
2.14	hemisphere	2007	Mar	7	8
2.15	hemisphere	2007	Mar	7	8
2.16	hemisphere	2007	Mar	7	8
2.17	hemisphere	2007	Mar	7	8
2.18	hemisphere	2007	Mar	7	8
2.19	pitot	2007	Sep	28	1, 7, 12
2.20	pitot	2007	Sep	28	all runs
2.21	pitot	2007	Sep	28	all runs
4.1	hemisphere	2007	Mar	7	1, 8
4.2	hemisphere	2007	Mar	7	1, 8
4.13	FFC	2007	Mar	29	4, 5
4.14	FFC	2007	Mar	28, 29	10, 2
4.15	FFC	2007	Mar	28	2, 5
4.16	FFC	2007	Apr	1	1, 3

Continued on next page

Figure	Model	Year	Month	Day	Run No.
4.17	FFC	2007	Mar	30	2, 5
4.18	FFC	2007	Mar	31	1, 3
4.22	FFC	2007	Oct	3	12, 15
4.23	FFC	2007	Oct	1	16, 19
4.24	FFC	2007	Oct	3	8, 11
4.25	FFC	2007	Oct	2	6, 8
4.26a	FFC	2007	Oct	2	11
4.26b	FFC	2007	Oct	2	15
4.26c	FFC	2007	Oct	2	3
4.26d	FFC	2007	Oct	3	6
4.26e	FFC	2007	Oct	3	3